

Tagging ultra-boosted jets at FCC-hh using machine learning techniques

Sanchari Bhattacharyya,^a Biplob Bhattacharjee,^a Camellia Bose,^a Debtosh Chowdhury,^b Swagata Mukherjee^b

^a*Centre for High Energy Physics, Indian Institute of Science, Bangalore 560012, India*

^b*Department of Physics, Indian Institute of Technology, Kanpur 208016, India*

E-mail: biplob@iisc.ac.in, sancharibhat@iisc.ac.in,
camelliabose@iisc.ac.in, debtoshc@iitk.ac.in, swagata@iitk.ac.in

ABSTRACT: The Future Circular Hadron Collider (FCC-hh) will probe unprecedented energy regimes, enabling direct searches for new elementary particles at a scale of tens of TeV. FCC-hh is currently in the planning stage, and one of its primary physics goals is to search for physics beyond the Standard Model by exploring a previously inaccessible kinematic domain. While venturing into uncharted high-energy territories promises excitement, reconstructing objects with enormous transverse momenta will require overcoming major experimental challenges. This work investigates the identification of boosted W bosons and boosted top quarks in the context of three beyond the Standard Model scenarios: heavy vector-like quark (B'), heavy neutral gauge boson (Z'), and heavy neutral Higgs boson (H). We employ machine learning techniques, including eXtreme Gradient Boosting (XGBoost) and convolutional neural networks (CNN), to identify these ultra-boosted objects in the collider from their SM background counterpart. We evaluate the performance of these techniques in distinguishing W jets and top jets from QCD jets at extremely high transverse momenta (p_T) values, demonstrating their potential for future FCC-hh analyses.

Contents

1	Introduction	1
2	Theoretical Scenarios	4
3	CERN FCC facility	9
4	Simulation of events	11
5	Challenges and mitigation strategies for jets at $\sqrt{s} = 100$ TeV	13
5.1	Effect of fixed jet radius on top and QCD jet mass	14
5.1.1	Jet radius estimation at the parton level	15
5.2	Effects of finite detector resolution on top and QCD jet mass	17
5.2.1	Calorimeters	18
5.2.2	Tracking system	19
5.3	Effects of finite detector resolution on N-Subjettiness observables	20
5.4	Boosted W jets at $\sqrt{s} = 100$ TeV	22
5.5	Jet grooming techniques	25
6	Machine learning techniques for jet tagging	26
6.1	Extreme Gradient Boosted Decision Trees	27
6.2	Convolutional Neural Networks (CNN)	30
6.2.1	Pre-processing of the images	30
6.2.2	The network architecture and results	30
7	Analysis of BSM processes with top and W jets in the final state	34
7.1	Analysis of Z' boson decaying to boosted top jets	36
7.1.1	Effect of b tagging	38
7.2	Analysis of neutral heavy Higgs boson decaying to boosted W jets	40
7.3	Analysis of vector-like, heavy B' quark decaying to boosted top jet and W jet	42

8 Conclusion	44
9 Acknowledgments	46
Appendix A Jet energy response and resolution	47
Appendix B Efficiencies used by DELPHES	49
Appendix C Jet after soft drop	50

1 Introduction

Experiments at the Large Hadron Collider (LHC) have contributed significantly to our understanding of the Standard Model (SM) of particle physics, including the discovery of the Higgs boson and precision measurements of its properties [1–7]. While the SM has been rigorously tested with great precision, unanswered puzzles remain, such as the hierarchy problem, the observed phenomena of dark matter, neutrino masses, and matter-antimatter asymmetry in the universe. Although these gaps in our understanding of the universe suggest the existence of Beyond the Standard Model (BSM) physics, there is no consensus about the typical scale at which the new physics should appear.

The lack of conclusive evidence for new physics at the LHC suggests that BSM phenomena may occur at energy scales inaccessible to current collider experiments. Various BSM scenarios predict new particles with large masses. For example, a simple $U(1)$ extension of the SM in the gauge sector predicts the existence of a new gauge boson Z' [8–10]. Similarly, BSM extensions of the Higgs sector in theories such as the Two Higgs Doublet Model [11–18] contain charged and neutral heavy Higgs bosons. Future collider initiatives are essential for exploring such BSM phenomena at energy scales beyond the LHC’s capabilities. The production of such heavy BSM particles at future colliders results in highly energetic and heavily boosted decay products, complicating event reconstruction and object identification. This study focuses on efficiently identifying these heavy states, common to many prominent BSM physics models, in a typical general-purpose experiment of the FCC-hh collider.

The FCC-hh [19, 20] program at CERN, Geneva, boasts an exceptionally broad physics program, spanning Standard Model precision studies to direct searches for BSM. It will explore

uncharted territories in high-energy physics, enabling searches for new physics at unprecedented mass scales. However, this endeavor also poses unique challenges in object reconstruction, particularly for objects with extremely large transverse momenta (p_T) [21–23]. In the case of FCC-hh, the large p_T of objects resulting from the decay of a highly massive particle leads to highly collimated decay products. Accurate reconstruction of these events depends on high-resolution detectors to resolve the individual signatures within these ultra-boosted objects [24].

In BSM physics analyses featuring final states that contain the W boson or the top quark, high selection efficiencies can generally be attained by leveraging hadronic decay channels. At sufficiently large Lorentz boost (typically $p_T > 200$ GeV or so), the final-state hadrons from the decay of W bosons or top quarks merge into a single large-radius (i.e., fat) jet. In such cases, jet substructure techniques are normally used to identify the jets arising from decays of W bosons or top quarks, exploiting the multiple, experimentally separable subjets within the fat jet [25–30]. However, in FCC-hh, where p_T of top quark or W boson can be in the multi-TeV range, the subjets will overlap and may not be experimentally separable anymore. Then, a key question that arises is how robust or useful the jet substructure observables (like N-Subjettiness [25]) will remain at such high energy scales. The highly collimated nature of jets at FCC-hh will make it very challenging to identify their subjet information in the same way as it is still possible at the LHC. The proposed solution in this direction has been to use observables constructed on track jets, as the tracking devices have the best resolution, much better than the calorimeters. Track-based observables offer improved discrimination properties of jet substructure variables compared to calorimeter-based methods, owing to the better resolution of the tracking system at FCC-hh [21, 22]. In this context, we present studies on the robustness of the improved discriminating power under various conditions of energy resolution of calorimeters, as well as the granularity of calorimeters and trackers. Moreover, previous studies have highlighted the importance of choosing an optimum jet radius to avoid contamination from excess radiation [21]. In this work, we focus on optimizing the jet radius from parton-level information of the top quark and W boson decay.

Furthermore, the performance of jet tagging at the LHC has steadily been improving and heavily relies on various Machine Learning (ML) techniques [31–83], which also inspires jet tagging algorithms for the proposed FCC-hh detectors. The focus of this work is mainly to provide a basic understanding of boosted top and W jet identification in FCC-hh detectors using Extreme Gradient Boosting (XGBoost) [84] and Convolutional Neural Networks (CNN) [85–87]. These two relatively simple ML models, based on high-level jet features and low-level jet constituents, respectively, are used to establish a baseline for preliminary feasibility studies at 100 TeV. The goal is to understand how well these taggers perform in the FCC-hh environment compared to their performance in the LHC environment, which can then serve

as a reference point for further improvements involving more complex and state-of-the-art ML taggers. We thus investigate the feasibility of efficiently distinguishing multi-prong W jets and top quark jets from single-prong QCD jets, where these objects have extremely high p_T , far exceeding those encountered at the LHC. Previous work in Ref. [88] employed boosted decision trees (BDTs) in the context of 100 TeV pp collisions, focusing on jets with $p_T \sim 5$ TeV. Our study focuses on multiple jet p_T bins ranging from 2 TeV to 16 TeV. The models in our work are trained as multi-class classifiers. We use the score from the classifiers to tag the final state top and W jets, thus allowing us to reconstruct the massive BSM particle. The study is based on the fast simulation of the reference FCC-hh detector [19, 20, 89].

Earlier works have studied the discovery potential of the FCC-hh for heavy resonances using BDTs [90, 91]. In our study, we explore the variation of jet kinematics with p_T and make use of the information to build jet identification strategies spanning a broad range of transverse momenta. The reason is that any heavy resonance decays to jets with p_T ranging from, say, $\mathcal{O}(1)$ TeV to as high as half of its mass. The capability of FCC-hh to directly produce such heavy resonances necessitates the development of p_T -specific taggers, as demonstrated in our study. We perform a detailed analysis of three benchmark BSM scenarios: a high-mass Z' boson decaying to boosted top jets, a heavy neutral CP-even Higgs boson decaying to boosted W jets, and a high-mass vector-like quark (B') decaying to a boosted top quark jet and a boosted W jet.

This paper explores the feasibility of efficiently distinguishing between boosted top jets, W jets, and QCD jets at extremely high transverse momenta (multi-TeV range). We focus on developing and validating simple machine learning-based top and W taggers rather than optimizing the analysis flow for setting cross-section limits on BSM scenarios. The example analyses presented in this paper are illustrative, and the analysis strategy can be refined further to improve the cross-section limits presented here. Our goal is to lay the groundwork for future studies rather than striving for the most stringent limits.

Another caveat is that we have not included pileup in our study. The FCC-hh is expected to have a mean pileup of 500-1000 at an instantaneous luminosity of $30 \times 10^{34} \text{ cm}^{-2}\text{s}^{-1}$ [20]. However, pileup mitigation strategies (pile-up subtraction algorithms like PUPPI [92]) for FCC-hh are still under development and not yet standardised. Moreover, the final states analysed in this study involve highly energetic jets in the multi-TeV range. In this regime, the relative effect of pileup is expected to be significantly reduced. Therefore, while the omission of pileup represents a limitation, its impact can be neglected to first approximation for the purposes of this exploratory study.

The outline of this paper is as follows: In Section 2, the physics models we consider are described. A brief description of the proposed FCC facility is provided in Section 3. Details

of event simulation are discussed in Section 4. The challenges that occur while reconstructing boosted jets at the $\sqrt{s} = 100$ TeV collider are highlighted in Section 5. It presents a detailed discussion about jet radius, jet substructure observables, and boosted W boson jets that may appear in the final states of various BSM scenarios. The section also addresses the effect of finite calorimeter and tracker resolution on the jet observables, along with the impact of jet grooming. Details of the ML models used in this study are provided in Section 6. Finally, the analyses of the three benchmark BSM scenarios are presented: a heavy neutral Z' boson in Section 7.1, a heavy neutral CP-even Higgs boson in Section 7.2, and a high-mass vector-like bottom-partner (B') in Section 7.3. The conclusions and outlook are summarised in Section 8.

2 Theoretical Scenarios

At the LHC, the top quarks and W bosons are produced via various SM interactions, like the strong and electroweak interactions. They can also originate from BSM interactions, such as the decay of heavy new particles predicted by BSM. There are several BSM scenarios where heavy resonances are produced, which then decay to top quarks or W bosons. The top quark eventually decays to a W boson and a b quark. Depending on the decay channel of the W boson, i.e., whether W decays to a lepton and a neutrino (leptonic decay) or to a quark-antiquark pair (hadronic decay), the final states will be different, leading to different signatures at the collider. In this analysis, we take into account three such BSM scenarios, which act as an additional source of top quarks and W bosons in addition to the SM.

To begin with, we consider a BSM scenario that involves a heavy neutral gauge boson, Z' , in addition to the SM spectrum. Such a heavy gauge boson is generic to many BSM scenarios, e.g., in the U(1) extended models [9, 10], Left-Right symmetric models (LRSM) [93–95], 3-3-1 model [96], Vector-leptoquark model [97], top-phillic Z' model [98, 99], etc. Z' may have a kinetic mixing with the SM Z boson, and depending on the symmetries of the corresponding models, it can decay into SM fermions. If the mass of Z' is quite high, the decay products are very boosted [100–103]. If kinematically allowed, a Z' can decay into a pair of top quarks. The results of an ATLAS study, where they have searched for a Z' boson decaying into a pair of hadronically decaying top quarks at the 13 TeV run of LHC with 139 fb^{-1} integrated luminosity [65], have excluded masses of Z' in the topcolor-assisted-technicolor model up to 3.9 TeV and 4.7 TeV, for the decay widths of 1% and 3%, respectively. In the context of FCC-hh, where the center of mass energy is 100 TeV, the FCC-hh can directly produce such a gauge boson with a very high mass (around tens of TeV). In this analysis, we have generated a multi-TeV scale Z' boson, and depending on its mass, we consider four benchmark points where $m_{Z'} = 5, 10, 15,$ and 20 TeV with a width to mass ratio ($\Gamma/m_{Z'}$) of 10%. We generate 10,000 events via the process $pp \rightarrow Z' \rightarrow t\bar{t}$ at 100 TeV run of FCC-hh using PYTHIA 8 (refer

to the Feynman diagram in Figure 1a. The top quarks decaying from such a heavy Z' will be highly boosted. Figure 1b represents the transverse momenta of such boosted top quarks for four different masses of the Z' . Similar final states ($t\bar{t}$) also arise in the SM due to QCD interactions, e.g., $pp \rightarrow t\bar{t}$ production, which is an important background for $Z' \rightarrow t\bar{t}$ search. The SM dijet production ($pp \rightarrow jj$) also acts as a major background process in the search for Z' . In section 7.1, we will discuss the signal-background analysis for Z' in detail.

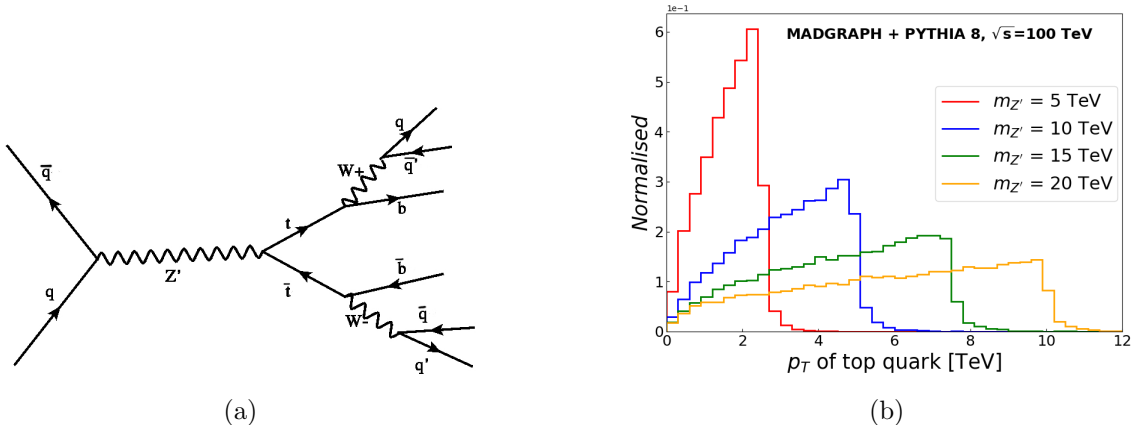


Figure 1: (a) Feynman diagram of s -channel production of a Z' , with the $Z' \rightarrow t\bar{t}$ decay where t and \bar{t} decay hadronically. (b) Transverse momentum distribution of a top quark coming from the decay of a Z' boson produced at the FCC-hh.

Next, we consider another BSM scenario that involves a heavy CP-even Higgs boson. Theories involving one or more heavy neutral and charged scalars have been extensively studied in the literature. One popular example is the Two Higgs Doublet Model (THDM) [12–18]. In addition to that, many of the well-studied BSM theories like Minimal Supersymmetric Standard Models (MSSM) [104–110], Left-Right Symmetric Models (LRSM) [93–95, 111], Extra-Dimensional models [112, 113], Grand Unified Theories (GUTs) [114, 115], multi-Higgs Doublet models [116–121], Georgi-Machacek model (GM) [122–128] have at least one heavy CP-even scalar other than the SM-like light Higgs boson in its mass spectrum. Both ATLAS and CMS collaborations have searched for such heavy scalars, neutral as well as charged [129–138].

The ATLAS collaboration performed a search for a heavy neutral resonance in the $W^+W^- \rightarrow \mu^+\bar{\nu}\mu^-\bar{\nu}$ channel using 13 TeV data corresponding to an integrated luminosity of 139 fb^{-1} . For a narrow-width Higgs-like scalar, 95% CL upper limits are set on the production cross-section times branching ratio. At $m_H = 3.8 \text{ TeV}$, values above 0.0048 pb and 0.0045 pb are excluded in the ggF and VBF production modes, respectively [139]. The

FCC-hh shall be able to directly produce a much heavier Higgs boson. Just as in the case of Z' , here too we choose four benchmark points by varying the mass of H , i.e., $m_H = 5, 10, 15, 20$ TeV, with the decay mode $H \rightarrow W^+W^-$. In our study, we consider the fully hadronic decay of the boosted W 's as we aim to study the boosted W jet tagging scenario at FCC-hh.

We generate 10,000 $pp \rightarrow H \rightarrow WW$ events using PYTHIA 8 with $\Gamma/m_H = 10\%$, where the W bosons decay hadronically to jets (refer to the Feynman diagram in Figure 2a). The decay of such massive Higgs bosons results in ultra-boosted W bosons. Figure 2b depicts the transverse momentum (p_T) of the boosted W 's considering four different heavy Higgs boson masses. As observed from the figure, W bosons from the decay of the massive Higgses are extremely boosted (very large p_T). In this case, the major SM background processes include W^+W^- pair production, $t\bar{t}$ production, and dijet production, the analysis of which is presented in detail in Section 7.2.

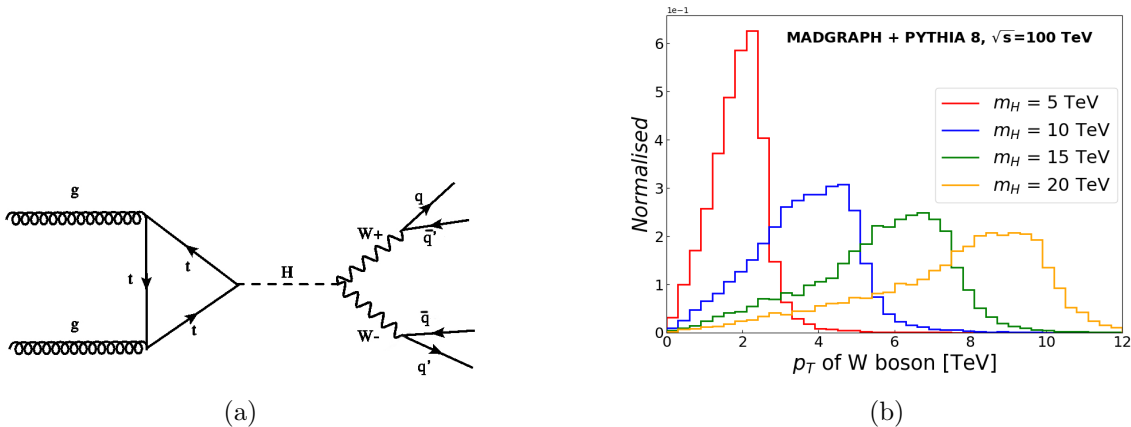


Figure 2: (a) Feynman diagram of gluon-gluon fusion production of H decaying via $H \rightarrow W^+W^-$ where the W 's decay hadronically. (b) Transverse momentum distribution of W boson produced from the decay of the heavy Higgs at the FCC-hh.

In our study, the W bosons are treated as unpolarised. While the results may be sensitive to the polarisation of the W bosons, as discussed in Ref. [140], a detailed analysis of polarisation effects is beyond the scope of this work.

The last model that we consider in our current analysis is a BSM scenario involving a vector-like quark (VLQ). A vector-like fermion is a Dirac fermion whose left- and right-chiral components have similar transformations under the SM gauge group. Thus, their representations are free from chiral anomaly. The minimal model for a VLQ analysis could be a VLQ singlet or doublet added to the SM Lagrangian. Theories with one or more VLQs have been considered in the literature where different multiplets of VLQs have been added

to the SM Lagrangian and their exotic decay modes, and related phenomenology has been studied [141–153].

A generic VLQ model may be categorised into models having bottom-like (B') or top-like (T') partners, or models where the VLQ has fractional charges other than $-1/3$ or $2/3$ [149, 150, 152]. ATLAS and CMS collaborations have extensively searched for B' and T' quarks in the 13 TeV run of LHC [154–162] via its various decay modes. In many BSM theories, B' or T' quarks mainly interact with third-generation SM quarks. Depending on the charge of the VLQ, it can decay to a top (or bottom) quark and a W boson (or SM/BSM particle, for example, SM Higgs/Heavy Higgs/ Z boson, etc.) [163–165]. If the VLQ is very heavy, then the top quark, coming from its decay, will be highly boosted. In such cases, the decay products of the top quark become highly collimated, and separating them from the usual background of jets becomes challenging. The search for VLQs with boosted top signatures has been performed in multiple studies [166–171]. The ATLAS collaboration has searched for a vector-like T' quark at 13 TeV LHC run, where T' decays to a top quark and a Z boson, followed by $t \rightarrow bW$, $W \rightarrow jets$ and $Z \rightarrow \nu\bar{\nu}$ [171]. They have carried out the analysis with boosted top topology and have quoted the lower mass limit of the VLQ to be 1.8 TeV. The CMS collaboration has also searched for vector-like B' quark decaying to a W boson and a top quark at 13 TeV run with 138 fb^{-1} integrated luminosity [166]. This analysis excludes the mass of the B' quark up to 1.56 TeV.

At FCC-hh, VLQs can be produced with masses of tens of TeV. We consider a BSM scenario where we have added one $SU(2)$ singlet bottom-like VLQ, B' having $SU(3)_C \otimes SU(2)_L \otimes U(1)_Y$ gauge quantum numbers as $(3, 1, -1/3)$, to the SM Lagrangian which interacts with the first and third generation SM quarks [163–165]. The interactions relevant for our study reads as [165],

$$\mathcal{L} \supset \frac{g\tilde{g}}{2} \left[\sqrt{\frac{R_L}{1+R_L}} \bar{B}'_L W_\mu^- \gamma^\mu u_L + \sqrt{\frac{1}{1+R_L}} \bar{B}'_L W_\mu^- \gamma^\mu t_L \right] + \text{h.c.} \quad (2.1)$$

where, g stands for $SU(2)_L$ gauge coupling constant of SM, and \tilde{g} and R_L are real-valued parameters. This B' can be singly-produced or pair-produced at the LHC or FCC-hh via electroweak or strong processes. In the present analysis, we produce a single B' in association with a light jet via the process $pp \rightarrow jB' \rightarrow jtW$. This production mode is chosen due to its relatively enhanced cross-section compared to pair production, especially at higher B' masses. We use the model file described in Ref. [163] and set the coupling parameter values fixed at $\tilde{g} = 0.1$ and $R_L = 0.5$.

We generate 50,000 events featuring B' , with two benchmark masses of 5 TeV and 10 TeV, produced in association with a light jet, were generated using the event generator MADGRAPH v2.9.18 [172] and the UFO file from Ref. [173]. The production cross-sections of $pp \rightarrow$

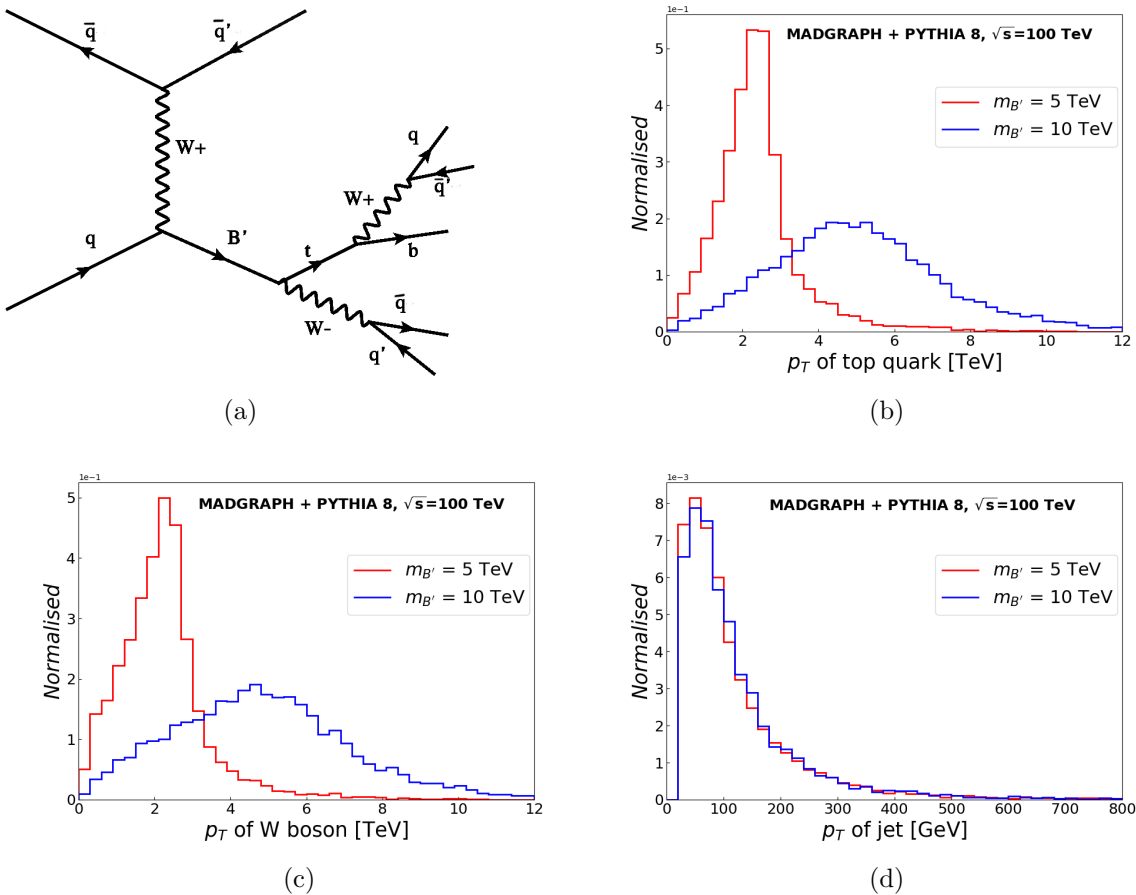


Figure 3: (a) Feynman diagram of t -channel production of B' with an associated jet and W exchange, where B' decays as $B' \rightarrow tW$ followed by hadronic decay of W . Distribution of transverse momentum of (b) the top quark coming from the decay of B' , (c) the W boson coming from the decay of B' , and (d) the light jet produced in association with the B' , for two different mass values of the singlet B' produced at the FCC-hh. These plots are made at the parton level.

$jB' \rightarrow jtW$ for $m_{B'} = 5$ TeV and $m_{B'} = 10$ TeV are 287 fb and 33 fb, respectively. After being produced, the B' decays to tW with a maximum branching ratio (BR) compared to its other decay modes [163, 164]. The top quark then further decays to Wb with a nearly 100% branching ratio (refer to the Feynman diagram in Figure 3a).

In Figures 3b, 3c, and 3d, we present the transverse momenta (p_T) of the boosted top quark and the boosted W boson produced in the B' decay for two different masses of B' at the FCC-hh using PYTHIA 8. We observe that the p_T of the light jet produced in association

with B' is very small compared to the p_T of the top quark or the W boson. The top quark and the W boson have almost similar p_T distributions. Therein arises an issue where a W jet can be mistagged as a top jet or a QCD jet. Similar SM processes, as discussed earlier, will act as major backgrounds for this signal. The signal-background analysis considering this benchmark model will be described in section 7.3.

In the following sections, we first discuss the FCC detector and the event simulation elaborately, followed by the challenges and possible solutions while dealing with boosted top quarks and boosted W bosons. Then, we present our results in detail, considering the above-mentioned theoretical scenarios.

3 CERN FCC facility

The Future Circular Collider (FCC) [19] is a proposed particle accelerator designed to push the boundaries of the energy frontier and significantly surpass the center-of-mass energies of previous colliders like the LHC. The FCC project includes three main planned scenarios: FCC-ee for electron-positron collisions, FCC-eh for electron-hadron collisions, and FCC-hh for hadron-hadron collisions. The FCC-hh aims for a center-of-mass collision energy of 100 TeV, which is nearly seven times higher than the LHC. It will offer a very exciting opportunity to explore physics at the multi-TeV scale. The collider will be housed in a 100 km tunnel, making it the largest particle accelerator ever built. The main motivation for FCC-hh is the exploration of the energy frontier as best as possible. With an unprecedented center-of-mass energy of 100 TeV, it will significantly extend the mass reach for discovering new BSM particles. The collider will enable precision measurements of the Higgs boson, top quark, and electroweak symmetry-breaking properties, surpassing the capabilities of the LHC. The high energy and luminosity of FCC-hh will allow for detailed studies of rare processes and interactions, providing insights into the fundamental forces of nature.

One of the key technological challenges is the development of high-field superconducting magnets, which are essential for bending the proton beams along the collider's circular path. The FCC-hh will also require advancements in cryogenics and vacuum systems to maintain the necessary conditions for particle collisions. The magnetic dipole system shall offer a field of up to 16 Tesla using Nb_3Sn superconducting magnets. The FCC-hh is planned to have two high luminosity and two low luminosity interaction points. The detectors for the FCC-hh are designed to handle extreme conditions and highly energetic particles originating from 100 TeV proton-proton collisions.

The FCC-hh detector is designed to have a diameter of 20 m and length of 50 m [20]. The innermost layer of the detector consists of the tracking system, which tracks the trajec-

tories of charged particles in the presence of a strong magnetic field. Surrounding this is the calorimeter, which is divided into electromagnetic and hadronic components to measure the energy of electrons, photons, and hadrons. The outermost layer contains the muon detector, designed to identify and measure the momentum of muons, which penetrate through the calorimeter. The detector design has been simulated using the FCC-hh configuration card in DELPHES [89, 174].

The detectors of FCC-hh will feature highly granular tracking and calorimetry systems. The innermost tracking layer is designed to have three layers consisting of $25\text{--}33.3\mu\text{m} \times 50\text{--}400\mu\text{m}$ pixels within $r < 200$ mm, $33.3\mu\text{m} \times 400\mu\text{m}$ macro-pixels in the $200 < r < 900$ mm region, and $33.3\mu\text{m} \times 2 - 50$ mm macro-pixels in the $900 < r < 1600$ mm region [20]. The combined tracker resolution per detector layer is $7.5 - 9.5 \mu\text{m}$. The total number of readout channels combining the three layers is 16×10^9 , which is significantly larger than that of the Phase II ATLAS and CMS tracking systems (6×10^9 and 2.2×10^9 respectively) [20].

At large p_T , the momentum resolution ($\sigma(p_T)$) is largely dependent on the detector resolution, which can be estimated using the approximation:

$$\frac{\sigma(p_T)}{p_T} \simeq \frac{\sigma_\theta p_T}{BR^2} \quad (3.1)$$

where σ_θ is the tracker resolution per layer, B is the uniform magnetic field, and R is the tracker radius. In the most optimistic scenario, the momentum resolution $\sigma(p_T)/p_T$ with the proposed granularity is $\sim 20\%$ for $p_T = 10$ TeV, and $\sim 2\%$ for $p_T = 1$ TeV.

In the case of FCC-hh, the large p_T of objects resulting from the decay of a highly massive particle leads to highly collimated decay products. Accurate reconstruction of these events depends on high-resolution detectors to resolve the individual signatures within these ultra-boosted objects [24].

The proposal for the electromagnetic calorimeter (ECAL) and the hadron calorimeter (HCAL) of the FCC-hh collider assumes a $(\Delta\eta, \Delta\phi)$ segmentation of $(0.01, 0.012)$ and $(0.025, 0.025)$, respectively in the central region, i.e., $|\eta| < 2.5$. The energy deposits of the particles in a tower are termed *hits*. The energy deposits are smeared by a log-normal distribution with a standard deviation $\sigma(\eta, E)$, which is also the resolution, given by:

$$\left(\frac{\sigma}{E}\right)^2 = \left(\frac{S(\eta)}{\sqrt{E}}\right)^2 + C(\eta)^2 \quad (3.2)$$

where E is the energy of the particle, η is the pseudorapidity, S and C are the *stochastic* term and the *constant* term respectively. We have neglected the *noise* term: $(N(\eta)/E)^2$, as it does not contribute much at high energies. In fact, for highly energetic particles, $C(\eta)$

contributes dominantly to the energy resolution of the calorimeters. For FCC-hh, the terms are listed in Table 1.

	$ \eta < 1.7$	$1.7 < \eta < 4.0$	$4.0 < \eta < 6.0$
S_{ECAL}	10%	10%	30%
C_{ECAL}	0.7%	0.7%	3.5%
S_{HCAL}	50%	60%	100%
C_{HCAL}	3%	3%	10%

Table 1: The stochastic and constant terms of the energy resolution of ECAL and HCAL as a function of pseudorapidity in the conceptual detector design of FCC-hh [20].

One of the significant challenges is managing the high radiation levels and particle fluxes, which require robust radiation-hard materials and advanced cooling systems. The detectors must also handle high levels of pile-up, where multiple proton-proton collisions occur in the same bunch crossing, complicating data analysis. In the ultimate scenario when FCC-hh runs with an instantaneous luminosity of $30 \times 10^{34} \text{ cm}^{-2}\text{s}^{-1}$, the average pile-up is projected to reach a maximum value of 1000. In our study of highly boosted jets, we have neglected the impact of pile-up. Over 25 years of operation, it is expected to collect 30 ab^{-1} of data.

In the following section, we provide an overview of the simulation details employed for generating signal and background events.

4 Simulation of events

We generated the following standard model (SM) processes: QCD dijet production ($pp \rightarrow jj$), pair-production of top and anti-top quarks ($pp \rightarrow t\bar{t}$), pair production of W boson ($pp \rightarrow W^+W^-$), as the source of boosted QCD jets, top jets, and W jets, respectively. These samples are generated using PYTHIA 8 [175] with NNPDF 2.3 LO PDF [176]. We generate the samples in five bins according to p_T of the boosted jet that we wish to tag. The p_T bins considered in this study are 2–4 TeV, 4–6 TeV, 6–8 TeV, 8–10 TeV, 10–12 TeV, 12–14 TeV, and 14–16 TeV.

Figure 4 shows the cross-section of the processes as calculated by PYTHIA 8. The QCD di-jet events have the largest cross-section. At lower energies, the SM $t\bar{t}$ is the next dominant process, while at higher energies, the SM WW process has a higher cross-section.

As discussed in Section 2, we consider three BSM processes - the Z' production with $f\bar{f} \rightarrow Z' \rightarrow t\bar{t}$, which results in two top jets in the final state, the neutral heavy Higgs boson (H) production that decays to two W jets using the $pp \rightarrow H \rightarrow W^+W^-$ process, and the

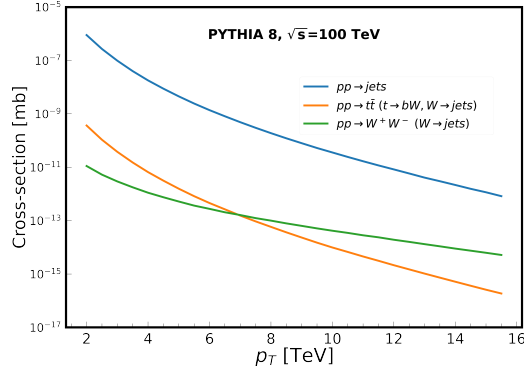


Figure 4: Cross-section as a function of p_T at FCC-hh for the three major SM background processes considered in this study: $pp \rightarrow jj$, $pp \rightarrow t\bar{t}$, $pp \rightarrow W^+W^-$.

$pp \rightarrow jB'$ production, with the singlet B' decaying to a t and a W . The generation procedure of the signal benchmarks has been discussed previously.

The backgrounds of the above BSM processes also include many other SM processes, which have been simulated for the analysis. These include SM $pp \rightarrow WZ$, and $pp \rightarrow ZZ$, which have been generated using PYTHIA 8. Other processes like SM $pp \rightarrow W + \text{jet}$ and SM $pp \rightarrow Z + \text{jet}$ have been generated using MADGRAPH 5, followed by showering and hadronisation via PYTHIA 8. In all the cases, we only consider the hadronic decay of the W boson. These backgrounds have not been included in the training samples, but are only considered during the BSM analysis later.

For our analysis, we have multiplied the cross-sections of QCD, $t\bar{t}$, VV , and $V + \text{jets}$ ($V = W^\pm/Z$) processes with a k-factor of 2 to approximately account for the higher-order corrections. For the signal, we have not used any k-factor.

All the above-mentioned samples are passed through DELPHES 3.5.0 [174] simulation of a typical FCC-hh detector. Table 2 shows the resolution of the tracking system and the $\eta - \phi$ segmentation of the Electromagnetic Calorimeter (ECAL) and Hadronic Calorimeter (HCAL) of FCC-hh as parametrised in [89].

The tracking efficiency for charged hadrons and the identification efficiency used by DELPHES for electrons, muons, and photons are listed in Table 12 in Appendix B. In case of two or more tracks lying within the angular resolution σ_θ , only the track with the highest momentum is reconstructed.

We relied on the particle-flow (PF) event reconstruction in DELPHES, which is based on a simplified approach that combines momentum and energy measurement from the tracking

Tracker		
$ \eta < 6.0$	$\sigma_\theta = 0.001$	
Calorimeters		
	ECAL	HCAL
$ \eta < 2.5$	$(\Delta\eta, \Delta\phi) = (0.01, 0.012)$	$(\Delta\eta, \Delta\phi) = (0.025, 0.025)$
$2.5 < \eta < 6.0$	$(\Delta\eta, \Delta\phi) = (0.025, 0.025)$	$(\Delta\eta, \Delta\phi) = (0.05, 0.05)$

Table 2: Angular resolution of the tracking system and segmentation in the Electromagnetic and Hadronic calorimeters of FCC-hh as parametrised in [89].

systems as well as calorimeter towers for event reconstruction. The algorithm is based on the complementarity between track momentum resolution and calorimeter energy resolution. For electrons and charged hadrons, the FCC-hh tracker provides excellent resolution up to $E = 500$ GeV and $E = 2$ TeV respectively, beyond which the calorimeter measurement dominates [89]. *Particle-flow tracks* are reconstructed for each charged object with an associated track. Neutral objects like photons, neutral hadrons, and charged hadrons with no associated tracks have significant energy deposits in the calorimeters. If the energy deposited in the calorimeters exceeds that measured from tracks, the final measurement is calculated as the difference between the two. These are reconstructed as *particle-flow photons* and *particle-flow neutral hadrons*.

FASTJET 3.4.2 [177, 178] is used on the PF candidates to construct jets of radius $R = 0.8$. We choose $R = 0.8$ because it is a typical choice of jet radius for large-radius jets in the LHC experiments. In the next section, we study the disadvantages of using fixed-radius jets. To mitigate the disadvantages, we also discuss the usage of dynamic radius jets. We select jets that satisfy the pseudorapidity cut of $|\eta| < 2.5$. These jets are then passed through the default flavour tagger modules of DELPHES. In this paper, we have not considered pile-up, which is left as an open topic for future studies.

The ML taggers are originally trained on 1M QCD jets, 1M top jets, and 1M jets distributed over seven p_T bins. The dataset is split in an 80:20 ratio between training and validation. Model performance is evaluated on an equivalent, independent test set. Finally, for the BSM analysis, we generate 560K jj , 560K $t\bar{t}$, 560K tW , 560K VV , and 560K Vj events, where $V = W, Z$, over seven different p_T bins.

5 Challenges and mitigation strategies for jets at $\sqrt{s} = 100$ TeV

At the 100 TeV collider, the high center-of-mass energy of pp collisions produces heavy BSM particles with masses up to tens of TeV. When such particles decay into jets, the jets are highly

boosted and thus highly collimated. In our study, we consider top and W jets with p_T ranging from 2 TeV to 16 TeV. As a consequence of poor jet energy resolution at very high p_T , we need to construct a tagger that caters to multiple p_T ranges because the characteristics of jets vary widely across the entire p_T range (see Appendix A). Reconstructing boosted particles from their final state requires addressing the unique challenges posed by these extreme energies. This section explores these challenges and discusses potential techniques to overcome them.

5.1 Effect of fixed jet radius on top and QCD jet mass

At sufficiently large boosts, the final-state hadrons from decays of resonances (like W boson or top quark) merge into a single jet. The jet mass is a potent discriminator between resonance jets and background QCD jets (i.e., jets originating from the light-flavour quarks or gluons). The distribution of jet mass (m_{jet}) for the top and QCD jets constructed with the radius of the jet, $R = 0.8$, is shown in Figure 5. The jets carry p_T in the range of 2–4 TeV, 6–8 TeV, 10–12 TeV, and 14–16 TeV.

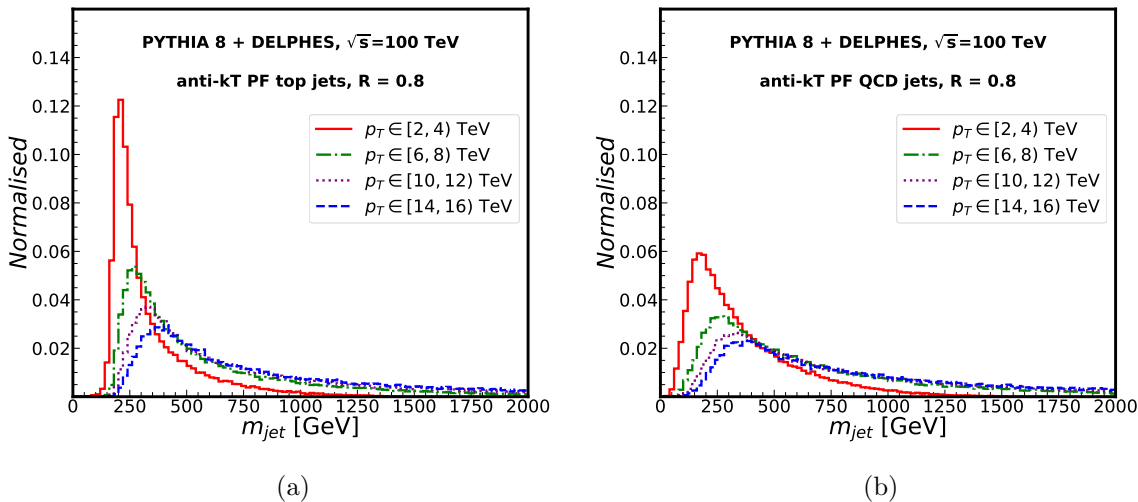


Figure 5: Normalised m_{jet} distribution of (a) top jets and (b) QCD jets with transverse momenta (p_T) of 2–4 TeV, 6–8 TeV, 8–10 TeV, and 14–16 TeV. Jets have been constructed with a fixed jet radius $R = 0.8$.

The mean squared invariant mass of a QCD jet in the collinear approximation is given by [179–181],

$$\langle m^2 \rangle \simeq C \cdot \frac{\alpha_S}{\pi} p_T^2 R^2 \quad (5.1)$$

where C is a coefficient that depends on the jet algorithm. At high p_T and with a fixed jet radius R , the mass increases, as shown in Figure 5. In addition, the jet captures contamination from the initial-state radiation (ISR), final-state radiation (FSR), and underlying events (UE). As described in [181], in the case of highly boosted top jets, the FSR from the top quark is not dead-cone suppressed any more, as the dead cone radius shrinks as $\simeq m_{\text{top}}/p_T$ for very high p_T . On the other hand, a single emission at the jet boundary with transverse momenta $p_{T,ISR}$ can substantially change the jet mass, as

$$m^2 \simeq m_{\text{top}}^2 + p_T \cdot p_{T,ISR} \cdot R^2 \quad (5.2)$$

The authors in [181] showed that an ISR jet with transverse momenta $p_{T,ISR} \sim m_{\text{top}}^2/p_T R^2$ can change the jet mass by $\mathcal{O}(1)$. At the FCC, where p_T can reach tens of TeV, radiative emissions of a few GeV can alter and increase the jet mass. The large tail in the jet mass distribution manifests in QCD jets, too, as seen in Figure 5b.

Jet grooming algorithms are applied to jets to remove contaminating radiation from uncorrelated sources, with the aim of improving the jet mass scale and resolution. However, they are not optimised for high p_T jets [182]. As a result, when grooming algorithms such as the soft drop technique are applied to fixed radius high- p_T jets, observables like the jet mass still possess the problem of a long tail in distributions (see Figure 25 in Appendix C).

To mitigate the above issues and reduce the contamination, we make use of a dynamic jet radius. Dynamic jet radius has already been used at the LHC for various studies [183–185]. The choice of the jet radius R is crucial because not only should the jet algorithm reconstruct the top quark well, but it also should be able to mitigate the contamination from underlying events. In the following section, we construct the dynamic radius using parton decay information.

5.1.1 Jet radius estimation at the parton level

To choose the radius that captures the correct jet substructure, we go back to the parton-level information of top jets. The top quark (t) decays to a b quark and a W boson, which in turn decays hadronically to a light quark and an anti-quark, which we shall refer to as u and d .

The top decay products lie within a cone, whose size depends on the initial p_T . For events in each bin, we calculate the distance ΔR between the parent top quark t and its three daughter quarks, b , u , and d . We then find out the maximum of the three distances, $\Delta R^{\text{max}} = \max(\Delta R_{tb}, \Delta R_{tu}, \Delta R_{td})$. ΔR^{max} serves as an approximate measurement of the cone size. We expect that this number decreases with increasing p_T . Figure 6a displays a two-dimensional matrix of the p_T ranges and the ΔR^{max} values. Each square shows the percentage of top jets with p_T in the i^{th} bin and j^{th} ΔR^{max} .

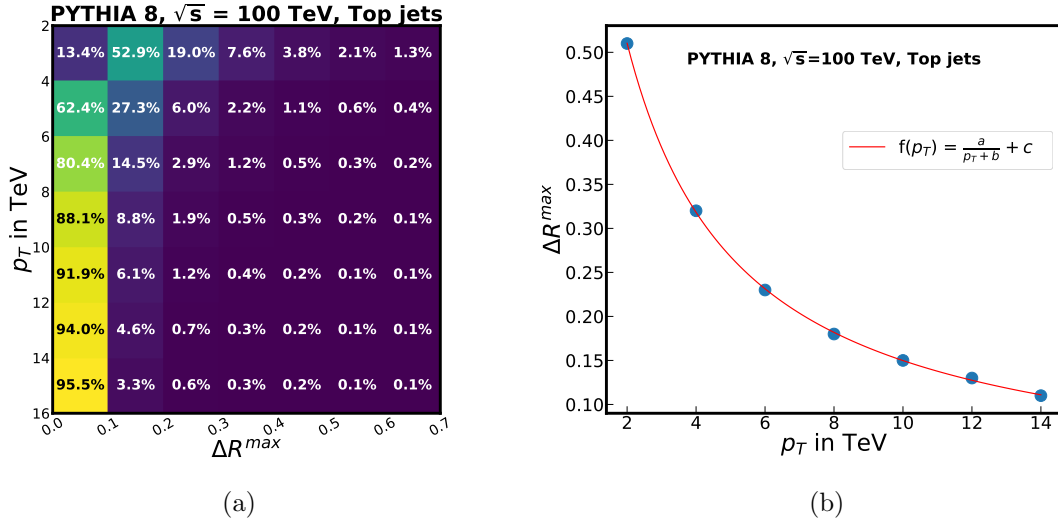


Figure 6: (a) A two-dimensional matrix showing the percentage of $t \rightarrow bW(W \rightarrow ud)$ events that have all the three daughter partons within radius ΔR^{max} from the mother top quark. (b) The variation of the ΔR^{max} value with 95% success rate of containing the full top decay, as a function of the p_T of the top quark. Here, $f(p_T)$ is the fitting function.

From Figure 6a, we see that as we move on to higher p_T , the top jets have smaller decay cone size, as denoted by the smaller ΔR^{max} . Only 13.4% of tops generated with p_T of 2–4 TeV have the b , u , and d contained fully within $\Delta R = 0.1$, while in the case of 14–16 TeV tops, the number is 95.5%. Using this information, we can estimate the cone radius that should be used so that a reconstructed jet contains the full information of the top.

We determine the ΔR^{max} value such that the top quark decay products, b , u , and d , are fully contained within a cone of this radius 95% of the time. We assign this ΔR^{max} value to the lower value of the corresponding p_T bin. For instance, if the top quarks in the 2–4 TeV have a ΔR^{max} of 0.5, we use 0.5 for 2 TeV. Similarly, if the 4–6 TeV bin has a ΔR^{max} of 0.3, we use 0.3 for 4 TeV, and we follow this for all the remaining bins. In Figure 6b, we have plotted the ΔR^{max} corresponding to each p_T bin. We fit the data points using a function of the form,

$$f(p_T) = \frac{a}{p_T + b} + c \quad (5.3)$$

where a , b , and c are fitting parameters, which are set to 1.64, 1.3, and 0.001, respectively. The dependence of R on the inverse p_T is inspired by the approach in [181]. As the p_T reaches ≈ 15.7 TeV, ΔR^{max} goes below 0.1.

In the later part of our work, we use the function to calculate the jet radius dynamically instead of using a fixed radius.

As stated earlier, we construct anti- k_T jets using FASTJET on particle-flow (PF) objects, using a fixed radius of 0.8. Now we recluster the jet constituents using the p_T dependent function in Equation 5.3. Figure 7 shows the distributions of jet mass for top jets and QCD jets after reclustering.

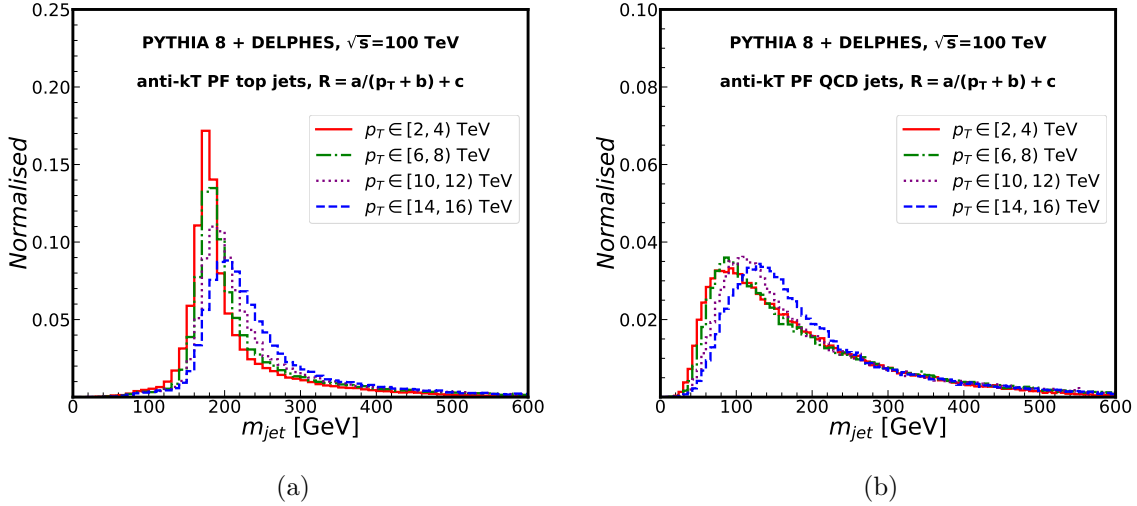


Figure 7: Normalized m_{jet} distribution of (a) top jets and (b) QCD jets with transverse momenta (p_T) of 2–4 TeV, 6–8 TeV, 8–10 TeV, and 14–16 TeV. The jet constituents have been reclustered using radius $R(p_T) = a/(p_T + b) + c$.

As seen in Figure 7a and 7b, using a dynamic jet radius that is a function of the jet’s p_T corrects the jet mass. The jet mass falls off faster in this case. However, the peak of the jet mass and the width of the distribution still increase with increasing p_T . This indicates that even with the new dynamic radius, the contamination could not be completely eliminated.

5.2 Effects of finite detector resolution on top and QCD jet mass

To further investigate the source of the high jet mass, we look into the detector parametrisation of the 100 TeV collider because the energy-momenta of the jet constituents depend to a large extent on the resolution of the detector elements. As stated in Section 4, we use the DELPHES modeling of the FCC-hh detector for simulation. The resolution used in the calorimeters and the tracking system is listed in Table 2 in Section 3. Since we are using particle-flow (PF) objects, consisting of tracks and calorimeter towers, we focus on the resolution effects of these two detector elements.

5.2.1 Calorimeters

The DELPHES algorithm iterates over a collection of tower hits and processes them to fill a tower by adding the total energy deposited in the tower. The tower's $\eta - \phi$ is then calculated as the $\eta - \phi$ of the cell's geometric centre, smeared by a Gaussian distribution. The four-momentum of the tower is recalculated from the η, ϕ, E information.

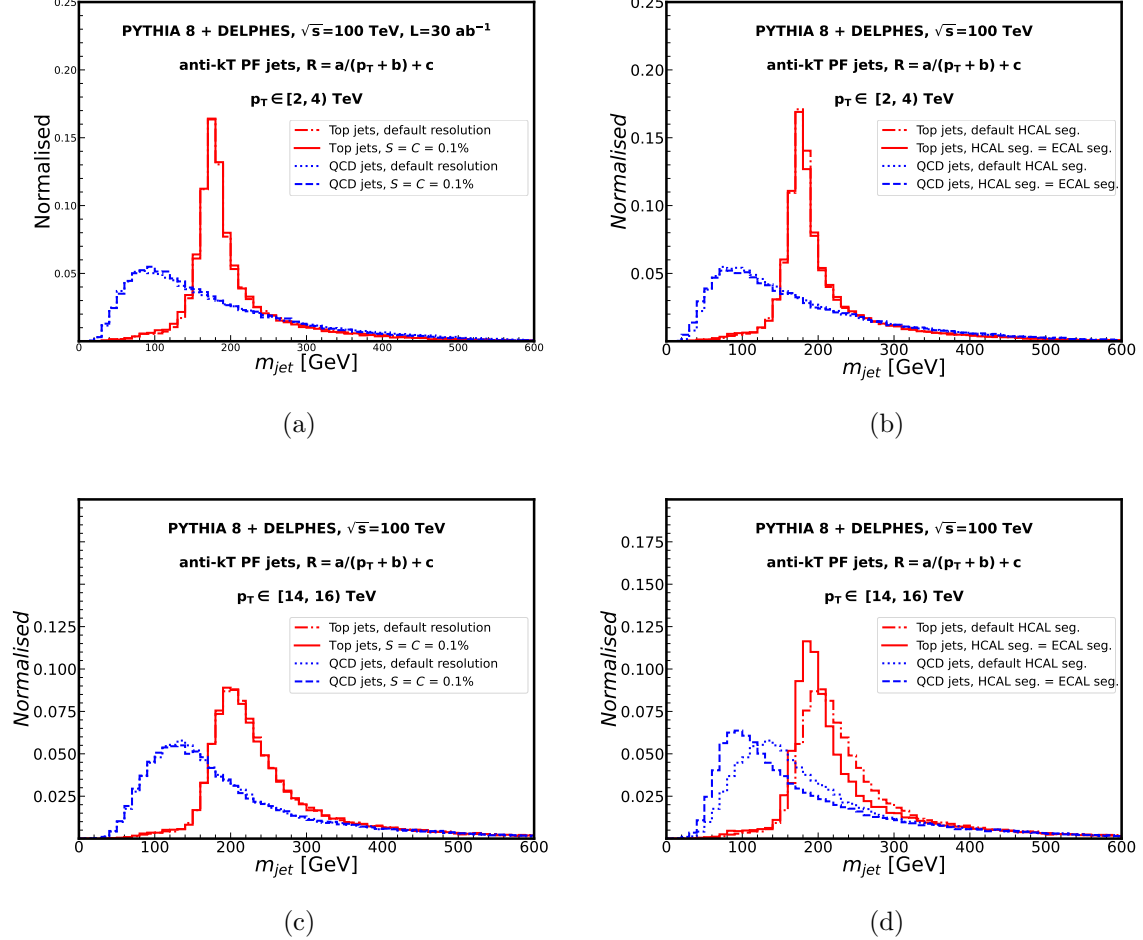


Figure 8: Normalised m_{jet} distribution of 2–4 TeV ((a), (b)) and 14–16 TeV ((c), (d)) top jets and QCD jets using different calorimeter configurations. Subfigures (a), (c) show the change in m_{jet} when the energy resolution is varied. Subfigures (b), (d) show the change in m_{jet} when the angular resolution is varied.

With a poorer energy resolution and granularity than the values that are currently under consideration, the jet mass resolution worsens (see Figure 24 in Appendix A). To examine the opposite effect, we construct two hypothetical scenarios in which the energy resolution

and granularity are improved relative to the present values. First, we set the stochastic and constant terms in the ECAL and HCAL resolution parameter σ to a very low value of 0.1%, i.e., $S = C = 0.1\%$. This reduces the extent to which the energy can be smeared. Then, we use a more granular segmentation of the HCAL by setting the cell size of HCAL towers to that of the ECAL towers. Reducing the HCAL cell size increases the number of cells within the jet clustering radius. Figure 8 shows the jet mass distribution for 2–4 TeV jets (Figures 8a, 8b) and for 14–16 TeV jets (Figures 8c, 8d).

Improving the energy resolution did not affect the jet mass reconstruction. On the other hand, increasing the $\eta - \phi$ segmentation of the HCAL towers by a factor of two changes the reconstructed jet mass substantially for the 14–16 TeV jets, although it does not affect the 2–4 TeV jets. The 14–16 TeV top jets have a sharper peak, and the overlap between the top and the QCD jets increases as the QCD distribution peaks at lower values. The improved angular resolution of the HCAL allows the highly collimated decay products of the 14–16 TeV to deposit energy in an increased number of highly granular tower cells, causing the PF reconstruction to be more efficient when matching the charged tracks to towers. For 2–4 TeV jets, the default segmentation already offers sufficient granularity to resolve the particles, hence increasing the segmentation does not provide much improvement.

To conclude, we find that in the study of ultra-boosted objects, granularity plays a more important role than energy resolution, as seen in Figure 8d. If such a fine granularity, where HCAL and ECAL cell sizes are of the same size, is indeed feasible to construct at the FCC-hh experiment, it will improve the mass reconstruction of highly boosted objects. However, we continue our study with the currently proposed granularity of ECAL and HCAL. We can also obtain a high angular resolution by using charged particle tracks, which we study in the next section.

5.2.2 Tracking system

The proposed angular resolution for tracking in the FCC detector design is $\sigma_\theta = 0.001$, which is an order of magnitude less than that of the ECAL. When two or more tracks are separated with a distance less than σ_θ , the one with the maximum p_T is considered by the dense track filtering algorithm in DELPHES. We calculate the mass on the constituent tracks of the PF jet with reclustered radius (m_{trk}). We also compute $m_{\text{jet}}^{\text{trk}}$ with a degraded tracking resolution, $\sigma_\theta = 0.005$. Figure 9 shows the distribution of mass calculated on tracks for 2–4 TeV (9a) and 14–16 TeV jets (9b), with two values of the σ_θ .

The mass distribution for tracks assumes lower values because they do not capture the full energy of a jet. Additionally, as we see in Figure 9, $m_{\text{jet}}^{\text{trk}}$, especially for top jets, is very sensitive to the angular resolution. The track-based mass needs to be rescaled with a ratio of

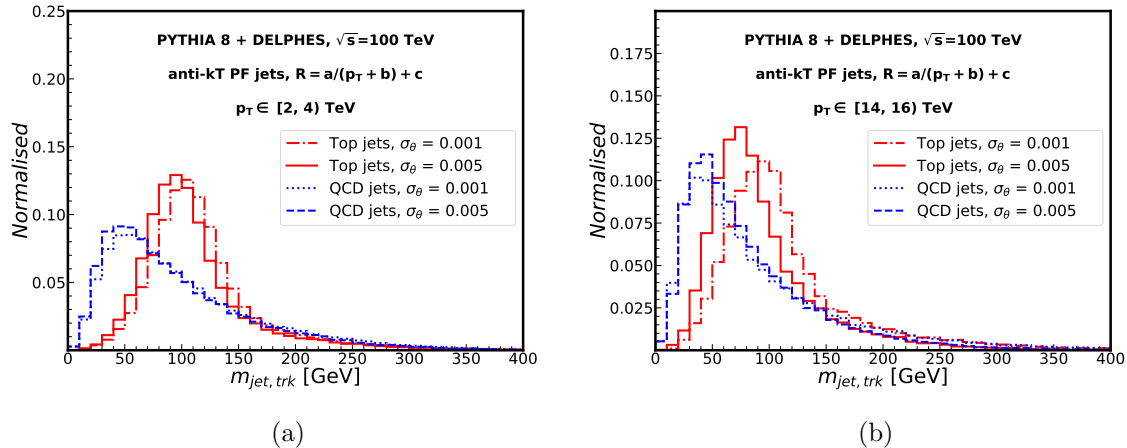


Figure 9: Normalised track-based m_{jet} distribution of (a) 2–4 TeV and (b) 14–16 TeV top jets and QCD jets with varying angular resolution of the tracker.

the original jet p_T to the track p_T [181] if we want to obtain the correct estimation of the jet mass. In the next section, we perform a similar study and check the detector effects on the jet substructure.

5.3 Effects of finite detector resolution on N-Subjettiness observables

For the purpose of identifying the top jets and QCD jets based on their substructure properties, a popular method is the use of the N-Subjettiness [25] (τ_N) observable, which measures the *prongness* of a jet relative to N subject directions \hat{n}_j ,

$$\tau_N^{(\beta)} = \frac{1}{\sum_{\alpha \in \text{jet}} p_{T,\alpha} R_0^\beta} \sum_{\alpha \in \text{jet}} p_{T,\alpha} \min_{k=1,\dots,N} (\Delta R_{k,\alpha})^\beta \quad (5.4)$$

where $\Delta R_{k,\alpha}$ is the separation between the α -th jet constituent and the k -th axis, β (which should be greater than zero) is an arbitrary weighting exponent to guarantee infrared safety, and R_0 is a radius parameter. For a jet having N subjets, $\tau_N < \tau_{N-1}$ and the ratio τ_N/τ_{N-1} is small.

In top quark decays, which yield three distinct subjets, the ratio τ_3/τ_2 is expected to exhibit a peak at lower values, distinguishing it from the QCD background, which peaks at higher values. Figure 10 shows the distributions of $\tau_{32}^{(1,0)} = \tau_3/\tau_2$ for 2–4 TeV and 14–16 TeV jets with modifications to the energy and the angular resolution of the calorimeters.

To begin with, we note that the discrimination between top and QCD jets in terms of $\tau_{32}^{(1)}$ degrades with an increase in the transverse momenta of the jets. Not only is there a

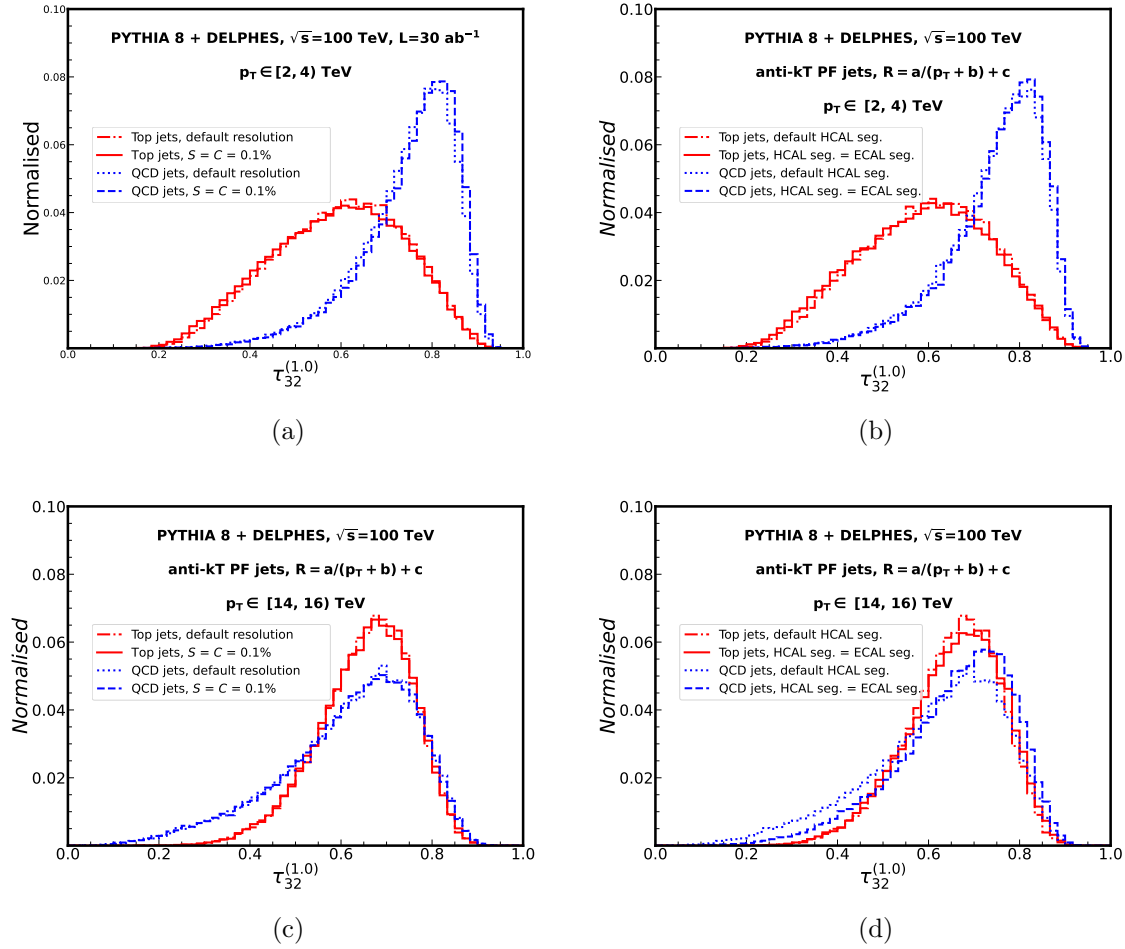


Figure 10: Normalised $\tau_{32}^{(1,0)}$ distribution of 2–4 TeV ((a), (b)) and 14–16 TeV ((c), (d)) top jets and QCD jets using different calorimeter configurations. Subfigures (a), (c) show the change in $\tau_{32}^{(1,0)}$ when the energy resolution is varied. Subfigures (b), (d) show the change in $\tau_{32}^{(1,0)}$ when the angular resolution is varied.

greater overlap between the two for 14–16 TeV jets, but the top and the QCD jets follow reverse trends in τ_{32} . In other words, the N-Subjettiness observable breaks down at high transverse momenta, even with the $(\Delta\eta, \Delta\phi) = (0.01, 0.01)$ calorimeter resolution at the FCC-hh. Improving the HCAL resolution corrects the observable to some extent, but it is not sufficient to be advantageous as a tagger. Variable τ_{21} also exhibits similar behavior. We now calculate the observable on the tracks.

Figure 11 shows that an angular resolution of 0.001 in the tracker is beneficial for the boosted jets. The finer track resolution restores the correct substructure properties of the

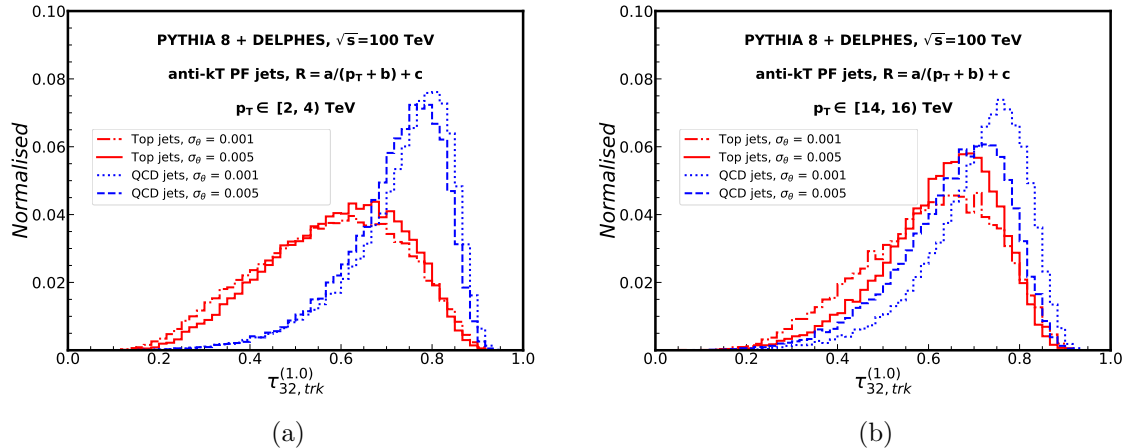


Figure 11: Normalised track-based $\tau_{32}^{(1,0)}$ distribution of (a) 2–4 TeV and (b) 14–16 TeV top jets and QCD jets with varying angular resolution of tracker.

14–16 TeV jets. As in the case of jet mass, decreasing σ_θ degrades the N-Subjettiness.

From our studies of the detector effects on the jet mass and τ_{32} , we make the key observation that a full and accurate reconstruction of the momentum and the jet substructure at tens of TeV is limited by finite resolution of the calorimeters. Even the DELPHES particle-flow reconstruction that uses both track and calorimeter information fails to resolve the substructure at high p_T . However, particle flow algorithms developed in actual experiments may be built with mechanisms to make up for resolution issues and achieve at least as good a tracking-only reconstruction.

The tracker volume with the proposed angular resolution of $\sigma_\theta = 0.001$ comes to the rescue. Solely track-based N-Subjettiness captures the *prongness* successfully. However, one must keep in mind that this is the best-case scenario that does not take pile-up into consideration. Further studies with pile-up are required to see if the track-based observables work in that situation.

5.4 Boosted W jets at $\sqrt{s} = 100$ TeV

As discussed in Section 2, the production of a vector-like quark (VLQ) B' at the FCC-hh that can decay into a top quark and a W boson is not only a source of highly boosted top jets but also highly boosted W jets. Figure 3c shows the full range of transverse momenta of such W jets coming from the decay of a B' , reaching up to 12 TeV for a B' of mass $m_{B'} = 10$ TeV. In the previous section, we discussed the challenges that may arise while reconstructing top jets and the possible ways to mitigate them. First, we cluster the PF candidates with a radius R

that is p_T dependent. This reduces the contamination by radiative effects. Next, we saw that the track-based jet substructure observable τ_{32} acts as a potent discriminant between the top and the QCD jets, even at high p_T . Similar challenges shall arise while reconstructing the W boson.

To study boosted W jets, we pair-produce W boson from a pair of quarks at $\sqrt{s} = 100$ TeV, where the W boson further decays hadronically to two light quarks. We follow the same simulation procedure as described in Section 4. We use the dynamic radius $R(p_T) = a/(p_T + b) + c$ that was optimized for top jets to cluster the particle-flow objects. Figure 12 shows the jet mass distribution of the boosted W jets for four different p_T ranges, with a fixed radius (Figure 12a) and a dynamic radius (Figure 12b).

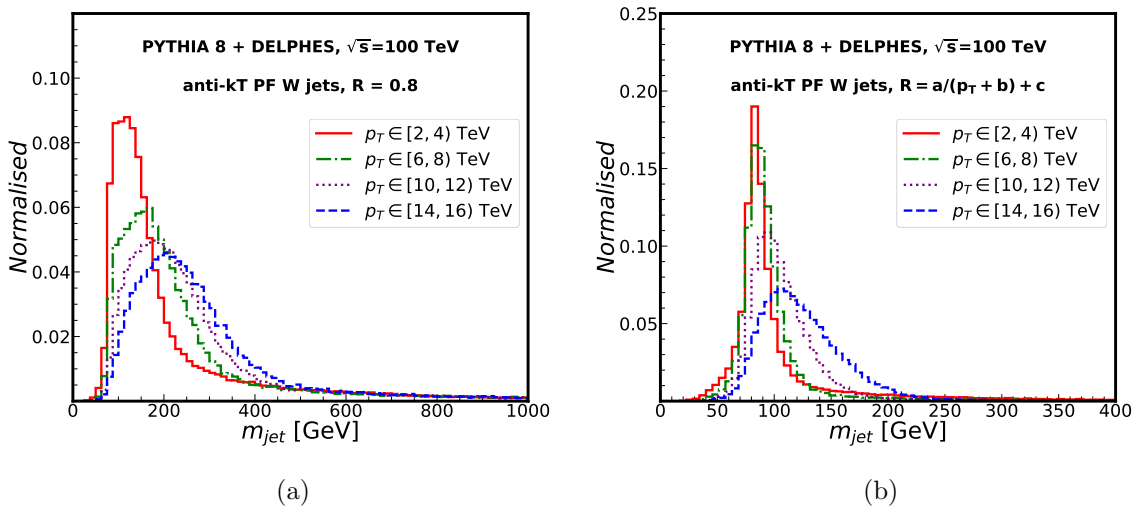


Figure 12: Normalised m_{jet} distribution of W jets (a) before and (b) after reclustering with $R(p_T)$.

As in the case with top and QCD jets, the W jet mass also suffers from radiation at the $\sqrt{s} = 100$ TeV collider though being an electroweak process, the amount is less than that in the former cases. Using the radius $R(p_T)$, much of the radiative effects could be removed. For $p_T \in [2, 4]$ TeV jets, the mass is exactly reconstructed at the W boson mass ($m_W \simeq 80$ GeV). With increasing p_T , the jet mass peak shifts to higher values due to increasing radiative effects and the worsening resolution of the detector.

Figure 13 shows the distributions of the jet mass and the two-prong N-Subjettiness ratio τ_{21} calculated on tracks for the W jets and the QCD jets from the two extreme ends of the p_T spectrum. Both W and QCD peak at ~ 50 GeV, though QCD features a much longer tail. The track-based τ_{21} shows distinguishing properties between the W and the QCD jets,

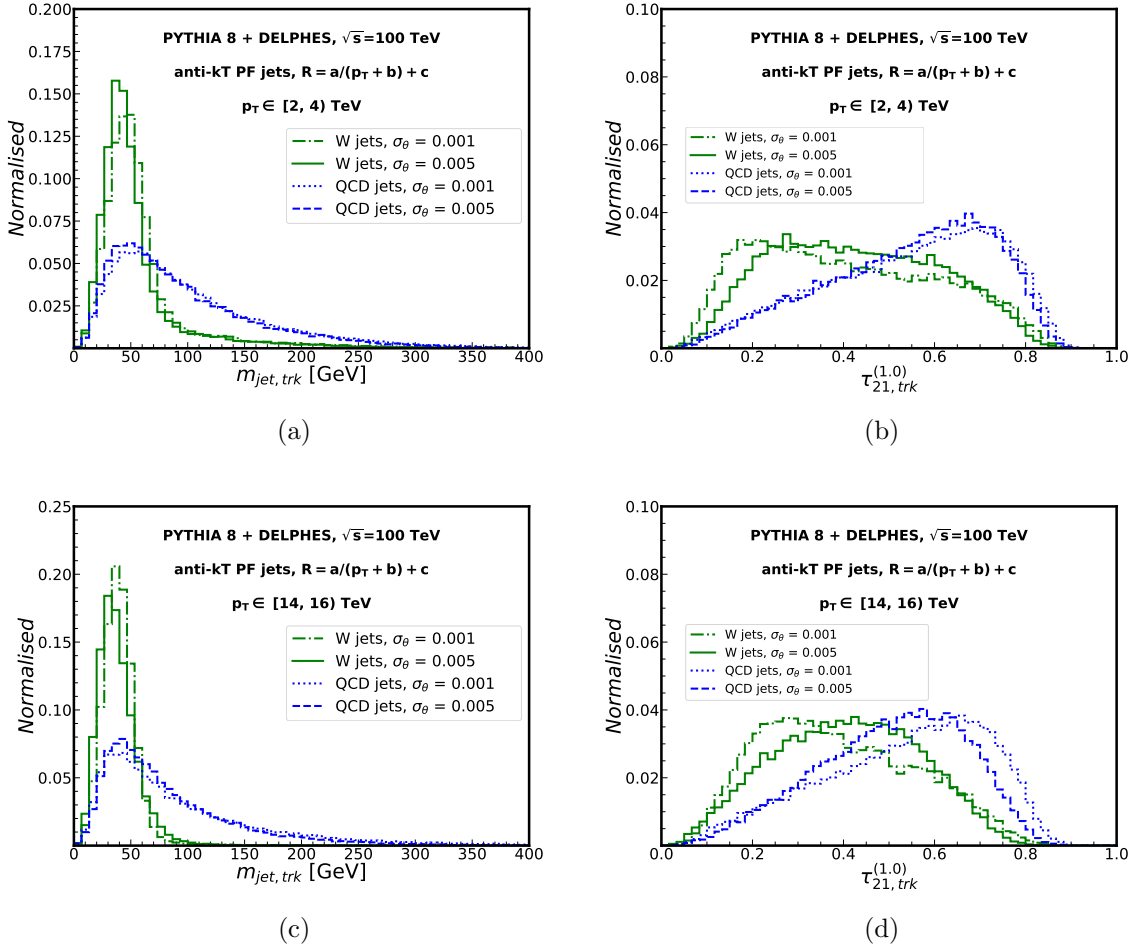


Figure 13: Normalised track-based m_{jet} and $\tau_{21}^{(1.0)}$ distributions of 2–4 TeV ((a) and (b) respectively) and 14–16 TeV ((c) and (d) respectively) top jets and QCD jets with varying angular resolution of the tracker.

the former peaking at lower values owing to the two-prong substructure. With the poorer resolution of tracks, the two tend to overlap with each other.

Using a radius optimized for W jets (using the parton level information of $W \rightarrow q\bar{q}$) could eliminate more of the radiation from the jets. We have used the dynamic radius optimized for top jets while reclustering the W decay products because we primarily wanted to study boosted top signatures. In the next section, we discuss the possibility of making further improvements to the reconstructed jets through jet grooming algorithms.

5.5 Jet grooming techniques

Initial-state radiation and the underlying event can substantially alter the measured jet mass. Jet grooming algorithms are applied to jets to remove contaminating radiation from uncorrelated sources, with the aim of improving the jet mass scale and resolution.

While the reclustering technique using a dynamic p_T dependent jet radius prevented ISR, FSR, and multi-parton interactions (MPI) contamination within the jets, we want to see if standard grooming techniques can do better in reducing the residual radiation.

We use the soft drop technique [182, 186] on the jets. The original jet with $R = 0.8$ is first reclustered within $R(p_T)$ using the Cambridge/Aachen (C/A) algorithm instead of the anti- k_T algorithm to form a structured tree with angular ordering. Then, the tree is declustered using the following algorithm:

1. Undo the last step of C/A clustering to break the jet j into two subjets j_1 and j_2 .
2. Check if j_1 and j_2 satisfy the condition:

$$\frac{\min(p_{T_1}, p_{T_2})}{p_{T_1} + p_{T_2}} > z_{\text{cut}} \left(\frac{\Delta R_{12}}{R_0} \right)^\beta \quad (5.5)$$

where the two parameters, z_{cut} , the soft drop threshold, and the angular exponent β controls the degree of jet grooming.

3. If the above condition is not satisfied, remove the softer subjet, redefine j to be the harder subjet, and reiterate steps 1 and 2 until criteria 5.5 is satisfied.
4. If the two branchings of jet j pass the condition, j is the final soft dropped jet.

We vary the parameters used for soft drop: $z_{\text{cut}} = 0.05, 0.08, 0.10, 0.20$, and $\beta = 0.2, 0.5, 1.0, 2.0$. Appendix C shows the m_{jet} distributions of top, W , and QCD jets for all possible combinations of the parameters. We calculate the Wasserstein-1 distance [187], a measure of the separation between two distributions, between the m_{jet} distributions of top, QCD, and W jets, and choose the parameters $z_{\text{cut}} = 0.05$, $\beta = 0.5$ that maximize this distance for the two extreme ends of our p_T range. Figure 14 shows the distribution of the top and the QCD jet mass after using the soft drop algorithm, with $z_{\text{cut}} = 0.05$, $\beta = 0.5$ for $p_T \in [2, 4]$ TeV and $p_T \in [14, 16]$ TeV jets.

Applying softdrop after reclustering with $R(p_T)$ leads to increased separation between top and QCD jets; however, the separation is reduced between top and W jets, and between W and QCD jets. The secondary peaks in the m_{jet} distributions of top and W jets appear when the condition in Equation 5.5 removes one of the softer prongs from the multi-pronged

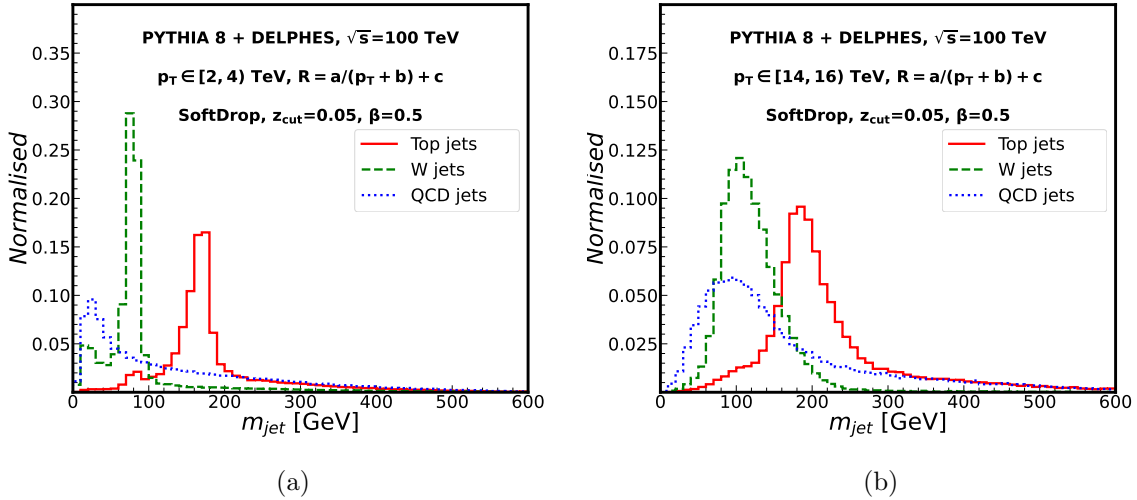


Figure 14: Normalised m_{jet} distribution of (a) 2–4 TeV and (b) 14–16 TeV top jets and QCD jets, after applying softdrop grooming with parameters $z = 0.05$, and $\beta = 0.5$.

jets. This is more evident in 2–4 TeV jets. In 14–16 TeV jets, along with the prongs carrying enough energy to satisfy Equation 5.5, the high boost concentrates the jet constituents with much smaller angular separation.

6 Machine learning techniques for jet tagging

Our goal in the following sections is to perform multi-class classification using these observables as well as jet images to explore how machine learning distinguishes between the three categories of jets in the $\mathcal{O}(1) - \mathcal{O}(10)$ TeV range. The motivation behind designing a multi-class tagger instead of separate binary classifiers is due to its ability to tackle scenarios involving multiple jet types in the final states. For example, in the decay of a vector-like quark (VLQ) B' , both t and W jets are produced, making it essential to simultaneously distinguish between top, W , and QCD jets. Additionally, $t\bar{t}$ jets form a substantial background for BSM processes involving W^+W^- final states, just as W jets can become a major background for BSM processes with $t\bar{t}$ in the final state. A multi-class tagger effectively addresses these challenges within a single framework.

We first introduce the machine learning (ML) models used in this work for top tagging and W tagging purposes. We generate top jets, QCD jets, and W jets using the process described in Section 4. We have used two kinds of ML algorithms in our work: the image-based convolutional neural network (CNN) that uses low-level inputs in the form of jet images

and the variable-based XGBoost that uses high-level, physics-motivated input features such as jet substructure observables. The choice of these simple models is to build a foundation based on how well these models work at a 100 TeV collider, before moving on to advanced machine learning taggers, which can be a point of further study.

We do not perform b tagging on the top jets in our analysis to ensure a fair comparison of top, W, and QCD tagging via multi-class classification using only jet substructure observables and jet images. However, we discuss the effect of b tagging briefly in Section 7.1. We build and train the ML models separately for each p_T range. This is because, as described earlier, the features have a large variation, going from 2 TeV to 14 TeV. We end up with 7 XGBoost and 7 CNN classifiers. We now briefly discuss the architecture of the algorithms below.

6.1 Extreme Gradient Boosted Decision Trees

XGBoost, or eXtreme Gradient Boosting [84], is an efficient, robust, and scalable implementation of gradient boosting machines. It is extensively utilized in machine learning due to its impressive speed and performance. XGBoost operates by creating an ensemble of decision trees, where each new tree attempts to correct the errors of the previous ones using a gradient descent algorithm, ultimately minimising the loss function. The key parameters of the XGBoost model include `objective` (loss function), `num_round` (boosting iterations), `learning_rate` (step size), `max_depth` (tree depth), `min_child_weight` (minimum instance weight), and `gamma` (minimum loss reduction). Regularisation parameters like `alpha` (L1 regularisation), `lambda` (L2 regularisation), `subsample` (training instance subsample ratio), `colsample_bytree` (feature subsample ratio) are used to reduce overfitting.

In our work, we use the XGBoost model for three-class classification between top jets, W jets, and QCD jets for the various p_T ranges. We use the multi-class logarithmic loss as the objective function to minimise. We use a `max_depth` of 3 and set the `learning_rate`, `colsample_bytree`, `colsample_bylevel`, `colsample_bynode` to 0.1, 0.3, 0.5, 0.3, respectively.

Using these parameters, we build the tree and use the high-level jet observables as input features. The observables m_{jet} and τ_{NN-1}^β have been calculated on four types of candidates: charged particle tracks (Obs_{trk}), particle-flow jets with radius $R(p_T)$ ($Obs_{rec.}$), particle-flow jets with radius $R(p_T)$ that have been groomed using soft drop algorithm (Obs_{SD}). We have divided them into several sets of input features. These are described as follows:

- Set 1: m_{jet} , m_{jet}^{SD} , $m_{\text{jet}}^{\text{trk}}$, N-Subjettiness ratios τ_{NN-1}^β where $N = 2-6$ and $\beta = 0.5, 1.0, 2.0$, calculated on reclustered jets before applying soft drop (τ_{NN-1}^β), after applying soft drop ($\tau_{NN-1,SD}^\beta$), and on tracks ($\tau_{NN-1,trk}^\beta$).
- Set 2: $m_{\text{jet}}^{\text{trk}}$, $\tau_{NN-1,trk}^\beta$ where $N = 2-6$ and $\beta = 0.5, 1.0, 2.0$.

- Set 3: $m_{\text{jet}}, m_{\text{jet}}^{SD}, m_{\text{jet}}^{\text{trk}}, \tau_{NN-1, \text{trk}}^\beta$ where $N = 2-4$ and $\beta = 0.5, 1.0, 2.0$.
- Set 4: $m_{\text{jet}}, \tau_{NN-1}^\beta$ where $N = 2-6$ and $\beta = 0.5, 1.0, 2.0$.
- Set 5: $m_{\text{jet}}^{SD}, \tau_{NN-1, SD}^\beta$ where $N = 2-6$ and $\beta = 0.5, 1.0, 2.0$.

Set 1 contains all the observables from $Obs_{\text{trk}}, Obs_{\text{rec.}}$, and Obs_{SD} . We include higher N-Subjettiness ratios as well as ratios with varying degrees of β parameter to form a comprehensive set of features. Set 2, 4, and 5 are composed of only $Obs_{\text{trk}}, Obs_{\text{rec.}}$, and Obs_{SD} , respectively. Set 3 is a mixed set of track observables (up to 4-Subjettiness) along with two jet mass observables — m_{jet} before and after soft drop.

Using these, we train the XGBoost. The Receiver-Operating-Characteristic (ROC) curve and the Area-Under-the Curve (AUC) are presented in Figure 15. AUC is the measure of how well a classifier can identify positives and negatives in data. A perfect classifier shall have $AUC = 1$. Figure 15a and 15b represent how well the classifier can identify top jets against the background of QCD jets and W jets. Figure 15c and 15d represent how well the classifier can identify W jets against the background of QCD jets and top jets. Set 1, being the most expansive set of features, performs the best in all the cases.

We also compare the performance of Set 1 observables using the same XGBoost model for multi-jet classification at the LHC with $\sqrt{s} = 14$ TeV. The classification performance is better at LHC energies for 2–4 TeV jets compared to that at the FCC-hh. This is possibly due to the difference in admixture of quark-initiated jets and gluon-initiated jets in the QCD background at LHC and FCC-hh, for the same p_T range. While at LHC, 2-4 TeV QCD consists of both quark-initiated and gluon-initiated jets in equal proportions ($(\frac{\sigma_{pp \rightarrow q\bar{q}}}{\sigma_{pp \rightarrow gg}})_{\text{PYTHIA 8 LO}} \sim 1$), at FCC-hh, 2-4 TeV QCD is mostly dominated by gluon-initiated jets. Gluon-initiated jets are more difficult to distinguish from top jets because of the increased number of splittings, hence the difference in performance.

Using solely track-based features (set 2) does not prove to be very advantageous, especially when identifying boosted W jets. Set 2 is outperformed by sets 3, 4, and 5, especially for W jet identification. In the multi-class tagger, the advantages of track-based features for top vs. QCD discrimination are offset by their inability to fully capture W jet information. One example is the $m_{\text{jet, trk}}$ variable. While it provides useful separation between top and QCD jets, there is significant overlap between $m_{\text{jet, trk}}$ of W jets and QCD jets.

The charged track multiplicity in W jets is low compared to top jets and QCD jets because of its two-prong decay (top decay has three hard prongs, and QCD jets emit soft radiation) and because W boson is less radiative. At high p_T the tracks from the two decay products overlap. The individual tracks carry more energy than tracks from top decay because

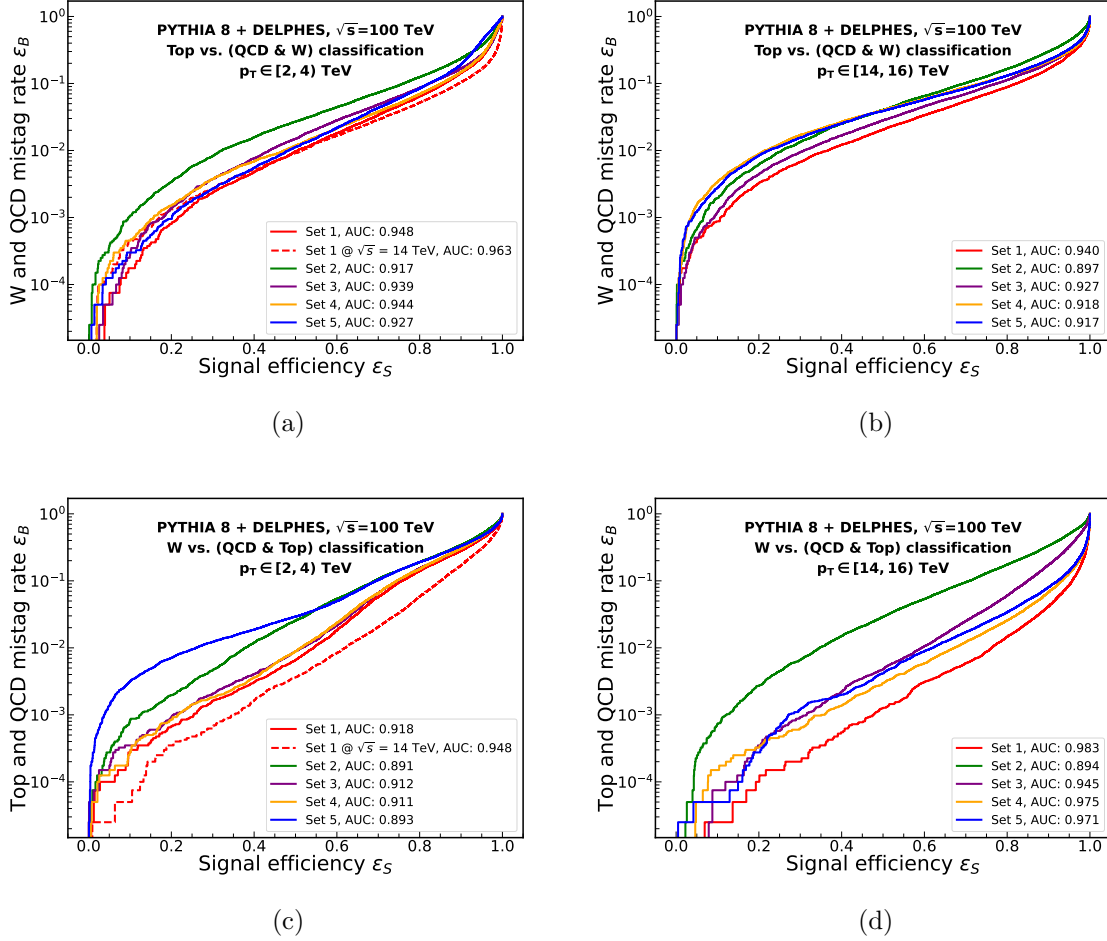


Figure 15: Receiver-Operating-Characteristic (ROC) curve and the Area-Under-the Curve (AUC) for multi-class classification. Figures 15a and 15b show the ROC for top vs. QCD and W classification for 2–4 TeV and 14–16 TeV jets, respectively. Figures 15c and 15d show the ROC for W vs. QCD and top classification for 2–4 TeV and 14–16 TeV jets, respectively. The red dotted lines in Figures 15a and 15c show the ROC for top vs. background and W vs. background classification ϵ_S respectively for 2–4 TeV jets generated at the LHC.

there are only two partons to share the energy. The collimation makes it harder to resolve the individual tracks. At 14–16 TeV, much of the information is lost due to overlapping hits in the tracker. This causes the track-based mass and other track-based observables to become less correlated with their particle-flow-based counterparts. On the other hand, less correlation leads to better separation from the top and QCD jets because the track-based and particle-flow-based features are more correlated in the latter case.

6.2 Convolutional Neural Networks (CNN)

Convolutional neural networks (CNNs) [85–87] are a powerful deep learning method designed to process visual data. The CNNs accept three-dimensional input images comprising height, width, and depth or channels. The core component of a CNN is the convolutional layer, which utilises two-dimensional kernels or filters to scan the input image, generating a feature map that distills the essential information. This process reduces the spatial dimensions of the data while preserving critical information present in the input image. The network then uses a pooling layer to further down-sample the feature maps by keeping only the most relevant information. In a typical CNN architecture, multiple convolutional layers and pooling layers are stacked sequentially, allowing the network to learn increasingly complex and abstract feature representations of the input data. The output is then flattened and subsequently fed into a fully connected neural network for the final classification task.

6.2.1 Pre-processing of the images

The p_T, η, ϕ of the constituents of each jet are mapped into a two-dimensional image where each pixel coordinate (x, y) represents a particle's (η, ϕ) , and the pixel intensity is the p_T of the particle. Before mapping, the jet constituents are subject to some pre-processing steps [36]. First, the jet is centered at the p_T weighted centroid of the constituents. Then, the constituents are rotated in such a way that the principal axis lies in the vertical direction (along the Y-axis). Lastly, the constituents are reflected on both axes such that the hardest constituents (constituents with the highest p_T) lie in the third quadrant. The intensity of the whole image is normalised to 1.

Figure 16 shows the averaged jet images for QCD jets, top jets, and W jets after pre-processing. As the jet constituents were reclustered into a p_T dependent radius, the dimensions of the images are also dependent on p_T . As we go from lower to higher momenta, the three-prong and two-prong features of the core of the top jets and W jets, respectively, shrink and look similar to the QCD jets. The W jets are harder to distinguish from the QCD jets because their two-prong structure appears more similar to that of the QCD jets when highly collimated. However, using the same reclustering radius for all three types of jets leads to some noticeable differences at higher p_T , as the constituents of W jets become less spread out compared to those of QCD and top jets for the same image size.

6.2.2 The network architecture and results

We built the CNN model on two 80 GB NVIDIA A100 GPUs using the TensorFlow-Keras framework. Figure 17 shows the layer structure in our model. Filters of shape 2×2 were used

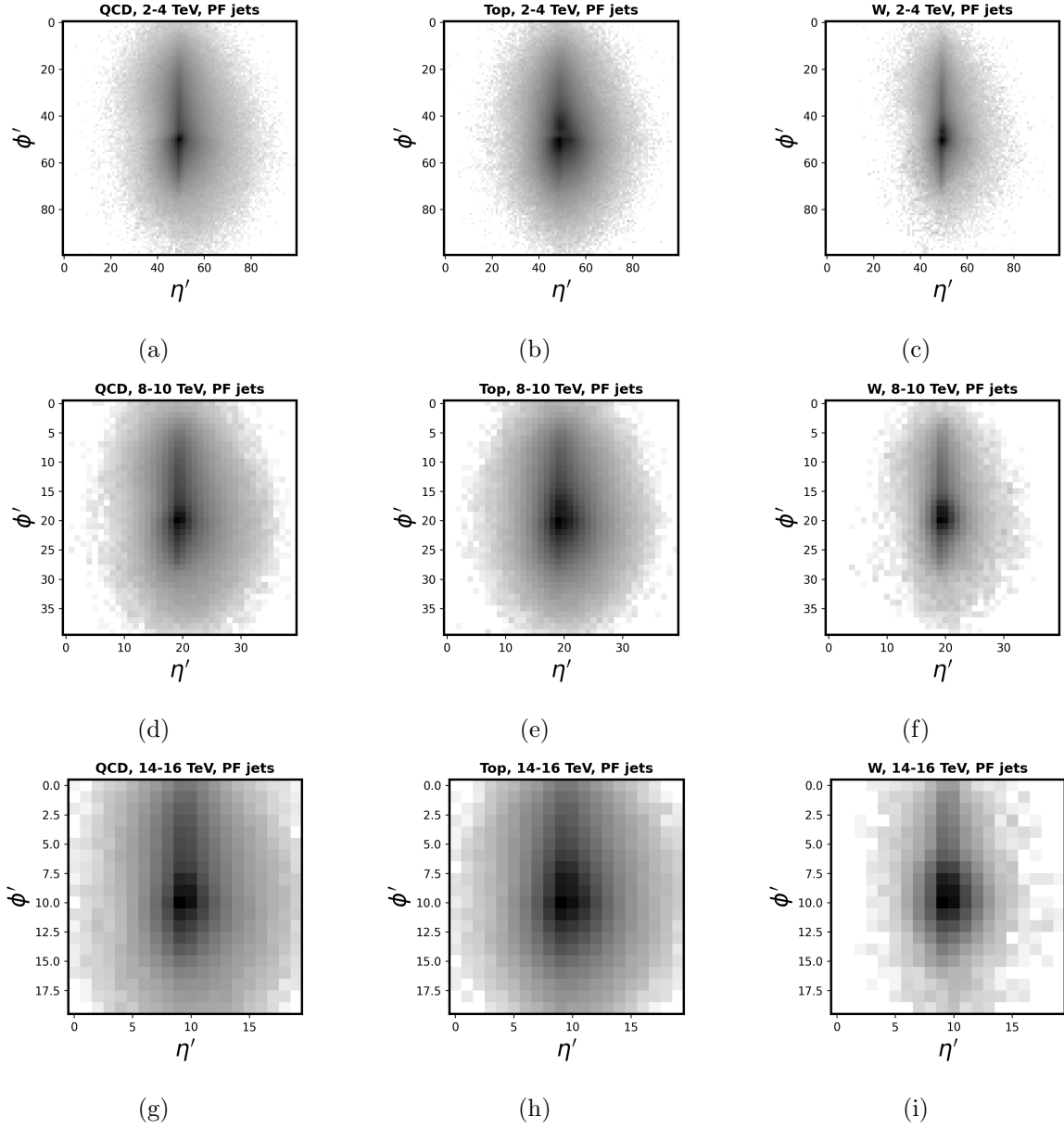


Figure 16: Jet images after averaging over 100,000 events of (a) 2-4 TeV QCD jets, (b) 2-4 TeV top jets, (c) 2-4 TeV W jets, (d) 8-10 TeV QCD jets, (e) 8-10 TeV top jets, (f) 8-10 TeV W jets, (g) 14-16 TeV QCD jets, (h) 14-16 TeV top jets, and (i) 14-16 TeV W jets.

for every convolution and pooling operation. To regularise the network and reduce overfitting, a dropout of 0.2 was added after the second Max-Pooling Layer, and a dropout of 0.5 was used before the two-dimensional feature maps were flattened. We have also added early-stopping with patience of 5 epochs. The output, in this case, is categorised into three classes, with a

probability of a jet being ‘QCD-like’ (0), ‘top-like’ (1), or ‘W-like’ (2).

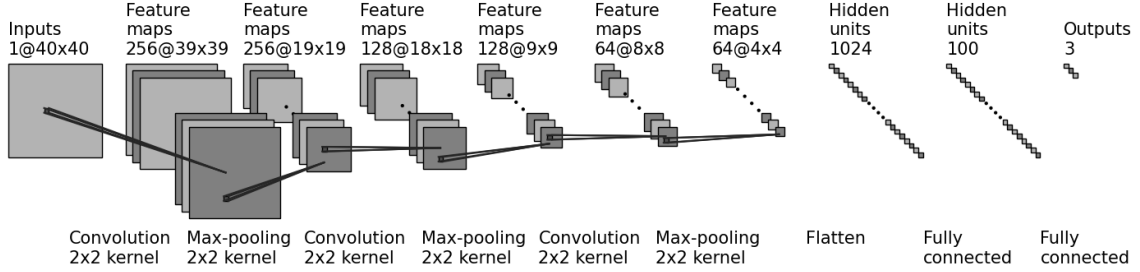


Figure 17: Symbolic representation of the model architecture of CNN used in our analysis. This figure is generated by adapting the code from https://github.com/gwding/draw_convnet.

With this network, we train the models on $\eta - \phi$ images of particle-flow jets separately for each p_T range. The results for the multi-class classification using CNN are represented by the ROC and AUC in Figure 18. Figure 18a shows the ROC for the identification of the top jets, while Figure 18b shows the ROC for the identification of the W jets. The CNN model identifies top jets better than W jets, as indicated by the respective AUC metrics.

Using the same CNN model for 2–4 TeV jets, we trained and tested on jets generated at $\sqrt{s} = 14$ TeV. We observe a 5% degradation in the top and W classification performance when moving from $\sqrt{s} = 14$ TeV to $\sqrt{s} = 100$ TeV. We had previously observed a 1-3% degradation with XGBoost. This indicates that ML taggers face increased challenges in the high-energy FCC-hh environment. CNN, which is a jet-constituent-based tagger, performs worse than XGBoost, which is a jet-observable-based tagger. The observations in this study call for further investigation in future developments of robust and more complex machine learning taggers. For example, Ref. [188] lists the performance of various state-of-the-art taggers, with the ParticleNet [38] achieving an AUC of 0.961. At the LHC, for jets above 2 TeV and signal efficiency (ϵ_S) of 0.8, ParticleNet reaches a background efficiency (ϵ_B) of $\sim 4\%$, and $\sim 0.5\%$ for $\epsilon_S = 0.5$. A detailed evaluation of such taggers in the FCC-hh environment remains an important direction for future work.

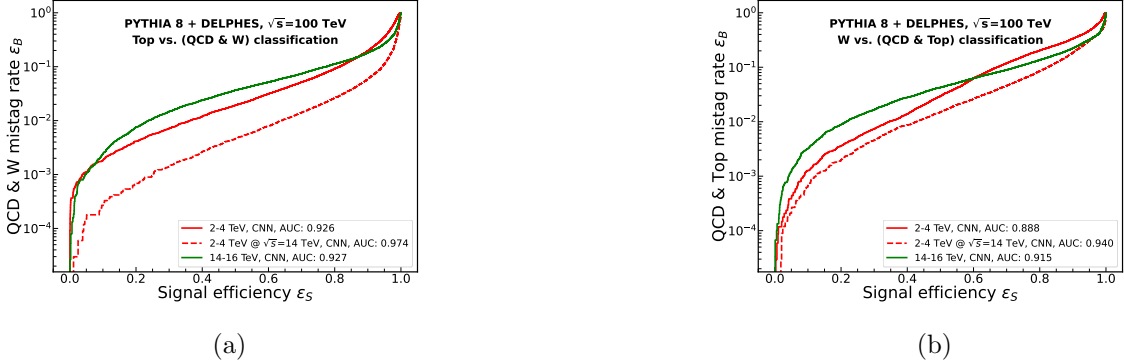


Figure 18: Receiver-Operating-Characteristic (ROC) curve and the Area-Under-the Curve (AUC) for multi-class classification. Figure 18a shows the ROC for top vs. QCD and W classification for 2–4 TeV and 14–16 TeV jets. Figure 18b shows the ROC for W vs. QCD and top classification for 2–4 TeV and 14–16 TeV jets. The red dotted lines in the Figures 18a and 18b show the ROC of a multi-class CNN for top vs. background and W vs. background classification, respectively.

p_T	CNN results		XGBoost results	
	$\epsilon_S^{top} = \epsilon_S^W = 30\%$			
	ϵ_B^{top}	ϵ_B^W	ϵ_B^{top}	ϵ_B^W
2–4 TeV	.71%	.73%	.24%	.16%
14–16 TeV	1.5%	1.6%	.68%	.02%
	$\epsilon_S^{top} = \epsilon_S^W = 40\%$			
2–4 TeV	1.2%	1.4%	.48%	.31%
14–16 TeV	2.4%	2.77%	1.2%	.06%
	$\epsilon_S^{top} = \epsilon_S^W = 60\%$			
2–4 TeV	3.1%	6.2%	1.8%	1.8%
14–16 TeV	5.2%	6.3%	3.4%	.31%

Table 3: Background efficiencies of CNN and XGBoost models for fixed signal efficiencies ($\epsilon_S^{top/W}$) of 30%, 40%, and 60%. The mistagging efficiencies for top identification are indicated as ϵ_B^{top} , while the mistagging efficiencies for W identification are indicated as ϵ_B^W .

We also summarise the results for the best-performing XGBoost tagger (trained with Obs_{strk} , $Obs_{rec.}$, and Obs_{SD}) and the CNN tagger in Table 3. The feature-based XGBoost tagger outperforms the image-based CNN tagger. Notably, the W jet identification by XGBoost at high p_T is superior to CNN. At 2–4 TeV, a 60% top tagging efficiency corresponds to

a background (including QCD and W) mistagging rate of $\sim 3\%$. The same tagging efficiency for W jets yields a background (QCD and top) mistagging rate of $\sim 6\%$. At 14–16 TeV, a 60% W tagging efficiency results in mistagging rates of $\sim 4\%$ for top jets and 6% for W jets. When the W tagging efficiency exceeds 60%, the background rejection improves for 14–16 TeV jets compared to 2–4 TeV jets. In our analysis of BSM signatures, we fix the working points of the taggers to obtain 60% top tagging and 60% W tagging efficiency.

In this study, the CNN was trained on jet images with the resolution of ECAL. Using track-based images could be a possible way to improve CNN’s performance. Track-based jet images offer higher resolution because the tracking detector’s granularity (0.001 in η - ϕ space) is much finer compared to the calorimeter’s (0.01). However, to maintain the same jet size, the image dimensions increase by a factor of 10, leading to significant computational challenges when used to train the convolutional neural networks (CNNs). Due to hardware limitations, we opted to use calorimeter-based jet images with a more manageable size. A possible future direction would be to explore convolutional neural networks on track-based images and to further optimize the networks.

In the following section, we will apply the developed taggers to explore physics beyond the Standard Model. As previously noted, the example analyses presented herein serve as illustrations, and the analysis strategy can be further optimized to enhance sensitivity. Our primary objective was to provide a foundation for future investigations rather than achieving the most stringent limits.

7 Analysis of BSM processes with top and W jets in the final state

This section explores the three BSM benchmarks described earlier (Section 2). We begin with the analysis of a neutral gauge boson Z' that decays to two top quarks, then proceed to study the production of a heavy neutral Higgs boson in the W^+W^- decay channel. Lastly, we discuss the associated production of a B' VLQ with a light jet, where the B' decays to a top quark and a W boson.

For our analysis, we choose the working point corresponding to a signal efficiency $\epsilon_S = 60\%$. The XGBoost taggers outperform the CNN taggers; however, for completeness, we also present the results using the CNN tagger. Finally, we combine both taggers to enhance signal purity and achieve high background rejection. In each of the three analyses, we select the two highest p_T jets in each event. If both jets are tagged, we proceed to calculate the invariant mass of the two. The resonance peaks are shifted to lower mass values. This effect is expected and can be corrected by applying jet energy correction factors, which are not used in this study. Instead, we factor in the effect of mass peak shift and use this information to apply

proper mass cuts for each benchmark accordingly. We select two tagged jets and require the invariant mass to fall within 10-20% of the mass of the resonant particle. The analyses are summarised in Table 4.

Analysis-I	$p_T^{j_1/j_2} > 2 \text{ TeV}, \eta < 2.5$ j_1 AND j_2 are XGBoost top/W-tagged $m_{res.} - \Delta_1 < m_{j_1 j_2} < m_{res.} + \Delta_2$
Analysis-II	$p_T^{j_1/j_2} > 2 \text{ TeV}, \eta < 2.5$ j_1 AND j_2 are CNN top/W-tagged $m_{res.} - \Delta_1 < m_{j_1 j_2} < m_{res.} + \Delta_2$
Analysis-III	$p_T^{j_1/j_2} > 2 \text{ TeV}, \eta < 2.5$ j_1 AND j_2 are XGBoost AND CNN top/W-tagged $m_{res.} - \Delta_1 < m_{j_1 j_2} < m_{res.} + \Delta_2$

Table 4: Three analyses used for all the benchmark scenarios with XGBoost tagger (I), CNN tagger (II), and both taggers (III).

We summarise the analysis strategy as follows for *all* three benchmarks:

- Preselect events by requiring the two hardest jets to satisfy $p_T > 2 \text{ TeV}$ and $|\eta| < 2.5$.
- Recluster the jets with a dynamic radius $R(p_T)$, followed by grooming using softdrop algorithm. Additionally, form track-only jet collections.
- Compute the variables of Set 1 (Section 6.1) with FASTJET and form jet-images per Section 6.2.1.
- Jet tagging is performed using XGBoost and CNN taggers corresponding to the correct p_T range, selected based on the individual jet's p_T . For example, in an event where a Z' boson produces two jets with p_T values of 6.5 TeV and 3 TeV, the 6–8 TeV ML tagger is used for the first jet, while the 2–4 TeV ML tagger is applied to the second jet. Each tagger returns a probability score, which is then used to classify the jet as a top or a W jet.
- Form the invariant mass of the two leading tagged jets and apply a resonance-dependent mass window (10–20% around the resonance mass).
- Evaluate background yields (B) and signal efficiency (ϵ_S), then extract 95% CL upper limits (σ_{UL}) from the following significance formula [189]:

$$\eta_S = \sqrt{2(S+B) \ln \left(\frac{(S+B)(B+\sigma_b^2)}{B^2+(S+B)\sigma_b^2} \right) - \frac{B^2}{\sigma_b^2} \ln \left(1 + \frac{\sigma_b^2 S}{B(B+\sigma_b^2)} \right)} \quad (7.1)$$

In this study, we obtain the projected upper limits at $\eta_S = 2$, representing a 95% confidence interval. σ_b is the systematic uncertainty times the background yield.

Systematic uncertainties originate from uncertainties on the parton distribution function (PDF), uncertainties on the production cross-section, scale uncertainties in the matrix element and parton shower algorithms, uncertainty on the integrated luminosity, and uncertainties on the object identification efficiencies [190]. We compute upper limits at 95% CL on the product of cross-section and branching ratio assuming an overall 5% systematic uncertainty ($\sigma_b = 5\% \times B$).

7.1 Analysis of Z' boson decaying to boosted top jets

With the models trained to efficiently distinguish between boosted top jets, QCD jets, and W jets, we proceed with the reconstruction of the BSM gauge boson, Z' . We have considered the decay $Z' \rightarrow t\bar{t}$ for four different benchmark masses of the Z' boson: $m_{Z'} = 5$ TeV, 10 TeV, 15 TeV, and 20 TeV. As the SM backgrounds to the $Z' \rightarrow t\bar{t}$ process, in addition to QCD dijet and $t\bar{t}$, we have also considered SM production of W^+W^- , $W^\pm Z$, and ZZ , collectively denoted as VV , SM production of $W^\pm + \text{jet}$, and $Z + \text{jet}$, collectively denoted as Vj , and the SM tW process.

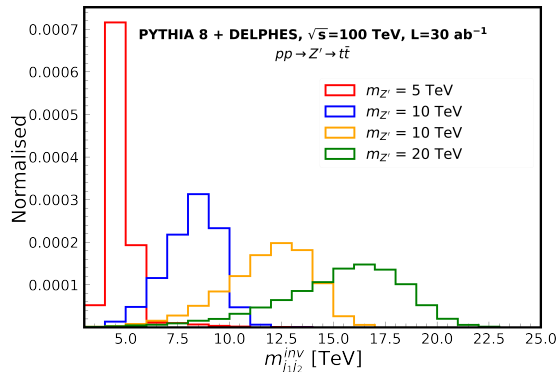


Figure 19: Normalised invariant mass distribution of two hardest jets from $pp \rightarrow Z' \rightarrow t\bar{t}$ process.

Figure 19 shows the invariant mass distribution of the two jets coming from the signal process. From the width of the distributions, we set Δ_1 as 20% of $m'_{Z'}$, and Δ_2 as 10% of $m'_{Z'}$. Table 5 shows the background yield (B) and signal efficiency (ϵ_S) for the four benchmarks of the Z' boson at different levels of cuts when the XGBoost tagger is used.

As reported in table 5, after applying the cut on P_{top}^{XGB} for j_1 and j_2 , the QCD background reduces to 0.08% of its original value. The tW reduces to 0.4% of its original value. However,

Selection cuts	Background yield				ϵ_S
	jj	$t\bar{t}$	tW	$VV + Vj$	$Z' \rightarrow t\bar{t}$
$m_{Z'} = 5 \text{ TeV}$					
$p_T^{j_1/j_2} > 2 \text{ TeV}, \eta < 2.5$	4.0×10^9	8.5×10^6	1.1×10^6	2.2×10^7	18%
j_1, j_2 are XGBoost top-tagged	3.0×10^6	3.2×10^6	4508	717	7%
$4.0 \text{ TeV} < m_{j_1 j_2} < 5.5 \text{ TeV}$	1.7×10^6	1.6×10^6	2460	8	6%
$m_{Z'} = 10 \text{ TeV}$					
$p_T^{j_1/j_2} > 2 \text{ TeV}, \eta < 2.5$	4.0×10^9	8.5×10^6	1.1×10^6	2.2×10^7	70%
j_1, j_2 are XGBoost top-tagged	3.0×10^6	3.2×10^6	4508	717	24%
$8.0 \text{ TeV} < m_{j_1 j_2} < 11.0 \text{ TeV}$	5.3×10^5	2.5×10^5	656	19	16%
$m_{Z'} = 15 \text{ TeV}$					
$p_T^{j_1/j_2} > 2 \text{ TeV}, \eta < 2.5$	4.0×10^9	8.5×10^6	1.1×10^6	2.2×10^7	82%
j_1, j_2 are XGBoost top-tagged	3.0×10^6	3.2×10^6	4508	717	27%
$12.0 \text{ TeV} < m_{j_1 j_2} < 16.5 \text{ TeV}$	4.4×10^4	3.0×10^4	22	94	17%
$m_{Z'} = 20 \text{ TeV}$					
$p_T^{j_1/j_2} > 2 \text{ TeV}, \eta < 2.5$	4.0×10^9	8.5×10^6	1.1×10^6	2.2×10^7	86%
j_1, j_2 are XGBoost top-tagged	3.0×10^6	3.2×10^6	4508	717	29%
$16.0 \text{ TeV} < m_{j_1 j_2} < 22.0 \text{ TeV}$	6530	5221	10	3	15%

Table 5: Background yield and signal efficiency (ϵ_S) for the four benchmark mass-points of Z' boson. The $m_{j_1 j_2}$ cuts are different for different values of Z' boson mass. Here, V denotes W^\pm , and Z .

due to the large cross-section of QCD, it still remains comparable to the $t\bar{t}$ background. The background yields from diboson (VV) and boson-plus-jet (Vj) processes have been combined. They are not dominant background sources; however, the Vj cross-section is higher than the $t\bar{t}$ cross-section, resulting in the high background yield initially. After applying all the selection cuts, these backgrounds are reduced to negligible levels. For $m_{Z'} = 5 \text{ TeV}$, the signal efficiency is very low due to the jets failing the $p_T > 2 \text{ TeV}$ criterion. Heavier Z' bosons decay into harder jets, hence we see an increase in the signal efficiency with mass. Both signal efficiency and background yield drop after using the cut on the invariant mass. The drop is more for higher resonant masses as the distribution becomes wider.

Table 6 shows the projected 95% CL upper limits on the cross-section for the process $pp \rightarrow Z' \rightarrow t\bar{t}$ at the FCC-hh for three different analysis strategies (I, II, III). We also quote the results with 5% systematic uncertainty on the background in Table 6. Among the three strategies, Analysis III consistently provides the best or comparable sensitivity due to improved background suppression. The most stringent limit is obtained for $m_{Z'} = 20 \text{ TeV}$, where the cross-section times branching can be constrained down to 0.099 fb at 95% CL. The CNN taggers did not perform well in comparison to the XGBoost taggers previously, resulting

$m_{Z'}$	Analysis	Background yield at 30 ab ⁻¹				Signal	$\sigma(pp \rightarrow Z' \rightarrow t\bar{t})_{UL}$ at 95% CL [fb] (5% sys.)
		jj	$t\bar{t}$	tW	$VV + Vj$	Efficiency	
5	I	1.7×10^6	1.6×10^6	2460	8	0.063	4.3 (395)
	II	3.2×10^6	1.4×10^6	7057	6016	0.053	6.0 (665)
	III	1.6×10^5	9.6×10^5	989	8	0.04	4.2 (229)
10	I	5.3×10^5	2.5×10^5	656	19	0.16	0.82 (37)
	II	1.1×10^6	2.6×10^5	1208	103	0.18	0.95 (57)
	III	4.4×10^5	1.8×10^5	310	0.6	0.12	0.95 (39)
15	I	44161	30299	22	94	0.17	0.24 (3.4)
	II	88637	32083	139	138	0.18	0.28 (5.1)
	III	22557	21016	9	83	0.12	0.26 (2.8)
20	I	6530	5221	10	3	0.16	0.099 (0.56)
	II	22041	5264	32	7	0.17	0.14 (1.24)
	III	2083	3318	9	0.3	0.11	0.099 (0.39)

Table 6: Table showing the number of events obtained for background processes, the signal efficiency after applying all cuts, and the upper limit of $pp \rightarrow Z' \rightarrow t\bar{t}$ cross-section at 95% CL for the three different analyses listed on Table 4. Here, V denotes W^\pm , Z . The limits at 95% CL with 5% systematic uncertainty on the background are listed within parentheses.

in weaker constraints. A CMS study in Ref. [191] conducted $t\bar{t}$ resonance search and placed upper limits at 95% CL on the cross-section times branching of a $\Gamma/m = 10\%$ Z' boson of mass 5 TeV to be 9.7 fb.

For $m_{Z'} = 5$ TeV, the 5% systematic uncertainty worsens the limit by a factor of approximately 100. The backgrounds in the low-mass region are large, and thus, the sensitivity in this region is limited by systematics. Choosing a stricter point on the ROC could potentially reduce the QCD background at the cost of a lower signal efficiency; however, the SM $t\bar{t}$ background remains irreducible. The impact of systematics decreases with increasing resonance mass, as we move from a low- x to a high- x region in FCC-hh (x is the momentum fraction), where background cross-sections fall steeply.

7.1.1 Effect of b tagging

Before we proceed to the next analysis of the heavy Higgs boson, we would like to briefly mention the effect of b tagging. The top jets contain a b jet as one of the three subjects. We have conducted our analysis without employing any b tagging. In the case of top tagging, if the two jets in an event obtained after applying selection cuts were also required to be b tagged, it would reduce the QCD background further. For FCC-hh, the b tagging efficiency employed in DELPHES follows the functional form $0.82 * (1 - p_T/15 \text{ TeV})$ [89] for the jets in our

selected phase space ($|\eta| < 2.5$). Table 7 shows the effect of using b tagging as an additional criterion at the selection level.

Effect of b tagging on background events, with b tagging efficiency = $0.82 * (1.0 - p_T/15 \text{ TeV})$		
Selection cuts	$pp \rightarrow jj$	$pp \rightarrow t\bar{t}$
$p_T^{j_1/j_2} > 2 \text{ TeV}, \eta < 2.5$	4.0×10^9	8.5×10^6
$p_T^{j_1/j_2} > 2 \text{ TeV}, \eta < 2.5, \text{btag}(j_1/j_2) = 1$	3.7×10^7	2.5×10^6

Table 7: Effect of b tagging on the two hardest jets at the selection level for QCD and $t\bar{t}$ backgrounds.

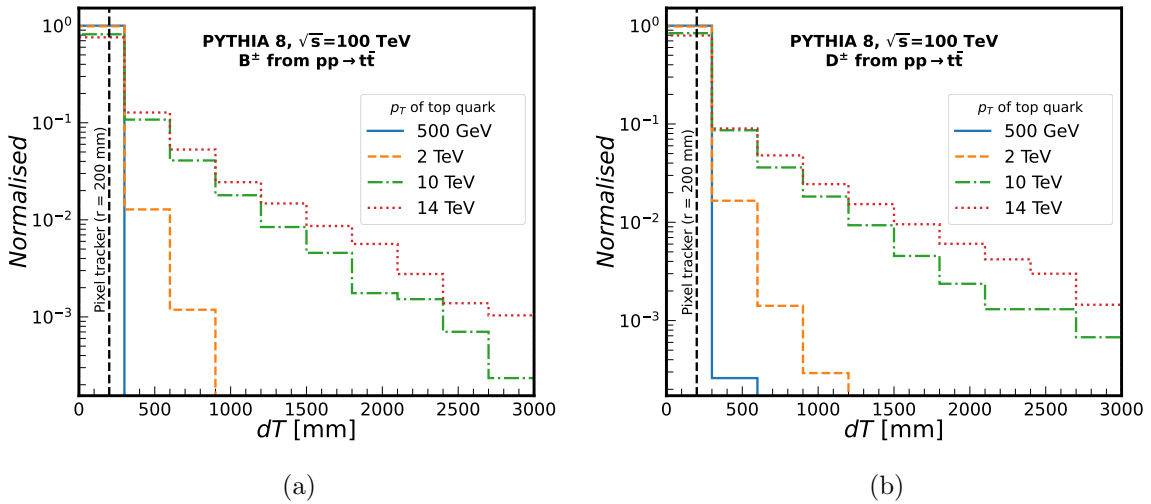


Figure 20: Normalised distribution of displacement (dT) of (a) boosted B^\pm hadron and (b) boosted D^\pm hadron from the decay of 500 GeV, 2 TeV, 10 TeV, and 14 TeV top quark. The dashed line in black represents the dimension of the inner tracking layer of the FCC-hh detector.

The QCD background efficiency reduces to 0.95% of its original value with the use of the b tagging criterion. Since QCD and $t\bar{t}$ are the leading backgrounds, a simple calculation using b tagging shows that the 95% CL upper limits on $\sigma(pp \rightarrow Z' \rightarrow t\bar{t})$ with 5% systematic uncertainty reduce to $\sim 60 \text{ fb}$ using Analysis III. However, the question remains how the b tagging performance in the actual FCC-hh experiment will be affected in the case of multi-TeV jets. A study in [192] demonstrated that in the multi-TeV regime, the reconstruction of highly boosted B -hadrons becomes challenging owing to their high displacement and high collimation of decay products. In Figure 20, we have shown the displacement of the B^\pm and D^\pm in the radial direction (dT), with increasing p_T of the top jet. The line in black shows

the dimension of the inner tracking layer, which consists of pixel sensors of $25\text{--}33.3\ \mu\text{m} \times 50\text{--}400\ \mu\text{m}$ and extends in the radial direction up to 200 mm [20].

Boosted hadrons coming from a 500 GeV top are well contained within the inner tracking layer. In contrast, for top quarks with $p_T = 2\ \text{TeV}$, 10 TeV, and 14 TeV, approximately 4%, 26%, and 32% of B^\pm decay outside the pixel tracker. A hit multiplicity approach to b tagging was proposed in Ref. [193] to tackle this challenge for boosted b jets. Using the information from the number of hits in each detector layer improved the b tagging in multi-TeV jets. Further studies could explore the effectiveness of this technique in improving b tagging for high- p_T top jets.

7.2 Analysis of neutral heavy Higgs boson decaying to boosted W jets

We consider the production of a heavy Higgs boson that decays to the SM W bosons: $pp \rightarrow H \rightarrow W^+W^-$. We consider the hadronic decay mode of the two W bosons. The final state thus consists of two highly boosted W jets. We consider four different masses of the heavy neutral Higgs to be 5 TeV, 10 TeV, 15 TeV, and 20 TeV. Depending on the mass, the W jets will carry a few TeV of energy. The SM background consists of QCD dijet production and the SM production of W^+W^- . We have considered other backgrounds, such as SM production of $W^\pm/Z + \text{jet}$, WZ , and ZZ . Additionally, top jets, which can be misidentified as W jets, are included as part of the background for the $H \rightarrow WW$ in the $t\bar{t}$ and tW processes.

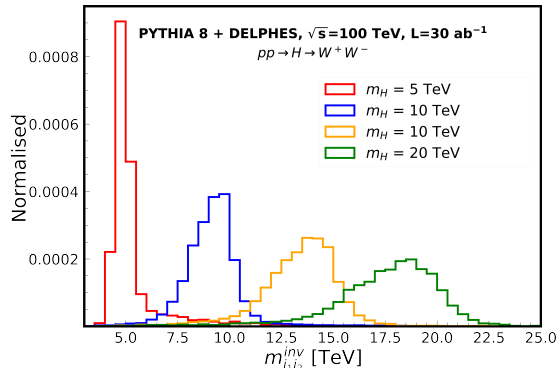


Figure 21: Normalised invariant mass distribution of two hardest jets from $pp \rightarrow H \rightarrow W^+W^-$ process.

Similar to the Z' analysis, we employ multi-class classification using XGBoost and CNN taggers. For each event, we require the presence of two W -tagged jets. Using this criterion and the analyses listed in Table 4, we calculate the signal and background efficiencies. The cuts on the invariant mass of the two jets tagged as W are specific to the signal benchmark.

Selection cuts	Background yield				ϵ_S
	VV	jj	Vj	$tW + t\bar{t}$	$H \rightarrow W^+W^-$
$m_H = 5 \text{ TeV}$					
$p_T^{j_1/j_2} > 2 \text{ TeV}, \eta < 2.5$	4.2×10^5	4.0×10^9	2.2×10^7	9.6×10^6	32%
j_1, j_2 are XGBoost W-tagged	1.6×10^5	2.7×10^6	6.5×10^5	8211	17%
$4.0 \text{ TeV} < m_{j_1 j_2} < 5.5 \text{ TeV}$	46444	1.3×10^6	3.4×10^5	4151	16%
$m_H = 10 \text{ TeV}$					
$p_T^{j_1/j_2} > 2 \text{ TeV}, \eta < 2.5$	4.2×10^5	8.5×10^6	1.1×10^6	2.2×10^7	74%
j_1, j_2 are XGBoost W-tagged	1.6×10^5	2.7×10^6	6.5×10^5	8211	42%
$8.0 \text{ TeV} < m_{j_1 j_2} < 11.0 \text{ TeV}$	27810	5.8×10^5	46694	460	36%
$m_H = 15 \text{ TeV}$					
$p_T^{j_1/j_2} > 2 \text{ TeV}, \eta < 2.5$	4.2×10^5	8.5×10^6	1.1×10^6	2.2×10^7	80%
j_1, j_2 are XGBoost W-tagged	1.6×10^5	2.7×10^6	6.5×10^5	8211	41%
$12.0 \text{ TeV} < m_{j_1 j_2} < 16.5 \text{ TeV}$	9020	77324	4020	154	35%
$m_H = 20 \text{ TeV}$					
$p_T^{j_1/j_2} > 2 \text{ TeV}, \eta < 2.5$	4.2×10^5	8.5×10^6	1.1×10^6	2.2×10^7	82%
j_1, j_2 are XGBoost W-tagged	1.6×10^5	2.7×10^6	6.5×10^5	8211	38%
$16.0 \text{ TeV} < m_{j_1 j_2} < 22.0 \text{ TeV}$	3408	1218	477	31	31%

Table 8: Background yield and signal efficiency (ϵ_S) for the four benchmark mass-points of H boson. The $m_{j_1 j_2}$ cuts are different for different values of H boson mass. Here, V denotes W^\pm , and Z .

The distribution of jet invariant mass for each signal benchmark is shown in Figure 21. We use $\Delta_1 = 20\%$ of m_H and $\Delta_2 = 10\%$ of m_H . Table 8 summarises the results for all benchmarks using Analysis I.

The dominant background is QCD due to its large cross-section. The SM $W/Z + j$ background is the next most dominant contribution. Since the SM WW final state is identical to that of the signal, we evaluate the fractional contributions from its different p_T bins to the background in the $H \rightarrow WW$ analysis. The $t\bar{t}$ and tW backgrounds are greatly reduced by the multi-class taggers. Using these numbers, we calculate the upper limit on the cross-section. Table 9 summarises the background yields and signal efficiency after all cuts, and the upper limit on the cross-section for the process $pp \rightarrow H \rightarrow W^+W^-$ at 95% CL, for heavy Higgs boson masses of 5 TeV, 10 TeV, 15 TeV, and 20 TeV. The upper limits, considering systematic uncertainty of 5%, are shown in parentheses.

The strongest upper bounds on $\sigma(pp \rightarrow H \rightarrow W^+W^-)$ at 95% CL are obtained with Analysis-III. At $m_H = 5 \text{ TeV}$, Analysis-III constrains $\sigma(pp \rightarrow H \rightarrow W^+W^-)$ at 95% CL up to 0.69 fb (16 fb with 5% systematics). As the Higgs mass increases, the limits tighten

m_H	Analysis	Background yield at 30 ab ⁻¹				Signal Efficiency	$\sigma(pp \rightarrow H \rightarrow W^+W^-)_{UL}$ at 95% CL [fb] (5% sys.)
		VV	jj	Vj	$tW + t\bar{t}$		
5	I	46444	1.3×10^6	3.4×10^5	4152	0.16	1.15 (78)
	II	30385	4.5×10^6	6.1×10^5	4949	0.11	3.0 (355)
	III	23827	72450	99008	1535	0.095	0.69 (16)
10	I	27810	5.8×10^5	46694	460	0.36	0.32 (13)
	II	28505	2.6×10^6	1.4×10^5	2723	0.36	0.69 (60)
	III	21460	32151	27138	222	0.29	0.14 (2.2)
15	I	9020	77324	4019	154	0.35	0.12 (1.95)
	II	9550	9.8×10^5	13894	368	0.39	0.37 (19)
	III	6881	52693	1766	94	0.28	0.13 (1.65)
20	I	3407	1218	477	31	0.31	0.034 (0.128)
	II	3579	4.8×10^5	2825	111	0.35	0.29 (11)
	III	2380	1218	380	30	0.23	0.041 (0.141)

Table 9: Table showing the number of events obtained for background processes, the signal efficiency after applying all cuts, and the upper limit of $pp \rightarrow H \rightarrow W^+W^-$ cross-section at 95% CL for the three different analyses listed on Table 4. Here, V denotes W^\pm, Z . The limits at 95% CL with 5% systematic uncertainty on the background are listed within parentheses.

further, reaching as low as 0.034 fb (0.128 fb) in Analysis I, and 0.041 fb (0.141 fb) in Analysis III, respectively, for $m_H = 20$ TeV.

7.3 Analysis of vector-like, heavy B' quark decaying to boosted top jet and W jet

In this subsection, we study the production of a vector-like quark in association with a jet via the process $pp \rightarrow B'j$, and $B' \rightarrow tW$, for $m_{B'} = 5$ TeV and 10 TeV, where both the top quark and the W boson decay hadronically.

The signal topology consists of a top jet and a W jet. The SM background consists of the $pp \rightarrow tW$, $pp \rightarrow jj$, $pp \rightarrow t\bar{t}$, $pp \rightarrow VV$, and $pp \rightarrow Vj$ processes, where V represents W^\pm/Z . We select the two hardest jets with $p_T > 2$ TeV and $|\eta| < 2.5$ jets and use the ML taggers to classify them. Following the procedure highlighted in the previous sections, we demand that either one of the two jets should be identified as the top jet and the other one should be identified as the W jet with $\epsilon_{t/W} = 60\%$.

Table 10 presents the upper limits on the cross-section for the process $pp \rightarrow jB' \rightarrow jtW$ at 95% CL for $m_{B'} = 5$ TeV and $m_{B'} = 10$ TeV. The values are computed for Analyses I, II, and III. We apply an invariant mass cut on the signal benchmarks: $4.5 \text{ TeV} < m_{j_1j_2} < 5.5 \text{ TeV}$, and $9 \text{ TeV} < m_{j_1j_2} < 11 \text{ TeV}$ for $m_{B'} = 5$ TeV and 10 TeV, respectively. For

$m_{B'}$	Analysis	Background yield at 30 ab ⁻¹				ϵ_S	σ_{UL} at 95% CL [fb] (5% sys.)
		tW	jj	Vj	$VV + t\bar{t}$		
5	I	8.1×10^5	3.5×10^6	6.6×10^5	1.8×10^5	0.086	4.0 (459)
	II	6.3×10^5	7.3×10^6	5.0×10^5	1.3×10^5	0.070	6.1 (921)
	III	4.9×10^5	3.6×10^5	2.3×10^5	81363	0.055	3.0 (162)
10	I	51989	1.6×10^6	66347	10370	0.084	2.3 (155)
	II	51692	3.7×10^6	79516	17366	0.090	3.2 (303)
	III	38729	2.2×10^5	33449	963	0.064	1.2 (36)

Table 10: Table showing the number of events obtained for background processes, the signal efficiency (ϵ_S) for $pp \rightarrow jB' \rightarrow jtW$ after all cuts, and the upper limit of $pp \rightarrow jB' \rightarrow jtW$ cross-section (σ_{UL}) at 95% CL, for the three different analyses listed on Table 4. Here, V denotes W^\pm , Z . The limits at 95% CL with 5% systematic uncertainty on the background are listed within parentheses.

$m_{B'} = 5$ TeV, Analysis III yields $\sigma_{UL} = 3.0$ fb, compared to 4.0 fb and 6.1 fb for Analyses I and II, respectively. For $m_{B'} = 10$ TeV, the upper limits improve due to lower backgrounds, with Analysis III achieving $\sigma_{UL} = 1.2$ fb, outperforming Analysis I (2.3 fb) and II (3.2 fb).

Effect of width

Before we summarise our work, we would like to discuss the effect of the width of the BSM particles on our results. At the 100 TeV collider, particles with masses in the tens of TeV range are expected to have very large widths. This large width makes it difficult to accurately reconstruct the mass of these particles because their decay products are spread over a wider range, leading to less distinct mass peaks. The decay width (Γ) increases with the mass of the particle, causing the resonance to become broader. So far, we have been using full-width calculations for the signal vs background analysis of a vector-like B' quark [194].

To demonstrate the effect of width, we show the distributions of $m_{j_1 j_2}^{\text{inv}}$ of the signal with the full-width (Γ), half-width ($\Gamma/2$), and quarter-width ($\Gamma/4$) in Figure 22. The distribution peaks more accurately at lower widths. We use the reduced width to obtain signal efficiency and upper limits on cross-section. The results are listed in Table 11. The background yields remain the same.

At smaller widths, such as half ($\Gamma/2$) or one-fourth ($\Gamma/4$) of the full width, we obtain better results. This is because reducing the width helps reduce the overlap of the signal with the background and the spread in the particle's mass, making it easier to identify and reconstruct the mass of heavy particles. We adapt the invariant mass selection for each width scenario to improve sensitivity to lower widths from increased signal efficiency and lower

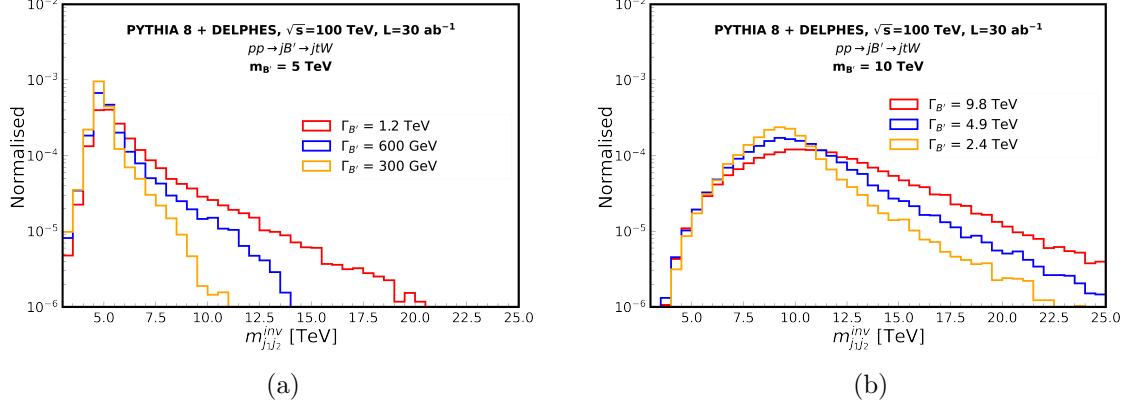


Figure 22: Normalised invariant mass distribution of two hardest jets from $pp \rightarrow jB' \rightarrow jtW$ process for 5 TeV (left) and 10 TeV (right) B' quark when the width is varied from Γ to $\Gamma/4$.

Γ'_B [TeV]	Cut on $m_{j_1j_2}$ [TeV]	Background yield at 30 ab^{-1}				ϵ_S	σ_{UL} at 95% CL [fb] (5% sys.)
		tW	jj	Vj	$VV + t\bar{t}$		
$m_{B'} = 5 \text{ TeV}$							
1.2	$4.5 < m_{j_1j_2} < 5.5$	4.9×10^5	3.6×10^5	2.3×10^5	81363	0.055	3.0 (162)
0.6	$4.6 < m_{j_1j_2} < 5.4$	4.0×10^5	3.6×10^5	1.8×10^5	72086	0.058	2.5 (128)
0.3	$4.6 < m_{j_1j_2} < 5.4$	4.0×10^5	3.6×10^5	1.8×10^5	72086	0.066	2.2 (113)
$m_{B'} = 10 \text{ TeV}$							
9.8	$9.0 < m_{j_1j_2} < 11.0$	38729	2.2×10^5	33449	5140	0.064	1.2 (36)
4.9	$9.2 < m_{j_1j_2} < 10.8$	28358	1.6×10^5	23663	3927	0.073	0.93 (22)
2.4	$9.0 < m_{j_1j_2} < 10.5$	32477	1.9×10^5	27813	4330	0.086	0.86 (22)

Table 11: Comparison of signal efficiency, and $\sigma(pp \rightarrow jB' \rightarrow jtW)_{UL}$ at 95% CL for $m_{B'} = 5 \text{ TeV}$ and $m_{B'} = 10 \text{ TeV}$ with $\Gamma' = \Gamma$, $\Gamma' = \Gamma/2$ and $\Gamma' = \Gamma/4$ with Analysis III.

background yields.

8 Conclusion

The FCC-hh will provide a unique opportunity to explore the high-energy frontier, enabling direct searches for physics beyond the Standard Model at an unprecedented energy scale of a few tens of TeV. However, this comes with its own set of challenges, like how well the top quark tagging and W boson tagging will work for particles with extremely high transverse momenta. In this paper, we have investigated the identification of boosted W boson jets and boosted top quark jets in the context of three BSM scenarios: heavy neutral gauge boson (Z'), heavy neutral Higgs boson (H), and heavy vector-like quark (B'). Jets emanating from

the decay of such high-mass particles are highly energetic up to tens of TeV and, thus, are highly boosted.

The kinematic properties, such as jet mass, are strongly influenced by the p_T of the jets. For ultra-boosted jets, jet mass and other variables will be significantly modified by the presence of underlying events, particularly initial and final state radiations, proportional to the jet radius. We have demonstrated the importance of using a dynamic jet radius, dependent on the transverse momentum of jets, to improve the reconstruction of top and W jets. Our results show that this approach can significantly reduce jet contamination and correct various jet properties to some extent. Additionally, we have shown the extent to which improved calorimeter resolution can affect jets with high transverse momentum. Track-based information is more powerful in terms of providing an accurate description of the jets owing to their higher resolution. We perform a brief hypothetical study showing that increasing the angular resolution from 1 mrad to 5 mrad increases the overlap between signal and background distributions of track-based observables, and the effect is more pronounced for $\mathcal{O}(10)$ TeV jets.

Furthermore, we have explored the application of machine learning techniques, including Extreme Gradient Boosted Decision Trees (XGBoost) and convolutional neural networks (CNNs), to distinguish top jets and W jets from QCD jets. The variable-based tagging performs the best when both tower and track-based observables are used as input features. In the case of image-based classification, we have used particle-flow (PF) jet images with ECAL tower resolution. Our findings during the comparative study of 14 TeV and 100 TeV jets indicate that the low-level jet constituent-based CNN, which outperforms observable-based XGBoost at 14 TeV, performs poorly at 100 TeV. Our focus in this study has been exploratory. This study excludes the simulation of pile-up. To extract the maximum sensitivity, the next step would be to use the ML taggers from this study and fit the resultant invariant mass spectrum with detailed signal and background models involving full pile-up simulation, and performing a full statistical analysis, as is usually done in LHC resonance searches.

We have tested the three BSM scenarios with the trained models and calculated the upper limits on cross-sections at 95% CL. Assuming only statistical uncertainty, the 95% CL upper limits on the cross-section from Analysis III are as follows. For the $Z' \rightarrow t\bar{t}$ channel, the limits are 4.2 fb, 0.95 fb, 0.26 fb, and 0.099 fb for $m_{Z'} = 5, 10, 15,$ and 20 TeV, respectively. For the heavy scalar $H \rightarrow W^+W^-$ channel, the limits are 0.69 fb at $m_H = 5$ TeV, 0.14 fb at 10 TeV, 0.13 fb at 15 TeV, and 0.041 fb at 20 TeV. For the vector-like quark process $pp \rightarrow jB' \rightarrow jtW$, the corresponding limits are 3.0 fb at $m_{B'} = 5$ TeV and 1.2 fb at 10 TeV.

The variation in the upper limits with 5% systematics also presents an interesting implication. The resonant masses that lie at the extreme reach of the LHC, and are only marginally

accessible at the LHC, shall also be the most challenging to probe at the FCC, due to the dominance of systematic effects in the regime. Overcoming this challenge shall require a more detailed analysis of the background. Finally, we show that the results also depend on the width of the BSM particle. As the width increases with the mass, reconstructing the particle at the FCC-hh will pose a challenge for multi-TeV resonances.

This study advances our understanding of jets in the exceptionally high-energy regime envisioned for future particle physics experiments. The results presented in this paper demonstrate the feasibility of identifying boosted top and W jets at the FCC-hh and highlight the potential for discovering new physics at a very high mass scale. By developing robust and efficient tagging techniques for hadronically decaying top quarks and W bosons, our work contributes to the ongoing efforts to demonstrate the discovery potential of the FCC-hh. We plan on further optimization of the top/ W jet tagging performance, using more advanced ML techniques in future studies.

9 Acknowledgments

The work of SM is supported by an initiation grant (IITK/PHY/2023282) received from IIT Kanpur. The works of BB, SB, and DC are supported by the Core Research Grants CRG/2021/007579 and CRG/2022/001922 of the Science and Engineering Research Board (SERB), Government of India. BB also acknowledges the MATRICS Grant (MTR/2022/000264) of the Science and Engineering Research Board (SERB), Government of India. DC also acknowledges funding from an initiation grant IITK/PHY/2019413 at IIT Kanpur. CB and BB are grateful to the Center for High Energy Physics, Indian Institute of Science, for the cluster facility.

A Jet energy response and resolution

As stated earlier, the top jets and the QCD have been generated in fixed p_T bins of 2 TeV. However, boosted objects with high p_T might lose energy due to radiation and smearing within the detector and lie in a p_T bin with lower energy. On the other hand, calorimeters and tracking systems introduce smearing effects that can slightly alter the reconstructed p_T of the jet compared to the original p_T , causing the reconstructed jet p_T to acquire higher values than the generated jet p_T .

Generally, a typical general-purpose detector cannot measure the energy (and p_T) of jets perfectly. The measured energy of a jet is usually corrected to match the energy of generated particle jets. The correction factors are generally functions of momentum and pseudorapidity, and they help to bring the p_T of the reconstructed jet in line with the generated jet. We study the extent to which the p_T of the reconstructed jets ($p_T^{(jet)}$) differ from the p_T of the generated jets ($p_T^{(gen)}$) at FCC-hh.

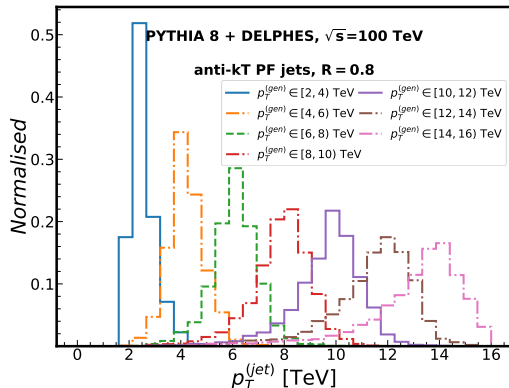


Figure 23: $p_T^{(jet)}$ distributions of top jets for each $p_T^{(gen)}$ bin.

Figure 23 illustrates the jet energy response and resolution for top jets at the FCC-hh. As the $p_T^{(gen)}$ increases, the reconstructed $p_T^{(jet)}$ shows an increasingly broad distribution, reflecting the deterioration of jet resolution at higher energies. The response is biased towards lower reconstructed values, though a small fraction of jets are also smeared upward. Similar behavior is observed for QCD and W jets.

We study the impact of using a poorer energy resolution and calorimeter segmentation on the jet mass observable. Firstly, we increase the S and C co-efficients of Equation 3.2 to 30%. Additionally, we set the ECAL granularity to HCAL granularity. Simulating the FCC-hh detector conditions using these parameters, we construct PF jets with the p_T dependent

radius. Figure 24 shows the variation in the m_{jet} distribution for the default and changed scenarios.

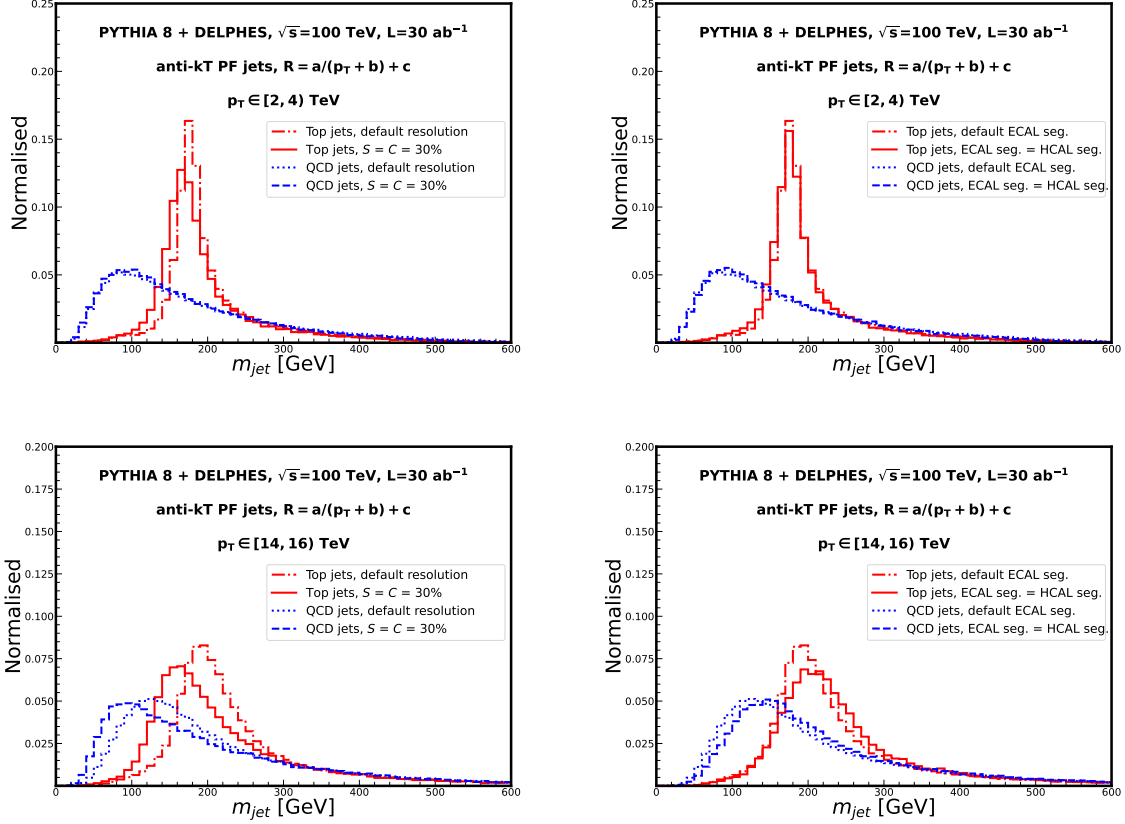


Figure 24: Normalised m_{jet} distribution of 2–4 TeV ((a), (b)) and 14–16 TeV ((c), (d)) top jets and QCD jets using different calorimeter configurations. Subfigures (a), (c) show the change in m_{jet} when the energy resolution is varied. Subfigures (b), (d) show the change in m_{jet} when the angular resolution is varied.

We observe that the jet mass resolution worsens due to the increased smearing and poor reconstruction in the calorimeter, and the impact is greater for 14–16 TeV jets compared to 2–4 TeV jets.

B Efficiencies used by DELPHES

In the following table, we list the identification efficiencies and tracking efficiency for charged hadrons used by the FCC-hh card of DELPHES. The charged hadrons and electron tracking efficiencies are approximated to be similar in DELPHES.

Type	$ \eta < 2.5$	$2.5 < \eta < 4.0$	$4.0 < \eta < 6.0$	$ \eta > 6.0$
Tracking Efficiency (Charged Hadrons)				
$p_T < 0.5$ GeV	0%	0%	0%	0%
$0.5 < p_T < 1.0$ GeV	90%	85%	80%	0%
$p_T > 1.0$ GeV	95%	90%	85%	0%
Electron Identification Efficiency				
$p_T < 4$ GeV	0%	0%	0%	0%
$p_T > 4$ GeV	95%	90%	85%	0%
Muon Identification Efficiency				
$p_T < 4$ GeV	0%	0%	0%	0%
$p_T > 4$ GeV	99%	99%	99%	0%
Photon Identification Efficiency				
$1 < p_T < 5$ GeV	70%	60%	50%	50%
$5 < p_T < 10$ GeV	85%	80%	70%	70%
$p_T > 10$ GeV	95%	90%	80%	80%

Table 12: Efficiencies (in %) for tracking and particle identification as a function of p_T and $|\eta|$ for charged hadrons, electrons, muons, and photons [89].

C Jet after soft drop

For fixed radius jets, the soft drop algorithm is unable to correct the long tail in the jet mass distribution of 14–16 TeV jets. We see this in Figure 25.

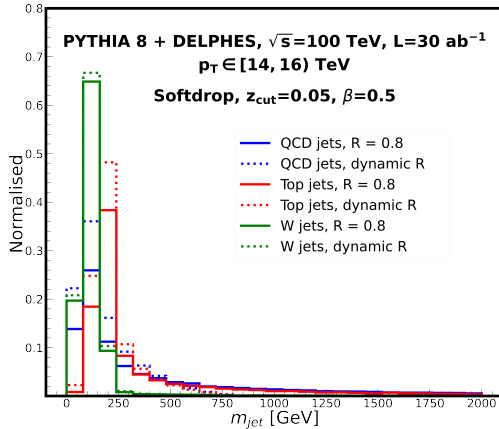


Figure 25: Jet mass distribution for top, QCD, and W jets with $p_T = 14$ TeV, after applying grooming on fixed R and variable R jets.

We now present the distributions of the jet mass (m_{jet}) after applying the softdrop algorithm on the reclustered jets. The distributions are shown for two extreme ends of the p_T spectrum, 2–4 TeV jets and 14–16 TeV jets, to highlight the effect of the softdrop with jet p_T . We vary the parameters of softdrop z_{cut} and β defined in Equation 5.5.

Figures 26 and 27 show the m_{jet} distributions of 2–4 TeV jets and 14–16 TeV jets respectively. The z parameter is fixed at 0.05 while β is varied from 0.2 to 2.0. Similar m_{jet} distributions for a fixed $z = 0.08$ are presented in Figures 28 and 29 for 2–4 TeV jets and 14–16 TeV jets respectively. Figures 30 and 31 show the distributions for $z = 0.1$, while Figures 32 and 33 show the distributions for $z = 0.2$.

As z increases, the soft components of the jets are removed more aggressively, hence we see an increase in small peaks at lower m_{jet} values, in top and W jet distributions. Increasing β for a fixed z results in less grooming, since a large β indicates that only wide-angle radiations are removed.

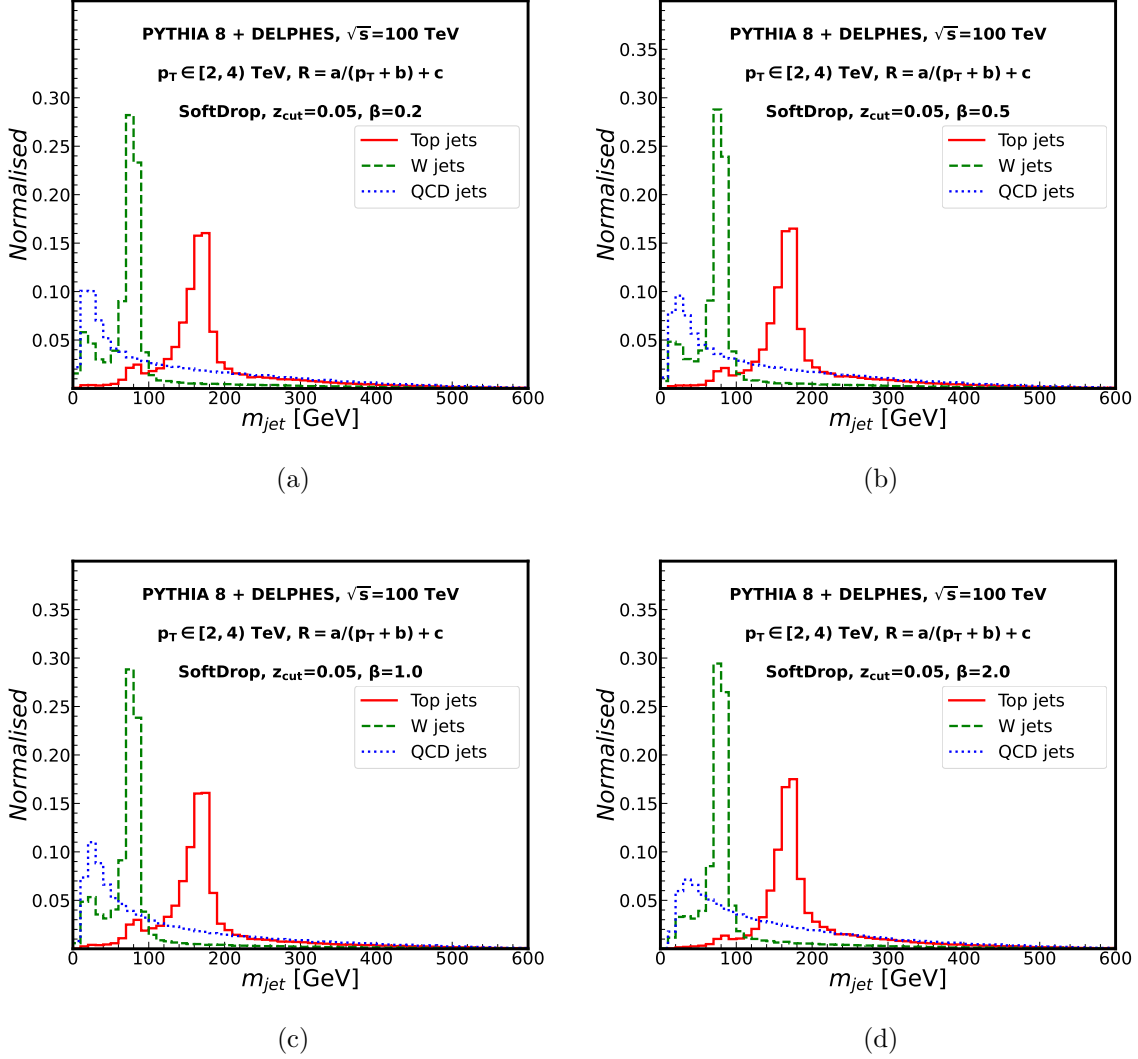


Figure 26: Normalised m_{jet} distribution of 2–4 TeV top jets and QCD jets, after applying softdrop grooming with parameters $z = 0.05$ (*fixed*), and (a) $\beta = 0.2$, (b) $\beta = 0.5$, (c) $\beta = 1.0$, (d) $\beta = 2.0$.

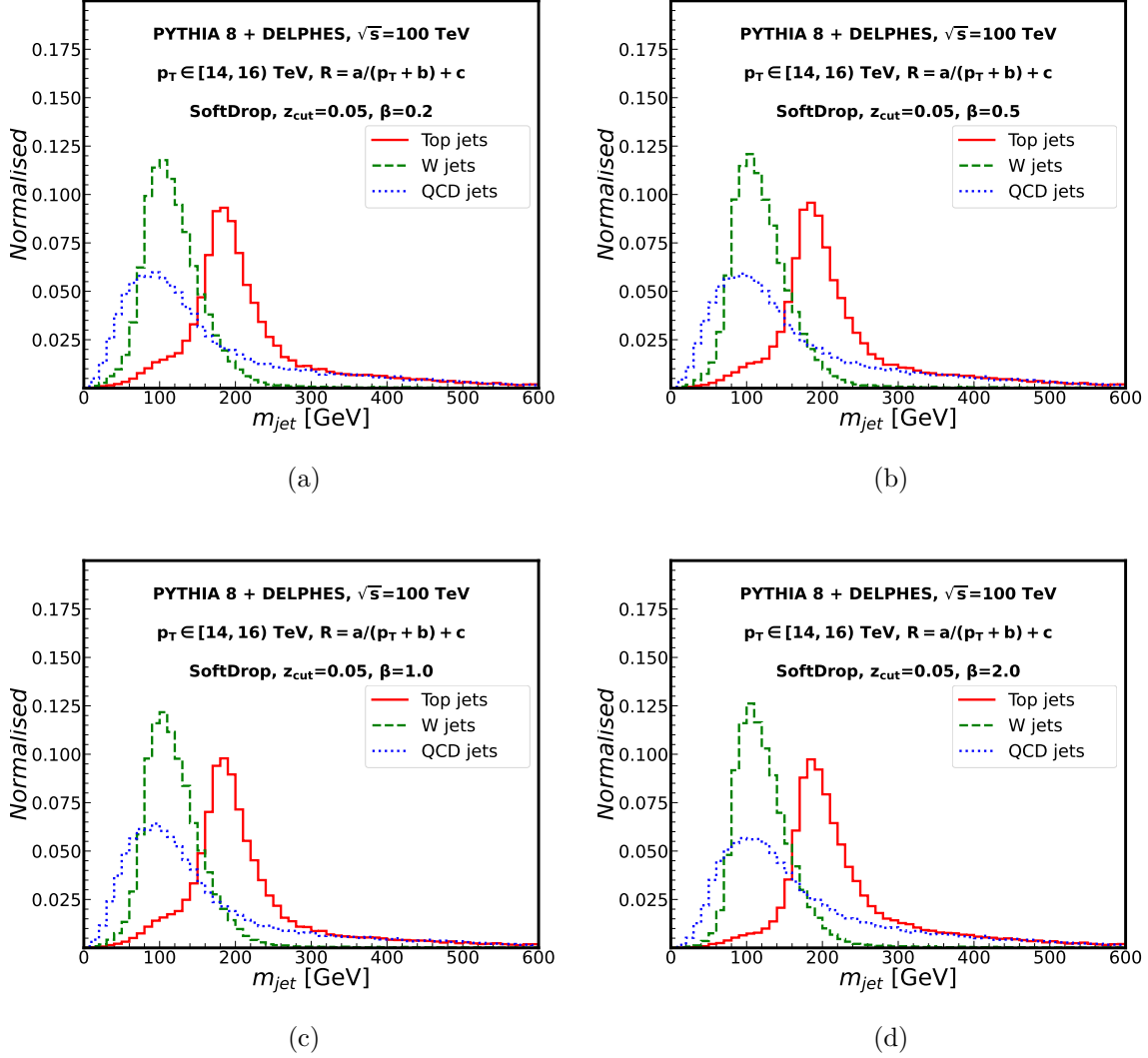


Figure 27: Normalised m_{jet} distribution of 14–16 TeV top jets and QCD jets, after applying softdrop grooming with parameters $z = 0.05$ (*fixed*), and (a) $\beta = 0.2$, (b) $\beta = 0.5$, (c) $\beta = 1.0$, (d) $\beta = 2.0$.

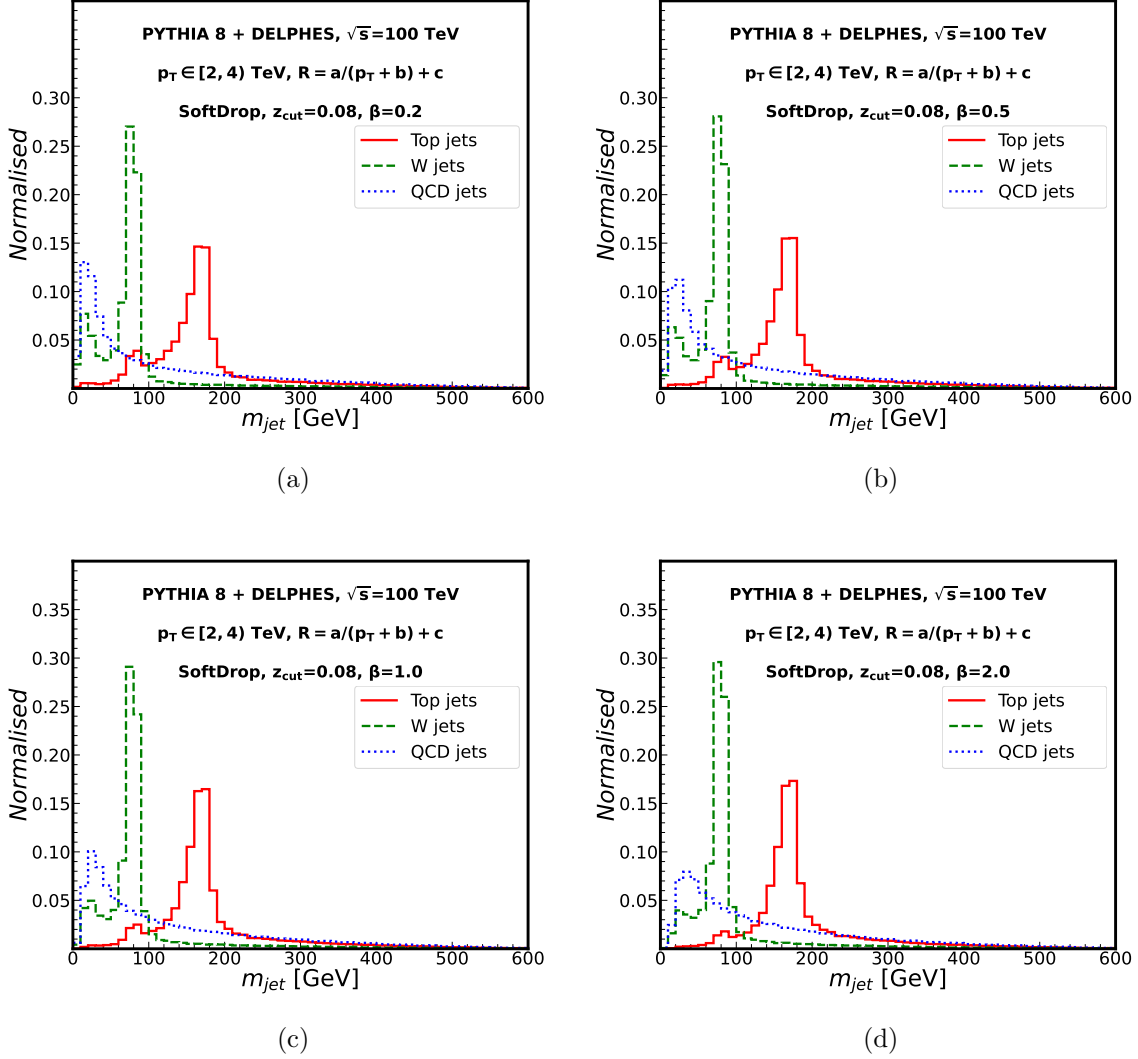


Figure 28: Normalised m_{jet} distribution of 2–4 TeV top jets and QCD jets, after applying softdrop grooming with parameters $z = 0.08$ (*fixed*), and (a) $\beta = 0.2$, (b) $\beta = 0.5$, (c) $\beta = 1.0$, (d) $\beta = 2.0$.

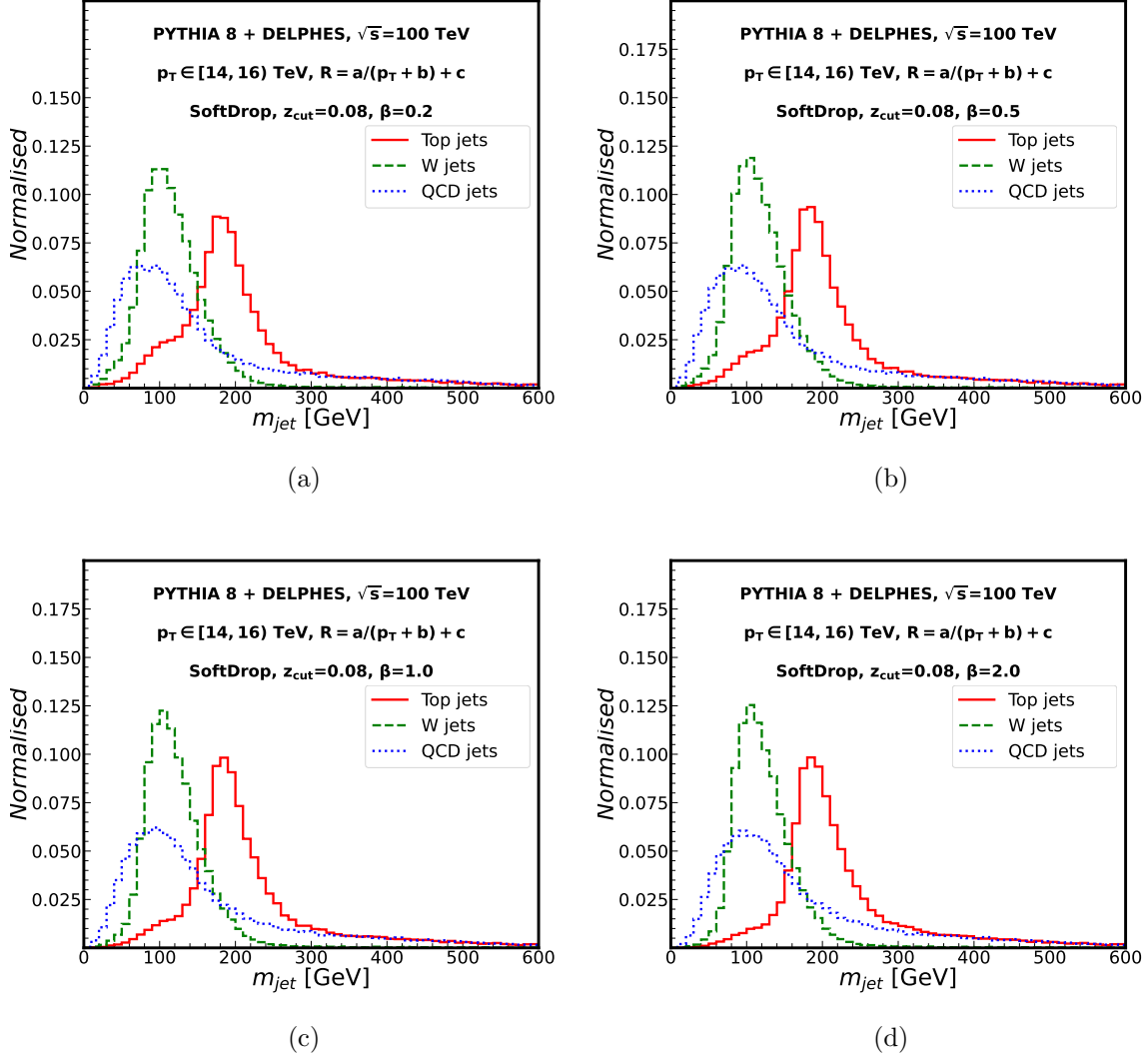


Figure 29: Normalised m_{jet} distribution of 14–16 TeV top jets and QCD jets, after applying softdrop grooming with parameters $z = 0.08$ (*fixed*), and (a) $\beta = 0.2$, (b) $\beta = 0.5$, (c) $\beta = 1.0$, (d) $\beta = 2.0$.

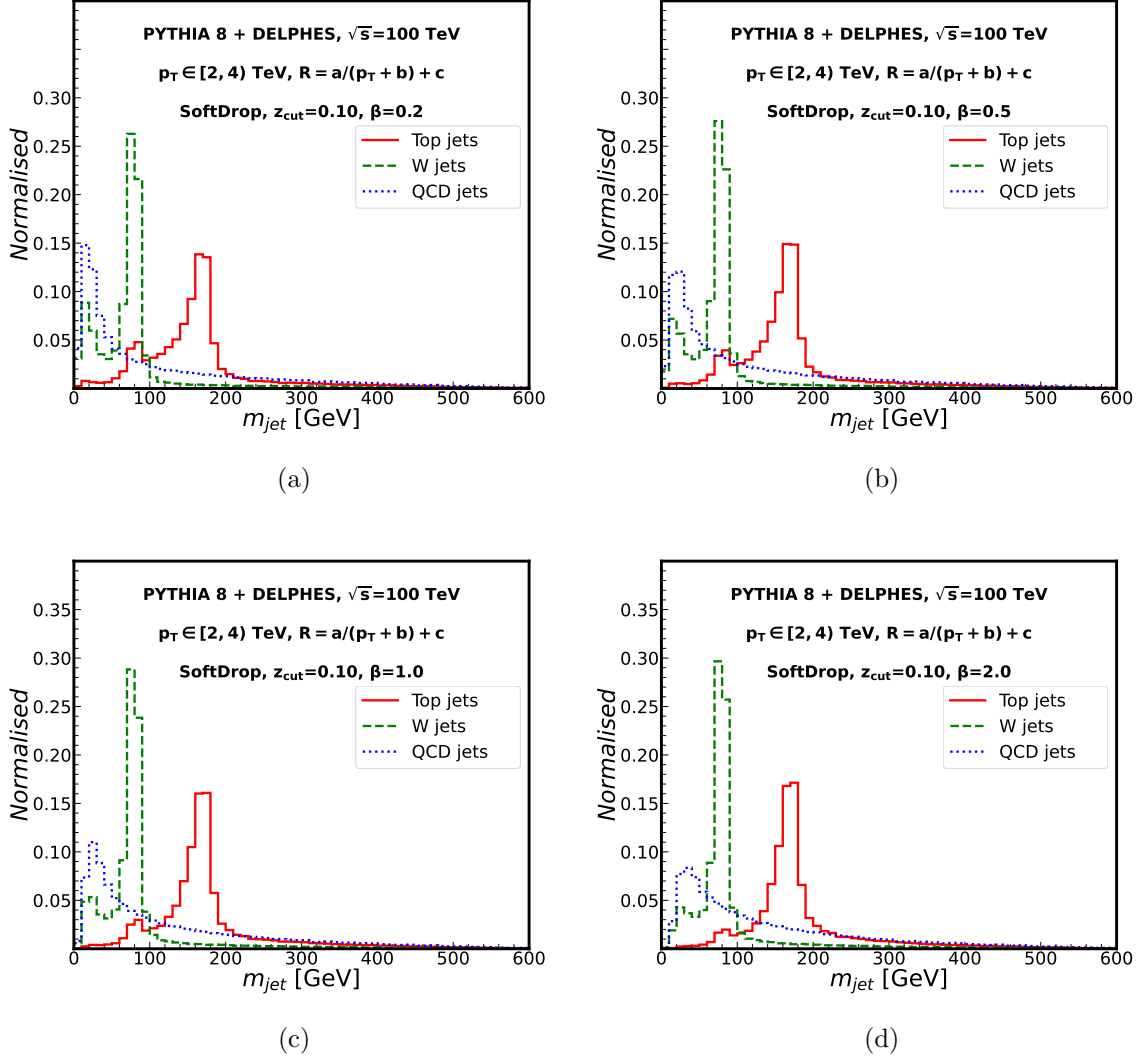


Figure 30: Normalised m_{jet} distribution of 2–4 TeV top jets and QCD jets, after applying softdrop grooming with parameters $z = 0.1$ (*fixed*), and (a) $\beta = 0.2$, (b) $\beta = 0.5$, (c) $\beta = 1.0$, (d) $\beta = 2.0$.

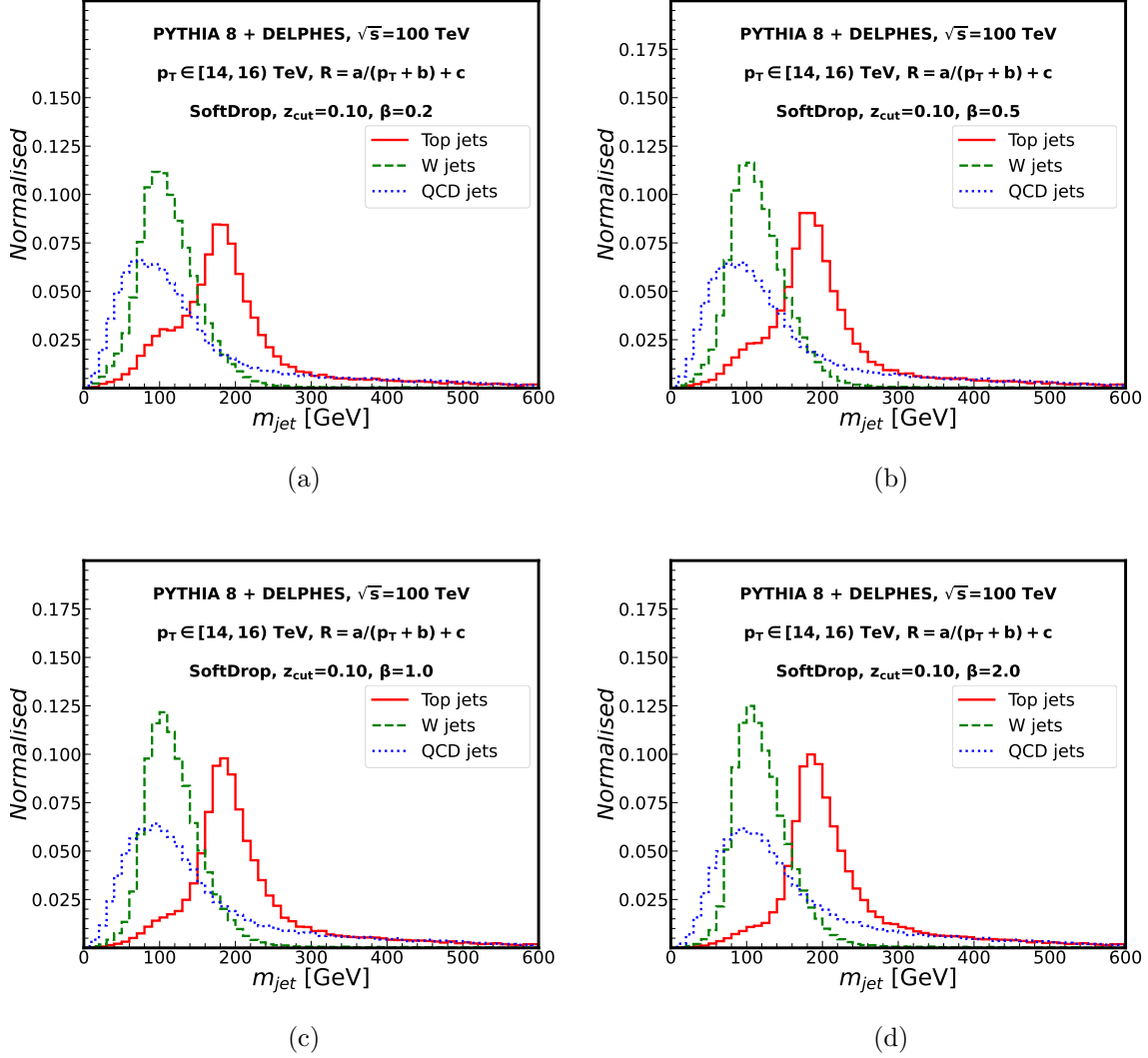


Figure 31: Normalised m_{jet} distribution of 14–16 TeV top jets and QCD jets, after applying softdrop grooming with parameters $z = 0.1$ (*fixed*), and (a) $\beta = 0.2$, (b) $\beta = 0.5$, (c) $\beta = 1.0$, (d) $\beta = 2.0$.

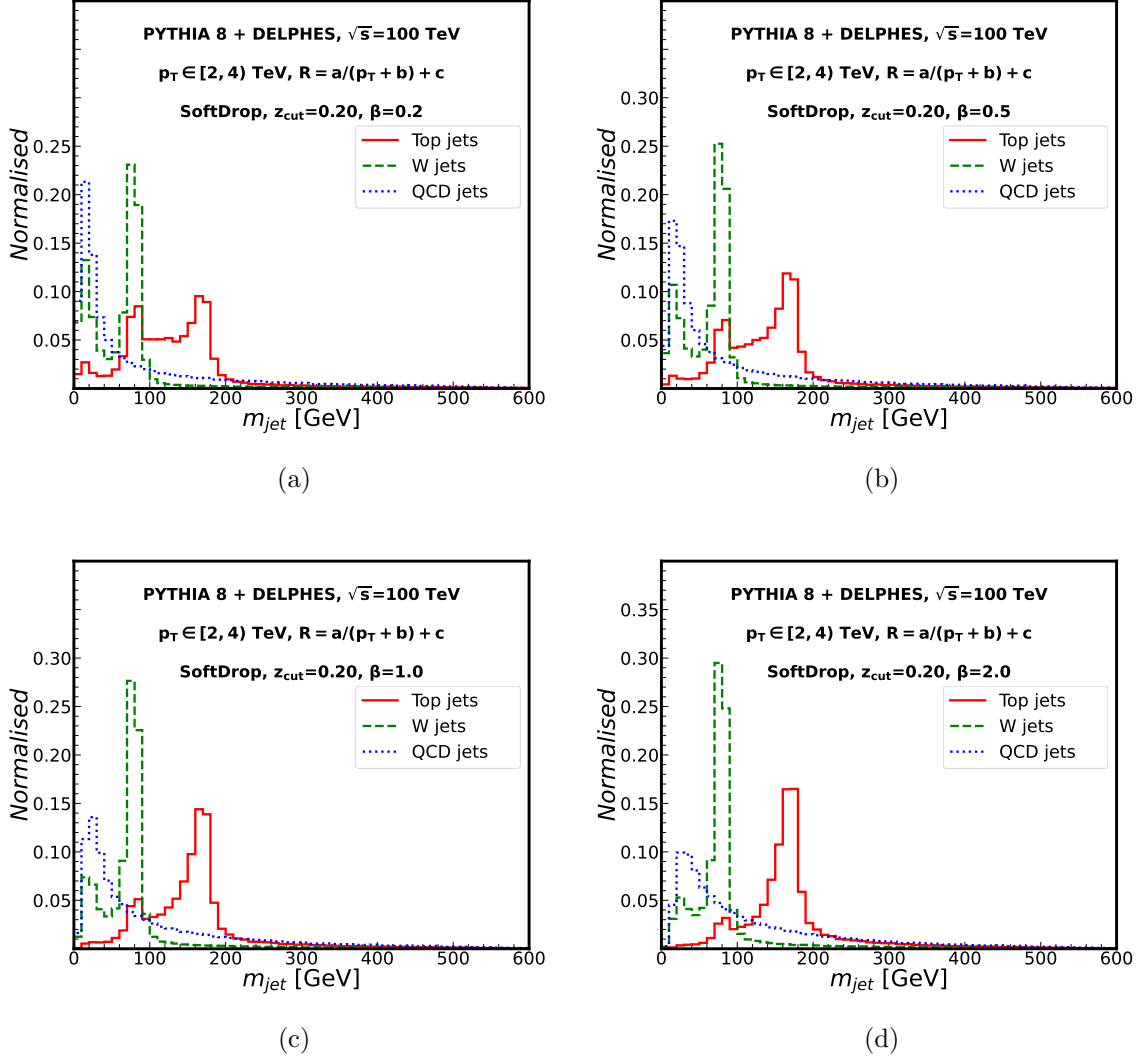


Figure 32: Normalised m_{jet} distribution of 2–4 TeV top jets and QCD jets, after applying softdrop grooming with parameters $z = 0.2$ (*fixed*), and (a) $\beta = 0.2$, (b) $\beta = 0.5$, (c) $\beta = 1.0$, (d) $\beta = 2.0$.

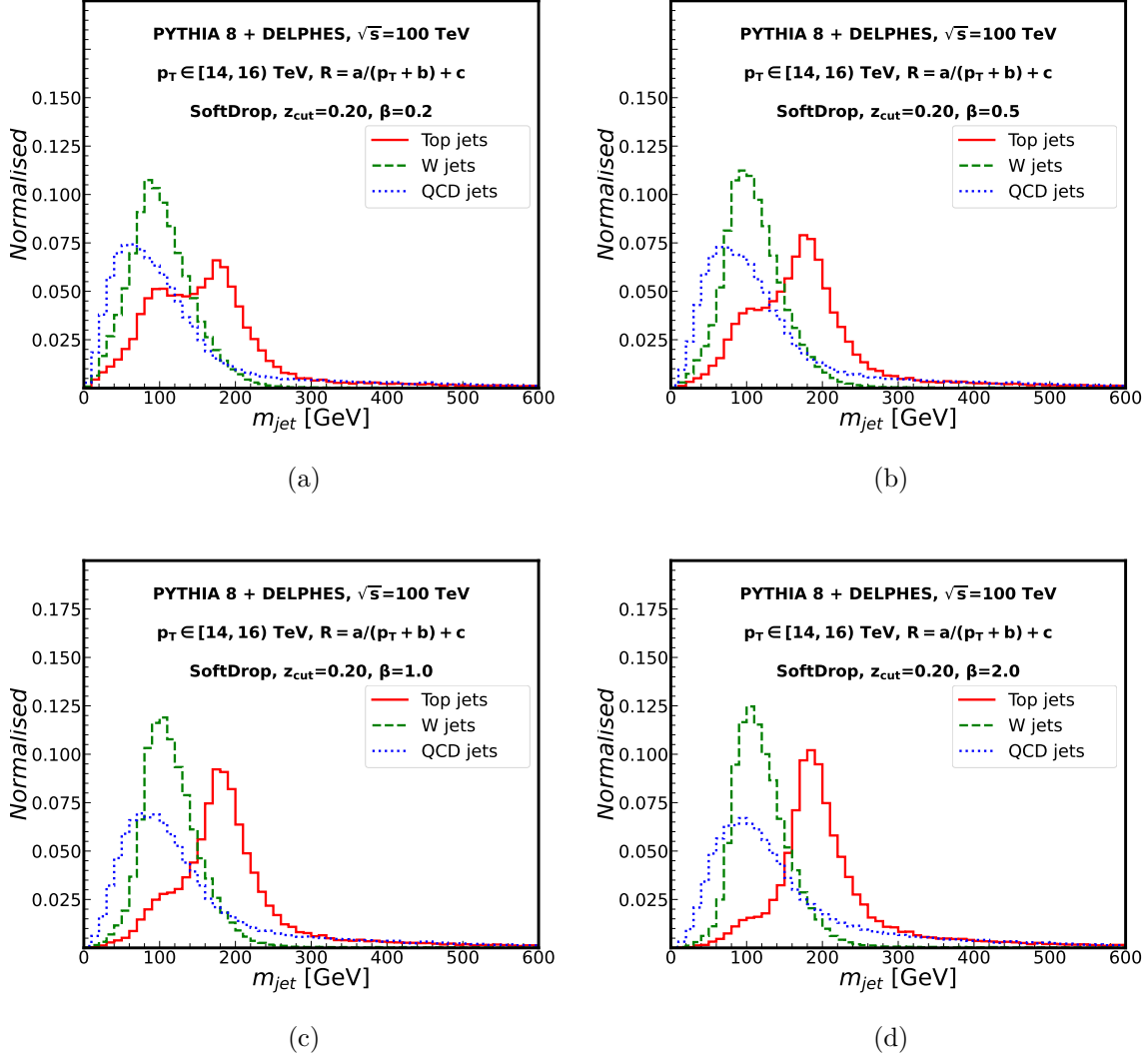


Figure 33: Normalised m_{jet} distribution of 14–16 TeV top jets and QCD jets, after applying softdrop grooming with parameters $z = 0.2$ (*fixed*), and (a) $\beta = 0.2$, (b) $\beta = 0.5$, (c) $\beta = 1.0$, (d) $\beta = 2.0$.

References

- [1] ATLAS collaboration, G. Aad et al., *Observation of a new particle in the search for the Standard Model Higgs boson with the ATLAS detector at the LHC*, *Phys. Lett. B* **716** (2012) 1–29, [[1207.7214](#)].
- [2] CMS collaboration, S. Chatrchyan et al., *Observation of a New Boson at a Mass of 125 GeV with the CMS Experiment at the LHC*, *Phys. Lett. B* **716** (2012) 30–61, [[1207.7235](#)].
- [3] G. Heinrich, *Collider Physics at the Precision Frontier*, *Phys. Rept.* **922** (2021) 1–69, [[2009.00516](#)].
- [4] CMS collaboration, A. Tumasyan et al., *Measurement of the Higgs boson width and evidence of its off-shell contributions to ZZ production*, *Nature Phys.* **18** (2022) 1329–1334, [[2202.06923](#)].
- [5] ATLAS collaboration, *Combined Measurement of the Higgs Boson Mass from the $H \rightarrow \gamma\gamma$ and $H \rightarrow ZZ^* \rightarrow 4\ell$ Decay Channels with the ATLAS Detector Using $\sqrt{s} = 7, 8,$ and 13 TeV pp Collision Data*, *Phys. Rev. Lett.* **131** (Dec, 2023) 251802.
- [6] ATLAS collaboration, G. Aad et al., *Measurement of the $H \rightarrow \gamma\gamma$ and $H \rightarrow ZZ^* \rightarrow 4\ell$ cross-sections in pp collisions at $\sqrt{s} = 13.6$ TeV with the ATLAS detector*, *Eur. Phys. J. C* **84** (2024) 78, [[2306.11379](#)].
- [7] PARTICLE DATA GROUP collaboration, S. Navas et al., *Review of particle physics*, *Phys. Rev. D* **110** (2024) 030001.
- [8] P. Langacker, *The physics of heavy Z' gauge bosons*, *Rev. Mod. Phys.* **81** (Aug, 2009) 1199–1228.
- [9] L. Basso, A. Belyaev, S. Moretti and C. H. Shepherd-Themistocleous, *Phenomenology of the minimal B-L extension of the Standard model: Z' and neutrinos*, *Phys. Rev. D* **80** (2009) 055030, [[0812.4313](#)].
- [10] S. Amrith, J. M. Butterworth, F. F. Deppisch, W. Liu, A. Varma and D. Yallup, *LHC Constraints on a B – L Gauge Model using Contur*, *JHEP* **05** (2019) 154, [[1811.11452](#)].
- [11] T. D. Lee, *A Theory of Spontaneous T Violation*, *Phys. Rev. D* **8** (Aug, 1973) 1226–1239.
- [12] G. C. Branco, P. M. Ferreira, L. Lavoura, M. N. Rebelo, M. Sher and J. P. Silva, *Theory and phenomenology of two-Higgs-doublet models*, *Phys. Rept.* **516** (2012) 1–102, [[1106.0034](#)].
- [13] D. Chowdhury and O. Eberhardt, *Global fits of the two-loop renormalized Two-Higgs-Doublet model with soft Z_2 breaking*, *JHEP* **11** (2015) 052, [[1503.08216](#)].
- [14] D. Chowdhury and O. Eberhardt, *Update of Global Two-Higgs-Doublet Model Fits*, *JHEP* **05** (2018) 161, [[1711.02095](#)].
- [15] F. Kling, H. Li, A. Pyarelal, H. Song and S. Su, *Exotic Higgs Decays in Type-II 2HDMs at the LHC and Future 100 TeV Hadron Colliders*, *JHEP* **06** (2019) 031, [[1812.01633](#)].
- [16] F. Kling, S. Su and W. Su, *2HDM Neutral Scalars under the LHC*, *JHEP* **06** (2020) 163, [[2004.04172](#)].

- [17] P. Draper, A. Ekstedt and H. E. Haber, *A natural mechanism for approximate Higgs alignment in the 2HDM*, *JHEP* **05** (2021) 235, [[2011.13159](#)].
- [18] L. Wang, J. M. Yang and Y. Zhang, *Two-Higgs-doublet models in light of current experiments: a brief review*, *Commun. Theor. Phys.* **74** (2022) 097202, [[2203.07244](#)].
- [19] M. Mangano, P. Azzi, M. Benedikt, A. Blondel, D. A. Britzger, A. Dainese et al., *FCC Physics Opportunities: Future Circular Collider Conceptual Design Report Volume 1. Future Circular Collider*, Tech. Rep. CERN-ACC-2018-0056, CERN, Geneva, 2019. 10.1140/epjc/s10052-019-6904-3.
- [20] M. Benedikt, M. Capeans Garrido, F. Cerutti, B. Goddard, J. Gutleber, J. M. Jimenez et al., *FCC-hh: The Hadron Collider: Future Circular Collider Conceptual Design Report Volume 3. Future Circular Collider*, Tech. Rep. CERN-ACC-2018-0058, CERN, Geneva, 2019. 10.1140/epjst/e2019-900087-0.
- [21] A. J. Larkoski, F. Maltoni and M. Selvaggi, *Tracking down hyper-boosted top quarks*, *JHEP* **06** (2015) 032, [[1503.03347](#)].
- [22] J. Bonilla et al., *Jets and Jet Substructure at Future Colliders*, *Front. in Phys.* **10** (2022) 897719, [[2203.07462](#)].
- [23] T. Bandyopadhyay, S. Mukherjee, S. Raychaudhuri and R. Vinze, *Kinematics and Particle Identification at Very High Energy Colliders*, *Springer Proc. Phys.* **304** (2024) 1251–1253.
- [24] C. Yeh, S. Chekanov, A. Kotwal, J. Proudfoot, S. Sen, N. Tran et al., *Studies of granularity of a hadronic calorimeter for tens-of-TeV jets at a 100 TeV pp collider*, *Journal of Instrumentation* **14** (may, 2019) P05008.
- [25] J. Thaler and K. Van Tilburg, *Identifying Boosted Objects with N-subjettiness*, *JHEP* **03** (2011) 015, [[1011.2268](#)].
- [26] A. J. Larkoski, G. P. Salam and J. Thaler, *Energy Correlation Functions for Jet Substructure*, *JHEP* **06** (2013) 108, [[1305.0007](#)].
- [27] A. J. Larkoski, I. Moulton and D. Neill, *Power Counting to Better Jet Observables*, *JHEP* **12** (2014) 009, [[1409.6298](#)].
- [28] A. J. Larkoski, I. Moulton and D. Neill, *Building a Better Boosted Top Tagger*, *Phys. Rev. D* **91** (2015) 034035, [[1411.0665](#)].
- [29] A. J. Larkoski, I. Moulton and D. Neill, *Analytic Boosted Boson Discrimination*, *JHEP* **05** (2016) 117, [[1507.03018](#)].
- [30] I. Moulton, L. Necib and J. Thaler, *New Angles on Energy Correlation Functions*, *JHEP* **12** (2016) 153, [[1609.07483](#)].
- [31] J. Erdmann, S. Guindon, K. Kroeninger, B. Lemmer, O. Nackenhorst, A. Quadt et al., *A likelihood-based reconstruction algorithm for top-quark pairs and the KLFilter framework*, *Nucl. Instrum. Meth. A* **748** (2014) 18–25, [[1312.5595](#)].

- [32] L. G. Almeida, M. Backović, M. Cliche, S. J. Lee and M. Perelstein, *Playing Tag with ANN: Boosted Top Identification with Pattern Recognition*, *JHEP* **07** (2015) 086, [[1501.05968](#)].
- [33] G. Kasieczka, T. Plehn, M. Russell and T. Schell, *Deep-learning Top Taggers or The End of QCD?*, *JHEP* **05** (2017) 006, [[1701.08784](#)].
- [34] M. Erdmann, B. Fischer and M. Rieger, *Jet-parton assignment in $t\bar{t}H$ events using deep learning*, *JINST* **12** (2017) P08020, [[1706.01117](#)].
- [35] A. Butter, G. Kasieczka, T. Plehn and M. Russell, *Deep-learned Top Tagging with a Lorentz Layer*, *SciPost Phys.* **5** (2018) 028, [[1707.08966](#)].
- [36] S. Macaluso and D. Shih, *Pulling Out All the Tops with Computer Vision and Deep Learning*, *JHEP* **10** (2018) 121, [[1803.00107](#)].
- [37] L. Moore, K. Nordström, S. Varma and M. Fairbairn, *Reports of My Demise Are Greatly Exaggerated: N -subjettiness Taggers Take On Jet Images*, *SciPost Phys.* **7** (2019) 036, [[1807.04769](#)].
- [38] H. Qu and L. Gouskos, *ParticleNet: Jet Tagging via Particle Clouds*, *Phys. Rev. D* **101** (2020) 056019, [[1902.08570](#)].
- [39] A. Butter et al., *The Machine Learning landscape of top taggers*, *SciPost Phys.* **7** (2019) 014, [[1902.09914](#)].
- [40] T. S. Roy and A. H. Vijay, *A robust anomaly finder based on autoencoders*, [1903.02032](#).
- [41] S. Diefenbacher, H. Frost, G. Kasieczka, T. Plehn and J. M. Thompson, *CapsNets Continuing the Convolutional Quest*, *SciPost Phys.* **8** (2020) 023, [[1906.11265](#)].
- [42] A. Chakraborty, S. H. Lim, M. M. Nojiri and M. Takeuchi, *Neural Network-based Top Tagger with Two-Point Energy Correlations and Geometry of Soft Emissions*, *JHEP* **07** (2020) 111, [[2003.11787](#)].
- [43] S. Bhattacharya, M. Guchait and A. H. Vijay, *Boosted top quark tagging and polarization measurement using machine learning*, *Phys. Rev. D* **105** (2022) 042005, [[2010.11778](#)].
- [44] A. Shmakov, M. J. Fenton, T.-W. Ho, S.-C. Hsu, D. Whiteson and P. Baldi, *SPANet: Generalized permutationless set assignment for particle physics using symmetry preserving attention*, *SciPost Phys.* **12** (2022) 178, [[2106.03898](#)].
- [45] S. H. Lim and M. M. Nojiri, *Morphology for jet classification*, *Phys. Rev. D* **105** (2022) 014004, [[2010.13469](#)].
- [46] F. A. Dreyer and H. Qu, *Jet tagging in the Lund plane with graph networks*, *JHEP* **03** (2021) 052, [[2012.08526](#)].
- [47] J. A. Aguilar-Saavedra, *Pulling the Higgs and top needles from the jet stack with feature extended supervised tagging*, *Eur. Phys. J. C* **81** (2021) 734, [[2102.01667](#)].
- [48] M. Andrews et al., *End-to-end jet classification of boosted top quarks with the CMS open data*, *EPJ Web Conf.* **251** (2021) 04030, [[2104.14659](#)].

- [49] H. Qu, C. Li and S. Qian, *Particle Transformer for Jet Tagging*, [2202.03772](#).
- [50] F. A. Dreyer, R. Grabarczyk and P. F. Monni, *Leveraging universality of jet taggers through transfer learning*, *Eur. Phys. J. C* **82** (2022) 564, [[2203.06210](#)].
- [51] I. Ahmed, A. Zada, M. Waqas and M. U. Ashraf, *Application of deep learning in top pair and single top quark production at the LHC*, *Eur. Phys. J. Plus* **138** (2023) 795, [[2203.12871](#)].
- [52] J. M. Munoz, I. Batatia and C. Ortner, *Boost invariant polynomials for efficient jet tagging*, *Mach. Learn. Sci. Tech.* **3** (2022) 04LT05, [[2207.08272](#)].
- [53] S. K. Choi, J. Li, C. Zhang and R. Zhang, *Automatic detection of boosted Higgs boson and top quark jets in an event image*, *Phys. Rev. D* **108** (2023) 116002, [[2302.13460](#)].
- [54] M. He and D. Wang, *Quark/gluon discrimination and top tagging with dual attention transformer*, *Eur. Phys. J. C* **83** (2023) 1116, [[2307.04723](#)].
- [55] A. Bogatskiy, T. Hoffman, D. W. Miller, J. T. Offermann and X. Liu, *Explainable equivariant neural networks for particle physics: PELICAN*, *JHEP* **03** (2024) 113, [[2307.16506](#)].
- [56] W. Shen, D. Wang and J. M. Yang, *Hierarchical high-point Energy Flow Network for jet tagging*, *JHEP* **09** (2023) 135, [[2308.08300](#)].
- [57] B. Işıldak, A. Hayreter, M. Hüdaverdi, F. İlgin, S. Salva, E. Şimşek et al., *Investigating the Violation of Charge-parity Symmetry Through Top-quark ChromoElectric Dipole Moments by Using Machine Learning Techniques*, *Acta Phys. Polon. B* **54** (2023) 5–A4, [[2306.11683](#)].
- [58] R. Sahu and K. Ghosh, *ML-based top taggers: Performance, uncertainty and impact of tower \mathcal{E} tracker data integration*, *SciPost Phys.* **17** (2024) 166, [[2309.01568](#)].
- [59] P. Baroň, J. Kvita, R. Přívara, J. Tomeček and R. Vodák, *Application of Machine Learning Based Top Quark and W Jet Tagging to Hadronic Four-Top Final States Induced by SM as well as BSM Processes*, in *16th International Workshop on Top Quark Physics*, 10, 2023. [2310.13009](#).
- [60] A. Bogatskiy, T. Hoffman and J. T. Offermann, *19 Parameters Is All You Need: Tiny Neural Networks for Particle Physics*, in *37th Conference on Neural Information Processing Systems*, 10, 2023. [2310.16121](#).
- [61] R. Liu, A. Gandrakota, J. Ngadiuba, M. Spiropulu and J.-R. Vlimant, *Efficient and Robust Jet Tagging at the LHC with Knowledge Distillation*, in *37th Conference on Neural Information Processing Systems*, no. FERMILAB-PUB-23-748-CMS, 11, 2023. [2311.14160](#).
- [62] J. Batson and Y. F. Kahn, *Scaling laws in jet classification*, *SciPost Phys. Core* **8** (2025) 034, [[2312.02264](#)].
- [63] A. Furuichi, S. H. Lim and M. M. Nojiri, *Jet classification using high-level features from anatomy of top jets*, *JHEP* **07** (2024) 146, [[2312.11760](#)].
- [64] V. S. Ngairangbam and M. Spannowsky, *Interpretable deep learning models for the inference and classification of LHC data*, *JHEP* **05** (2024) 004, [[2312.12330](#)].

- [65] ATLAS collaboration, G. Aad et al., *Search for $t\bar{t}$ resonances in fully hadronic final states in pp collisions at $\sqrt{s} = 13$ TeV with the ATLAS detector*, *JHEP* **10** (2020) 061, [[2005.05138](#)].
- [66] ATLAS collaboration, *Boosted hadronic vector boson and top quark tagging with ATLAS using Run 2 data*, Tech. Rep. ATL-PHYS-PUB-2020-017, CERN, Geneva, 2020.
- [67] ATLAS collaboration, *Constituent-Based Top-Quark Tagging with the ATLAS Detector*, Tech. Rep. ATL-PHYS-PUB-2022-039, CERN, Geneva, 2022.
- [68] CMS collaboration, S. Chatrchyan et al., *Search for Anomalous $t\bar{t}$ Production in the Highly-Boosted All-Hadronic Final State*, *JHEP* **09** (2012) 029, [[1204.2488](#)].
- [69] CMS collaboration, A. M. Sirunyan et al., *Search for $t\bar{t}$ resonances in highly boosted lepton+jets and fully hadronic final states in proton-proton collisions at $\sqrt{s} = 13$ TeV*, *JHEP* **07** (2017) 001, [[1704.03366](#)].
- [70] CMS collaboration, A. M. Sirunyan et al., *Search for top squark production in fully-hadronic final states in proton-proton collisions at $\sqrt{s} = 13$ TeV*, *Phys. Rev. D* **104** (2021) 052001, [[2103.01290](#)].
- [71] P. Keicher, *Machine Learning in Top Physics in the ATLAS and CMS Collaborations*, in *15th International Workshop on Top Quark Physics*, no. CR-2023/006, 1, 2023. [2301.09534](#).
- [72] B. Bhattacharjee, C. Bose, A. Chakraborty and R. Sengupta, *Boosted top tagging and its interpretation using Shapley values*, *Eur. Phys. J. Plus* **139** (2024) 1131, [[2212.11606](#)].
- [73] C. Bose, A. Chakraborty, S. Chowdhury and S. Dutta, *Interplay of traditional methods and machine learning algorithms for tagging boosted objects*, *Eur. Phys. J. ST* **233** (2024) 2531–2558, [[2408.01138](#)].
- [74] R. Baruah, A. Choudhury, K. Ghosh, S. Mondal and R. Sahu, *Probing sub-TeV Higgsinos aided by a machine-learning-based top tagger in the context of trilinear R -parity violating SUSY*, *Phys. Rev. D* **111** (2025) 095004, [[2412.11862](#)].
- [75] R. K. Barman and S. Biswas, *Top-philic machine learning*, *Eur. Phys. J. ST* **233** (2024) 2497–2530, [[2407.00183](#)].
- [76] K. Fraser, *Probing Undiscovered Particles with Theory and Data-Driven Tools*. PhD thesis, Harvard U. (main), Harvard U., 4, 2024.
- [77] S. Mondal and L. Mastrolorenzo, *Machine learning in high energy physics: a review of heavy-flavor jet tagging at the LHC*, *Eur. Phys. J. ST* **233** (2024) 2657–2686, [[2404.01071](#)].
- [78] S. Chowdhury, A. Chakraborty and S. Dutta, *Boosted top tagging through flavour-violating interactions at the LHC*, *Eur. Phys. J. C* **85** (2025) 231, [[2310.10763](#)].
- [79] A. Choudhury, A. Mondal, S. Mondal and S. Sarkar, *Improving sensitivity of trilinear R -parity violating SUSY searches using machine learning at the LHC*, *Phys. Rev. D* **109** (2024) 035001, [[2308.02697](#)].
- [80] A. Chakraborty, A. De, R. M. Godbole and M. Guchait, *Tagging a boosted top quark with a τ final state*, *Phys. Rev. D* **108** (2023) 035011, [[2304.12846](#)].

- [81] A. Chakraborty, S. Dasmahapatra, H. Day-Hall, B. Ford, S. Jain and S. Moretti, *Fat b-jet analyses using old and new clustering algorithms in new Higgs boson searches at the LHC*, *Eur. Phys. J. C* **83** (2023) 347, [[2303.05189](#)].
- [82] E. Alvarez, M. Szewc, A. Szykman, S. A. Tanco and T. Tarutina, *Exploring unsupervised top tagging using Bayesian inference*, *SciPost Phys. Core* **6** (2023) 046, [[2212.13583](#)].
- [83] D. Alvestad, N. Fomin, J. Kersten, S. Maeland and I. Strümke, *Beyond cuts in small signal scenarios: Enhanced sneutrino detectability using machine learning*, *Eur. Phys. J. C* **83** (2023) 379, [[2108.03125](#)].
- [84] T. Chen and C. Guestrin, *Xgboost: A scalable tree boosting system*, *CoRR* **abs/1603.02754** (2016) , [[1603.02754](#)].
- [85] K. Fukushima, *Neocognitron: A self-organizing neural network model for a mechanism of pattern recognition unaffected by shift in position*, *Biological Cybernetics* **36** (1980) 193–202.
- [86] K. Fukushima, *Artificial vision by multi-layered neural networks: Neocognitron and its advances*, *Neural Networks* **37** (2013) 103–119.
- [87] Y. Lecun, L. Bottou, Y. Bengio and P. Haffner, *Gradient-based learning applied to document recognition*, *Proceedings of the IEEE* **86** (1998) 2278–2324.
- [88] E. Coleman, M. Freytsis, A. Hinzmann, M. Narain, J. Thaler, N. Tran et al., *The importance of calorimetry for highly-boosted jet substructure*, *JINST* **13** (2018) T01003, [[1709.08705](#)].
- [89] M. Selvaggi, *A Delphes parameterisation of the FCC-hh detector*, Tech. Rep. CERN-FCC-PHYS-2020-0003, CERN, Geneva, 2020.
- [90] B. Auerbach, S. Chekanov, J. Love, J. Proudfoot and A. V. Kotwal, *Sensitivity to new high-mass states decaying to $t\bar{t}$ at a 100 TeV collider*, *Phys. Rev. D* **91** (Feb, 2015) 034014.
- [91] C. Hensens, D. Jamin, M. L. Mangano, T. G. Rizzo and M. Selvaggi, *Heavy resonances at energy-frontier hadron colliders*, *Eur. Phys. J. C* **79** (2019) 569, [[1902.11217](#)].
- [92] D. Bertolini, P. Harris, M. Low and N. Tran, *Pileup Per Particle Identification*, *JHEP* **10** (2014) 059, [[1407.6013](#)].
- [93] B. Bhattacharjee, N. Khan and A. Patra, *Anatomy of Heavy Gauge Bosons in a Left-Right Supersymmetric Model*, *Phys. Rev. D* **100** (2019) 075010, [[1811.11743](#)].
- [94] Z. Lu, J. Qin, H. Li, Z.-L. Han, F. Huang, C.-Y. Li et al., *Phenomenological study of heavy neutral gauge bosons in the left-right symmetric model at future muon collider*, *JHEP* **08** (2025) 207, [[2408.15471](#)].
- [95] S. Bhattacharyya and A. Datta, *Phenomenology of an E_6 inspired extension of the Standard Model: Higgs sector*, *Phys. Rev. D* **105** (2022) 075021, [[2109.08524](#)].
- [96] Q.-H. Cao and D.-M. Zhang, *Collider Phenomenology of the 3-3-1 Model*, [1611.09337](#).
- [97] L. Di Luzio, J. Fuentes-Martin, A. Greljo, M. Nardecchia and S. Renner, *Maximal Flavour Violation: a Cabibbo mechanism for leptiquarks*, *JHEP* **11** (2018) 081, [[1808.00942](#)].

- [98] N. Greiner, K. Kong, J.-C. Park, S. C. Park and J.-C. Winter, *Model-Independent Production of a Top-Philic Resonance at the LHC*, *JHEP* **04** (2015) 029, [[1410.6099](#)].
- [99] J. H. Kim, K. Kong, S. J. Lee and G. Mohlabeng, *Probing TeV scale Top-Philic Resonances with Boosted Top-Tagging at the High Luminosity LHC*, *Phys. Rev. D* **94** (2016) 035023, [[1604.07421](#)].
- [100] ATLAS collaboration, M. Aaboud et al., *Search for heavy particles decaying into top-quark pairs using lepton-plus-jets events in proton-proton collisions at $\sqrt{s} = 13$ TeV with the ATLAS detector*, *Eur. Phys. J. C* **78** (2018) 565, [[1804.10823](#)].
- [101] ATLAS collaboration, M. Aaboud et al., *Search for heavy particles decaying into a top-quark pair in the fully hadronic final state in pp collisions at $\sqrt{s} = 13$ TeV with the ATLAS detector*, *Phys. Rev. D* **99** (2019) 092004, [[1902.10077](#)].
- [102] ATLAS collaboration, G. Aad et al., *Search for $t\bar{t}$ resonances in fully hadronic final states in pp collisions at $\sqrt{s} = 13$ TeV with the ATLAS detector*, *JHEP* **10** (2020) 061, [[2005.05138](#)].
- [103] ATLAS collaboration, G. Aad et al., *Search for top-philic heavy resonances in pp collisions at $\sqrt{s} = 13$ TeV with the ATLAS detector*, *Eur. Phys. J. C* **84** (2024) 157, [[2304.01678](#)].
- [104] H. E. Haber and L. Stephenson Haskins, *Supersymmetric theory and models.*, in *Theoretical Advanced Study Institute in Elementary Particle Physics: Anticipating the Next Discoveries in Particle Physics*, no. SCIPP-17-11, SCIPP 17/11, pp. 355–499, WSP, 2018. [1712.05926](#). DOI.
- [105] R. K. Barman, B. Bhattacharjee, A. Choudhury, D. Chowdhury, J. Lahiri and S. Ray, *Current status of MSSM Higgs sector with LHC 13 TeV data*, *Eur. Phys. J. Plus* **134** (2019) 150, [[1608.02573](#)].
- [106] H. Bahl, S. Liebler and T. Stefaniak, *MSSM Higgs benchmark scenarios for Run 2 and beyond: the low $\tan\beta$ region*, *Eur. Phys. J. C* **79** (2019) 279, [[1901.05933](#)].
- [107] R. K. Barman, B. Bhattacharjee, I. Chakraborty, A. Choudhury and N. Khan, *Electroweakino searches at the HL-LHC in the baryon number violating MSSM*, *Phys. Rev. D* **103** (2021) 015003, [[2003.10920](#)].
- [108] A. Adhikary, R. K. Barman, B. Bhattacharjee, A. De, R. M. Godbole and S. Kulkarni, *Long-lived NLSP in the NMSSM*, *Phys. Rev. D* **108** (2023) 035020, [[2207.00600](#)].
- [109] R. K. Barman, G. Belanger, B. Bhattacharjee, R. Godbole, G. Mendiratta and D. Sengupta, *Invisible decay of the Higgs boson in the context of a thermal and nonthermal relic in MSSM*, *Phys. Rev. D* **95** (2017) 095018, [[1703.03838](#)].
- [110] S. P. Martin, *A Supersymmetry primer*, *Adv. Ser. Direct. High Energy Phys.* **18** (1998) 1–98, [[hep-ph/9709356](#)].
- [111] S. Bhattacharyya, *Heavy Higgs boson searches at the LHC in light of a left-right symmetric model*, *Phys. Rev. D* **109** (2024) 015034, [[2307.04169](#)].
- [112] T. Appelquist, H.-C. Cheng and B. A. Dobrescu, *Bounds on universal extra dimensions*, *Phys. Rev. D* **64** (2001) 035002, [[hep-ph/0012100](#)].

- [113] H.-C. Cheng, *Introduction to Extra Dimensions*, in *Theoretical Advanced Study Institute in Elementary Particle Physics: Physics of the Large and the Small*, pp. 125–162, 2011. [1003.1162](#). DOI.
- [114] Q. Shafi, *E6 as a unifying gauge symmetry*, *Physics Letters B* **79** (1978) 301–303.
- [115] T. Fukuyama, *SO(10) GUT in Four and Five Dimensions: A Review*, *Int. J. Mod. Phys. A* **28** (2013) 1330008, [[1212.3407](#)].
- [116] V. Keus, S. F. King and S. Moretti, *Three-Higgs-doublet models: symmetries, potentials and Higgs boson masses*, *JHEP* **01** (2014) 052, [[1310.8253](#)].
- [117] I. P. Ivanov, *Building and testing models with extended Higgs sectors*, *Prog. Part. Nucl. Phys.* **95** (2017) 160–208, [[1702.03776](#)].
- [118] J. Shao, I. P. Ivanov and M. Korhonen, *Symmetries for the 4HDM: II. Extensions by rephasing groups*, *J. Phys. A* **57** (2024) 385401, [[2404.10349](#)].
- [119] M. P. Bento, J. C. Romão and J. a. P. Silva, *Unitarity bounds for all symmetry-constrained 3HDMs*, *JHEP* **08** (2022) 273, [[2204.13130](#)].
- [120] R. Boto, J. C. Romão and J. a. P. Silva, *Current bounds on the type-Z Z3 three-Higgs-doublet model*, *Phys. Rev. D* **104** (2021) 095006, [[2106.11977](#)].
- [121] S. Carrolo, J. C. Romão, J. a. P. Silva and F. Vazão, *Symmetry and decoupling in multi-Higgs boson models*, *Phys. Rev. D* **103** (2021) 075026, [[2102.11303](#)].
- [122] H. Georgi and M. Machacek, *Doubly charged higgs bosons*, *Nuclear Physics B* **262** (1985) 463–477.
- [123] M. S. Chanowitz and M. Golden, *Higgs boson triplets with $M_W = M_Z \cos \theta_W$* , *Physics Letters B* **165** (1985) 105–108.
- [124] H. E. Logan and M. B. Reimer, *Characterizing a benchmark scenario for heavy Higgs boson searches in the Georgi-Machacek model*, *Phys. Rev. D* **96** (2017) 095029, [[1709.01883](#)].
- [125] G. Bélanger, J. Dutta, R. M. Godbole, S. Kraml, M. Mitra, R. Padhan et al., *Revisiting the decoupling limit of the Georgi-Machacek model with a scalar singlet*, *JHEP* **10** (2024) 058, [[2405.18332](#)].
- [126] Z. Baire and A. Ahriche, *More constraints on the Georgi-Machacek model*, *Phys. Rev. D* **108** (2023) 055028, [[2207.00142](#)].
- [127] D. Chowdhury, P. Mondal and S. Samanta, *Next-to-Leading Order Unitarity Fits in the Extended Georgi-Machacek Model*, [2404.18996](#).
- [128] A. Kundu, P. Mondal and P. B. Pal, *Custodial symmetry, the Georgi-Machacek model, and other scalar extensions*, *Phys. Rev. D* **105** (2022) 115026, [[2111.14195](#)].
- [129] CMS collaboration, A. M. Sirunyan et al., *Search for a heavy Higgs boson decaying to a pair of W bosons in proton-proton collisions at $\sqrt{s} = 13$ TeV*, *JHEP* **03** (2020) 034, [[1912.01594](#)].

- [130] CMS collaboration, A. Tumasyan et al., *Search for a heavy Higgs boson decaying into two lighter Higgs bosons in the $\tau\tau bb$ final state at 13 TeV*, *JHEP* **11** (2021) 057, [[2106.10361](#)].
- [131] CMS collaboration, A. Tumasyan et al., *Search for a massive scalar resonance decaying to a light scalar and a Higgs boson in the four b quarks final state with boosted topology*, *Phys. Lett. B* **842** (2023) 137392, [[2204.12413](#)].
- [132] CMS collaboration, A. M. Sirunyan et al., *Search for charged Higgs bosons decaying into a top and a bottom quark in the all-jet final state of pp collisions at $\sqrt{s} = 13$ TeV*, *JHEP* **07** (2020) 126, [[2001.07763](#)].
- [133] CMS collaboration, A. Tumasyan et al., *Search for a charged Higgs boson decaying into a heavy neutral Higgs boson and a W boson in proton-proton collisions at $\sqrt{s} = 13$ TeV*, *JHEP* **09** (2023) 032, [[2207.01046](#)].
- [134] ATLAS collaboration, G. Aad et al., *Search for heavy neutral Higgs bosons decaying into a top quark pair in 140 fb^{-1} of proton-proton collision data at $\sqrt{s} = 13$ TeV with the ATLAS detector*, *JHEP* **08** (2024) 013, [[2404.18986](#)].
- [135] ATLAS collaboration, G. Aad et al., *Search for the decay of the Higgs boson to a Z boson and a light pseudoscalar particle decaying to two photons*, *Phys. Lett. B* **850** (2024) 138536, [[2312.01942](#)].
- [136] ATLAS collaboration, G. Aad et al., *Search for heavy Higgs bosons with flavour-violating couplings in multi-lepton plus b-jets final states in pp collisions at 13 TeV with the ATLAS detector*, *JHEP* **12** (2023) 081, [[2307.14759](#)].
- [137] ATLAS collaboration, G. Aad et al., *Search for charged Higgs bosons decaying into a top quark and a bottom quark at $\sqrt{s} = 13$ TeV with the ATLAS detector*, *JHEP* **06** (2021) 145, [[2102.10076](#)].
- [138] ATLAS collaboration, G. Aad et al., *Search for a heavy charged Higgs boson decaying into a W boson and a Higgs boson in final states with leptons and b-jets in $\sqrt{s} = 13$ TeV pp collisions with the ATLAS detector*, *JHEP* **02** (2025) 143, [[2411.03969](#)].
- [139] ATLAS collaboration, *Search for heavy resonances in the decay channel $W^+W^- \rightarrow e\nu\mu\nu$ in pp Collisions at $\sqrt{s} = 13$ TeV using 139 fb^{-1} of data with the ATLAS detector*, Tech. Rep. ATLAS-CONF-2022-066, CERN, Geneva, 2022.
- [140] CMS collaboration, *Identifying Hadronically Decaying Vector Bosons Merged into a Single Jet*, Tech. Rep. CMS-PAS-JME-13-006, CERN, 2013.
- [141] S. Gopalakrishna, T. Mandal, S. Mitra and R. Tibrewala, *LHC Signatures of a Vector-like b'* , *Phys. Rev. D* **84** (2011) 055001, [[1107.4306](#)].
- [142] S. Gopalakrishna, T. Mandal, S. Mitra and G. Moreau, *LHC Signatures of Warped-space Vectorlike Quarks*, *JHEP* **08** (2014) 079, [[1306.2656](#)].
- [143] A. Azatov, D. Chowdhury, D. Ghosh and T. S. Ray, *Same sign di-lepton candles of the composite gluons*, *JHEP* **08** (2015) 140, [[1505.01506](#)].

- [144] R. Benbrik et al., *Signatures of vector-like top partners decaying into new neutral scalar or pseudoscalar bosons*, *JHEP* **05** (2020) 028, [[1907.05929](#)].
- [145] A. Banerjee et al., *Phenomenological aspects of composite Higgs scenarios: exotic scalars and vector-like quarks*, [2203.07270](#).
- [146] A. Bhardwaj, T. Mandal, S. Mitra and C. Neeraj, *Roadmap to explore vectorlike quarks decaying to a new scalar or pseudoscalar*, *Phys. Rev. D* **106** (2022) 095014, [[2203.13753](#)].
- [147] A. Bhardwaj, K. Bhide, T. Mandal, S. Mitra and C. Neeraj, *Discovery prospects of a vectorlike top partner decaying to a singlet boson*, *Phys. Rev. D* **106** (2022) 075024, [[2204.09005](#)].
- [148] J. Bardhan, T. Mandal, S. Mitra and C. Neeraj, *Machine learning-enhanced search for a vectorlike singlet B quark decaying to a singlet scalar or pseudoscalar*, *Phys. Rev. D* **107** (2023) 115001, [[2212.02442](#)].
- [149] J. a. M. Alves, G. C. Branco, A. L. Cherchiglia, C. C. Nishi, J. T. Penedo, P. M. F. Pereira et al., *Vector-like singlet quarks: A roadmap*, *Phys. Rept.* **1057** (2024) 1–69, [[2304.10561](#)].
- [150] A. Banerjee, V. Ellajosyula and L. Panizzi, *Heavy vector-like quarks decaying to exotic scalars: a case study with triplets*, *JHEP* **01** (2024) 187, [[2311.17877](#)].
- [151] Y.-B. Liu, B. Hu and C.-Z. Li, *Single production of vectorlike quarks with charge 5/3 at the 14 TeV LHC*, *Nucl. Phys. B* **1007** (2024) 116667, [[2402.01248](#)].
- [152] A. Banerjee, E. Bergeaas Kuutmann, V. Ellajosyula, R. Enberg, G. Ferretti and L. Panizzi, *Vector-like quarks: Status and new directions at the LHC*, *SciPost Phys. Core* **7** (2024) 079, [[2406.09193](#)].
- [153] Y.-J. Zhang, Y.-T. Zhu, L. Han, Y.-P. Bi and T.-G. Liu, *Searching for the vector-like X-quark at the future electron–proton colliders*, *Eur. Phys. J. C* **84** (2024) 1184.
- [154] CMS collaboration, A. Hayrapetyan et al., *Review of searches for vector-like quarks, vector-like leptons, and heavy neutral leptons in proton–proton collisions at $\sqrt{s}=13$ TeV at the CMS experiment*, *Phys. Rept.* **1115** (2025) 570–677, [[2405.17605](#)].
- [155] ATLAS collaboration, *Search for singly produced vectorlike top partners in multilepton final states with 139 fb⁻¹ of pp collision data at $\sqrt{s} = 13$ TeV with the ATLAS detector*, *Phys. Rev. D* **109** (Jun, 2024) 112012.
- [156] ATLAS collaboration, *Search for single production of a vectorlike T quark decaying into a Higgs boson and top quark with fully hadronic final states using the ATLAS detector*, *Phys. Rev. D* **105** (May, 2022) 092012.
- [157] ATLAS collaboration, *Search for pair-production of vector-like quarks in pp collision events at $\sqrt{s}=13$ TeV with at least one leptonically decaying Z boson and a third-generation quark with the ATLAS detector*, *Physics Letters B* **843** (2023) 138019.
- [158] ATLAS collaboration, *Search for singly produced vectorlike top partners in multilepton final states with 139 fb⁻¹ of pp collision data at $\sqrt{s} = 13$ TeV with the atlas detector*, *Phys. Rev. D* **109** (Jun, 2024) 112012.

- [159] CMS collaboration, A. Tumasyan et al., *Search for single production of a vector-like T quark decaying to a top quark and a Z boson in the final state with jets and missing transverse momentum at $\sqrt{s} = 13$ TeV*, *JHEP* **05** (2022) 093, [[2201.02227](#)].
- [160] CMS collaboration, A. Tumasyan et al., *Search for a W' boson decaying to a vector-like quark and a top or bottom quark in the all-jets final state at $\sqrt{s} = 13$ TeV*, *JHEP* **09** (2022) 088, [[2202.12988](#)].
- [161] CMS collaboration, A. Tumasyan et al., *Search for pair production of vector-like quarks in leptonic final states in proton-proton collisions at $\sqrt{s} = 13$ TeV*, *JHEP* **07** (2023) 020, [[2209.07327](#)].
- [162] CMS collaboration, A. Tumasyan et al., *Search for a vector-like quark $T' \rightarrow tH$ via the diphoton decay mode of the Higgs boson in proton-proton collisions at $\sqrt{s} = 13$ TeV*, *JHEP* **09** (2023) 057, [[2302.12802](#)].
- [163] M. Buchkremer, G. Cacciapaglia, A. Deandrea and L. Panizzi, *Model Independent Framework for Searches of Top Partners*, *Nucl. Phys. B* **876** (2013) 376–417, [[1305.4172](#)].
- [164] J.-Z. Han, J. Yang, S. Xu and H.-K. Wang, *Search for single production of vector-like B quark via bZ channel at the HL-LHC*, *Nuclear Physics B* **975** (2022) 115672.
- [165] B. Yang, Z. Li, X. Jia, S. Moretti and L. Shang, *Search for single vector-like B quark production in hadronic final states at the LHC*, *Eur. Phys. J. C* **84** (2024) 1124, [[2405.13452](#)].
- [166] CMS collaboration, A. M. Sirunyan et al., *Search for single production of vector-like quarks decaying to a top quark and a W boson in proton-proton collisions at $\sqrt{s} = 13$ TeV*, *Eur. Phys. J. C* **79** (2019) 90, [[1809.08597](#)].
- [167] ATLAS collaboration, G. Aad et al., *Optimisation of large-radius jet reconstruction for the ATLAS detector in 13 TeV proton–proton collisions*, *Eur. Phys. J. C* **81** (2021) 334, [[2009.04986](#)].
- [168] ATLAS collaboration, G. Aad et al., *Search for single production of a vectorlike T quark decaying into a Higgs boson and top quark with fully hadronic final states using the ATLAS detector*, *Phys. Rev. D* **105** (2022) 092012, [[2201.07045](#)].
- [169] ATLAS collaboration, G. Aad et al., *Search for pair-production of vector-like quarks in pp collision events at $\sqrt{s}=13$ TeV with at least one leptonically decaying Z boson and a third-generation quark with the ATLAS detector*, *Phys. Lett. B* **843** (2023) 138019, [[2210.15413](#)].
- [170] ATLAS collaboration, G. Aad et al., *Search for singly produced vectorlike top partners in multilepton final states with 139 fb^{-1} of pp collision data at $\sqrt{s}=13$ TeV with the ATLAS detector*, *Phys. Rev. D* **109** (2024) 112012, [[2307.07584](#)].
- [171] ATLAS collaboration, G. Aad et al., *Search for new particles in final states with a boosted top quark and missing transverse momentum in proton-proton collisions at $\sqrt{s} = 13$ TeV with the ATLAS detector*, *JHEP* **05** (2024) 263, [[2402.16561](#)].

- [172] J. Alwall, M. Herquet, F. Maltoni, O. Mattelaer and T. Stelzer, *MadGraph 5 : Going Beyond*, *JHEP* **06** (2011) 128, [[1106.0522](#)].
- [173] Mathieu Buchkremer, Giacomo Cacciapaglia, Aldo Deandrea, Luca Panizzi , “VLQ Model.” http://feynrules.irmp.ucl.ac.be/wiki/VLQ_bsingletv1, 2014.
- [174] DELPHES 3 collaboration, J. de Favereau, C. Delaere, P. Demin, A. Giammanco, V. Lemaître, A. Mertens et al., *DELPHES 3, A modular framework for fast simulation of a generic collider experiment*, *JHEP* **02** (2014) 057, [[1307.6346](#)].
- [175] T. Sjostrand, S. Mrenna and P. Z. Skands, *A Brief Introduction to PYTHIA 8.1*, *Comput. Phys. Commun.* **178** (2008) 852–867, [[0710.3820](#)].
- [176] NNPDF collaboration, R. D. Ball et al., *Parton distributions for the LHC Run II*, *JHEP* **04** (2015) 040, [[1410.8849](#)].
- [177] M. Cacciari and G. P. Salam, *Dispelling the N^3 myth for the k_t jet-finder*, *Phys. Lett. B* **641** (2006) 57–61, [[hep-ph/0512210](#)].
- [178] M. Cacciari, G. P. Salam and G. Soyez, *FastJet User Manual*, *Eur. Phys. J. C* **72** (2012) 1896, [[1111.6097](#)].
- [179] S. Ellis, J. Huston, K. Hatakeyama, P. Loch and M. Tönnesmann, *Jets in hadron–hadron collisions*, *Progress in Particle and Nuclear Physics* **60** (Apr., 2008) 484–551.
- [180] G. P. Salam, *Towards jetography*, *The European Physical Journal C* **67** (May, 2010) 637–686.
- [181] A. J. Larkoski, F. Maltoni and M. Selvaggi, *Tracking down hyper-boosted top quarks*, *JHEP* **06** (2015) 032, [[1503.03347](#)].
- [182] A. J. Larkoski and J. Thaler, *Aspects of jets at 100 TeV*, *Phys. Rev. D* **90** (2014) 034010, [[1406.7011](#)].
- [183] B. Mukhopadhyaya, T. Samui and R. K. Singh, *Dynamic radius jet clustering algorithm*, *JHEP* **04** (2023) 019, [[2301.13074](#)].
- [184] S. Jain, *Revisiting new and old jet clustering algorithms for beyond the standard model Higgs searches in the final states with b-jets*. PhD thesis, University of Southampton, Southampton U., Southampton U., 2023.
- [185] T. Lapsien, R. Kogler and J. Haller, *A new tagger for hadronically decaying heavy particles at the LHC*, *Eur. Phys. J. C* **76** (2016) 600, [[1606.04961](#)].
- [186] A. J. Larkoski, S. Marzani, G. Soyez and J. Thaler, *Soft Drop*, *JHEP* **05** (2014) 146, [[1402.2657](#)].
- [187] M. Arjovsky, S. Chintala and L. Bottou, *Wasserstein generative adversarial networks*, in *International conference on machine learning*, pp. 214–223, PMLR, 2017.
- [188] ATLAS collaboration, *Constituent-Based Top-Quark Tagging with the ATLAS Detector*, Tech. Rep. ATL-PHYS-PUB-2022-039, CERN, Geneva, 2022.

- [189] G. Cowan, K. Cranmer, E. Gross and O. Vitells, *Asymptotic formulae for likelihood-based tests of new physics*, *Eur. Phys. J. C* **71** (2011) 1554, [[1007.1727](#)].
- [190] FCC collaboration, L. Borghonovi et al., *Higgs and Electro-weak symmetry breaking at the FCC-hh*, Tech. Rep. CERN-ACC-2018-0045, 3, 2019.
- [191] CMS collaboration, A. M. Sirunyan et al., *Search for resonant $t\bar{t}$ production in proton-proton collisions at $\sqrt{s} = 13$ TeV*, *JHEP* **04** (2019) 031, [[1810.05905](#)].
- [192] E. Perez Codina and P. G. Roloff, *Initial Study of the Reconstruction of Boosted B-hadrons and τ -leptons at FCC-hh*, Tech. Rep. CERN-ACC-2018-0035, LCD-NOTE-2018-003, CERN, Geneva, 2018.
- [193] E. Perez Codina and P. G. Roloff, *Hit multiplicity approach to b-tagging in FCC-hh*, Tech. Rep. CERN-ACC-2018-0023, LCD-Note-2018-001, CERN, Geneva, 2018.
- [194] V. Barger, *Collider Physics*. CRC Press, 2018.